Towards optimum swirl recovery for propeller propulsion systems

Li, Qingxi

DOI
10.4233/uuid:ef966464-6b76-434d-b147-81ec247b023c

Publication date
2019

Document Version
Final published version

Citation (APA)
Li, Q. (2019). *Towards optimum swirl recovery for propeller propulsion systems*. [Dissertation (TU Delft), Delft University of Technology]. https://doi.org/10.4233/uuid:ef966464-6b76-434d-b147-81ec247b023c

TOWARDS OPTIMUM SWIRL RECOVERY FOR PROPELLER PROPULSION SYSTEMS

Towards Optimum Swirl Recovery for Propeller Propulsion Systems

Dissertation

for the purpose of obtaining the degree of doctor
at Delft University of Technology
by the authority of the Rector Magnificus, prof.dr.ir. T.H.J.J. van der Hagen,
Chair of the Board for Doctorates
to be defended publicly on
Tuesday 3 September 2019 at 10:00 o'clock

by

Qingxi LI
Master of Engineering in Aerospace Propulsion, Theory and Engineering
Northwestern Polytechnical University, China
born in Taiyuan, China

This dissertation has been approved by the promotors.
Composition of the doctoral committee:

Rector Magnificus,	chairperson
Prof.dr.ir. L.L.M Veldhuis	Delft University of Technology, promotor
Prof.dr.ing. G.Eitelberg	Delft University of Technology, promotor

Independent members:

Prof.dr.ir. T.J.C. van Terwisga	Delft University of Technology
Prof.dr.ir. Y. Wang	Northwestern Polytechnical University, China
Prof.dr. J.Friedrichs	Technical University of Braunschweig, Germany
Prof.dr.ir. C.J.Simao Ferreira	Delft University of Technology
Prof.dr. L.R. Calavera	Universidad Politécnica de Madrid, Spain
Prof.dr.ir. P. Colonna	Delft University of Technology, reserve member

The author was funded by the *China Scholarship Council*.

Keywords: propeller, swirl recovery vane, propeller integration.
Cover designed by: Qingxi LI
Printed by: Glideprint inc.

ISBN: 978-94-6323-805-2
An electronic version of this dissertation is available at *http://repository.tudelft.nl*

Summary

In a propeller propulsion system, due to the torque working on the propeller, a rotational motion of the fluid is generated. This rotational motion, expressed as a swirl component in the slipstream, does not result in any useful propulsive power, but causes a decrease in propeller efficiency. By recovering the momentum in the crosswise direction with other aerodynamic components located in the slipstream, either extra thrust can be produced or the overall drag of the aircraft can be reduced with the same power input from the propeller. This dissertation provides aerodynamic design and investigation of swirl recovery for both uninstalled and installed propeller propulsion systems.

Swirl recovery vanes (SRVs) are a set of stationary vanes located behind a propeller, by which the angular momentum contained in the propeller slipstream can be recovered and thereby extra thrust can be generated. In this thesis, a design framework of SRVs is developed based on a lifting line model. The design method features a fast turnaround time, which makes it suitable for system level design and parameter studies.

As a test example, a set of SRVs was designed for an uninstalled six-bladed propeller at a high propeller loading condition. A parametric study was performed of the SRV performance as a function of the blade count and radius. In order to validate the design routine, an experiment was performed with a propeller and the SRVs in a low-speed open-jet wind tunnel. The thrust generated by the SRVs was measured at different propeller loading conditions. The experimental results show that the SRVs provided thrust at all the measured propeller advance ratios. Since the SRVs did not require any extra power input, the propulsive efficiency of the system (propeller + SRVs) has improved accordingly for all the loading conditions considered.

For an installed tractor-propeller propulsion system, both the downstream wing and the SRV have the ability of recovering the swirl of propeller slipstream. In the first case of swirl recovery from the trailing wing, reduction of wing induced drag can be achieved. In order to determine the optimum wing shape for maximum drag reduction, a multi-fidelity optimization procedure is developed, where the low-fidelity method corresponds to the potential flow-based method, and the high-fidelity method is based on an analysis by solving Euler equations. As a test case, the twist distribution of the wing is optimized at the cruise condition of a typical turboprop aircraft. Compared to the baseline wing (untwisted), the induced drag of the optimized wing has decreased by 1.4% of the propeller thrust.

In the second case of swirl recovery from the SRV, extra thrust can be generated by the vanes. Four different cases of SRVs installation positions are investigated (with assumption of inviscid flow) with different axial and azimuthal positions relative to the wing. An optimum configuration is identified where SRVs are positioned on the blade-downgoing side downstream of the wing.

For the identified optimum configuration, a set of SRVs was designed taking the effect

of viscosity into account. The SRV design is subsequently validated by RANS simulation. Good agreement is observed in the lift, circulation, and thrust distributions of the SRV between the lifting line prediction and the RANS result. A thrust of 1.6% of propeller thrust from SRVs was validated by the RANS simulation.

Comparing the two ways of swirl recovery, further investigation has shown that for the installed propeller propulsion system, due to the different aerodynamic consequences of the two (drag reduction of the wing compared with thrust enhancement from the SRV), they can be algebraically added up.

Samenvatting

Propellervoortstuwingssystemen introduceren een draaiing in de stroming door het koppel op de propeller. Deze draaiing, hier benoemd als een swirl-component in de slipstroom, levert geen nuttig voortstuwingsvermogen op, en zorgt dus voor een afname van het propellerrendement. Door de impuls in de omtreksrichting terug te winnen met andere aerodynamische elementen die in de slipstroom zijn geplaatst, kan ofwel extra stuwkracht gegenereerd worden ofwel de totale weerstand van het vliegtuig verminderd worden, bij gelijke vermogensafgifte van de propeller. Dit proefschrift voorziet in een aerodynamisch ontwerp en onderzoek van swirl recovery voor zowel geïsoleerde als geïnstalleerde propellervoortstuwingssystemen.

Swirl recovery vanes (SRV's) zijn een set statorbladen, geplaatst achter een propeller, waarmee de impuls in omtreksrichting die in de slipstroom aanwezig is teruggewonnen kan worden en daardoor extra stuwkracht geproduceerd kan worden. In dit proefschrift wordt een ontwerpgeraamte voor SRV's ontwikkeld op basis van dragende-lijn theorie. De analysemethode biedt een snelle doorlooptijd, welke de methode geschikt maakt voor ontwerp op systeemniveau en voor parameterstudies.

Als voorbeeld werd een set SRV's ontworpen voor een geïsoleerde zesbladige propeller met een bedrijfsconditie met hoge bladbelasting. Een parameterstudie van de SRV prestaties werd uitgevoerd met als variabelen het aantal statorvanen en hun straal. Om de ontwerproutine te valideren werd een experiment uitgevoerd met een propeller en de SRV's in een lage-snelheids open-straal windtunnel. De stuwkracht gegenereerd door de SRV's werd gemeten bij verschillende bedrijfscondities van de propeller. De uitkomsten van het experiment tonen aan dat de SRV's stuwkracht leverden bij alle gemeten voortgangscoëfficiënten van de propeller. Aangezien de SRV's geen extra vermogensafgifte vereisen, werd het rendement van het voortstuwingsysteem zodoende verbeterd bij alle beschouwde bedrijfscondities.

Voor een geïnstalleerd propellervoortstuwingssysteem in trekconfiguratie zijn zowel de stroomafwaarts gelegen vleugel als de SRV's in staat om de swirl in de slipstroom te herwinnen. In het eerste geval van swirl recovery door de stroomafwaarts gelegen vleugel kan een vermindering van de geïnduceerde weerstand van de vleugel behaald worden. Om de optimale vorm van de vleugel voor een maximale weerstandsvermindering te bepalen, werd een optimalisatieprocedure ontwikkeld met meerdere getrouwheidsniveaus, waarin de lage-orde methode overeenkomt met een potentiaalstromingsmethode, en de hoge-orde methode is gebaseerd op een analyse die de Euler vergelijkingen oplost. Als test werd de wrongverdeling van de vleugel geoptimaliseerd voor de kruisconditie van een typisch turboprop vliegtuig. In vergelijking met de oorspronkelijke vleugel (zonder wrong), werd voor de geoptimaliseerde vleugel de geïnduceerde weerstand verminderd met 1.4% van de stuwkracht van de propeller.

In het tweede geval van swirl recovery door de SRV's kan extra stuwkracht worden

gegenereerd door de statorvanen. Vier verschillende gevallen van SRV installatieposities werden onderzocht (onder de aanname van niet-viskeuze stroming) met verschillende posities ten opzichte van de vleugel in axiale richting en omtreksrichting. Een optimale configuratie werd geïdentificeerd waarbij de SRV's stroomafwaarts gepositioneerd zijn van de vleugel, aan de kant van de vleugel waar het propellerblad naar beneden beweegt.

Voor de geïdentificeerde optimale configuratie werd een set SRV's ontworpen waarbij het effect van viscositeit in acht genomen werd. Dit SRV ontwerp werd vervolgens gevalideerd met een RANS simulatie. Een goede overeenkomst werd waargenomen tussen de dragende-lijn voorspelling en RANS resultaten voor de draagkrachts-, circulatie-, en stuwkrachtverdeling op de SRV's. Een stuwkracht op de SRV's van 1.6% van de stuwkracht van de propeller werd gevalideerd door de RANS simulatie.

De twee manieren van swirl recovery werden vergeleken aan de hand van aanvullend onderzoek. Dit toonde aan dat voor het geïnstalleerde propellervoortstuwingssysteem de twee manieren niet uitwisselbaar zijn, vanwege de verschillende aerodynamische mechanismes voor beide manieren (een weerstandsvermindering van de vleugel ten opzichte van een toename in stuwkracht door de SRVs).

Content

Nomenclature

Abbreviations

CRP	contra-rotating propeller
DIRECT	dividing rectangles optimization algorithm
GCI	grid convergence index
Ma	Mach number
PIV	particle image velocimetry
PSV	pre-swirl vane
RANS	Reynolds-averaged Navier-Stokes
Re	Reynolds number
SBO	surrogate-based optimization
SPRP	shape-preserving response prediction
SRP	single-rotation propeller
SRV	swirl recovery vane
URANS	unsteady Reynolds-Averaged Navier-Stokes

English Symbols

a_{SoS}	speed of sound in air, [m/s]
b	order of convergence in Richardson extrapolation
c	chord length, [m]
c_r	wing root chord length, [m]
C_d	sectional drag coefficient, $dD/(0.5\rho V^{*2}c)$
$C_{D,i}$	induced drag coefficient, $D_I/(0.5\rho V_\infty^2 S)$
C_l	sectional lift coefficient, $dL/(0.5\rho V^{*2}c)$
C_L	lift coefficient, $L/(0.5\rho V_\infty^2 S)$
C_p	pressure coefficient, $(p-p_\infty)/(0.5\rho V_\infty^2)$
C_P	power coefficient, $P/(\rho n_s^3 D_P^5)$
C_Q	torque coefficient, $Q/(\rho n_s^2 D_P^5)$
C_T	thrust coefficient defined based on propeller properties, $T/(\rho n_s^2 D_P^4)$
D	drag force, [N]
D_I	induced drag, [N]
D_P	propeller diameter, [m]
$\boldsymbol{F}$	force vectors on wing panels, [N]
h	maximum camber to chord ratio of airfoil

h_p	chordwise position of maximum camber of airfoil, [m]
J	propeller advance ratio, $V_\infty / (n_s D_P)$
k	turbulent kinetic energy, [$m^2 \cdot s^{-2}$]
K	air bulk elastic modulus, [N/m^2]
l	wing span, [m]
L	lift force, [N]
m_{MTO}	maximum take-off weight, [kg]
$\boldsymbol{n}$	unit normal vector
n_s	propeller rotation frequency, [s^{-1}]
N	blade count
p	static pressure, [Pa]
p_∞	freestream static pressure, [Pa]
P	propeller shaft power, [W]
q	grid refinement ratio in Richardson extrapolation
Q	torque, [N·m]
r	radial coordinate, [m]
R	propeller radius, [m]
R_{hub}	propeller hub radius, [m]
S	wing area, [m^2]
t	maximum thickness to chord ratio of airfoil
t_p	chordwise position of maximum thickness of airfoil, [m]
T	thrust, [N]
T_C	thrust coefficient defined based on wing properties, $T/0.5\rho V_\infty^2 S$
u, v, w	perturbation velocity in x, y, and z direction, [$m \cdot s^{-1}$]
v_a, v_t	axial and circumferential induced velocities, [$m \cdot s^{-1}$]
V_a, V_t	axial and circumferential inflow velocities, [$m \cdot s^{-1}$]
V_∞	freestream velocity, [$m \cdot s^{-1}$]
V^*	resultant velocity, [$m \cdot s^{-1}$]
$\bar{V}$	time-averaged velocity, [$m \cdot s^{-1}$]
x, y, z	coordinate in axial, vertical, spanwise directions, [m]
X	samples in optimization process
y^+	dimensionless wall distance
Z	number of mesh points

Greek Symbols

α	angle of attack, [deg]
β	pitch angle, [deg]

Γ	circulation, [$m^2 \cdot s^{-1}$]
η	efficiency
μ	doublet strength, [$m^3 \cdot s^{-1}$]
ξ	swirl angle, [deg]
Π	non-dimensional parameter in dimensional analysis
ρ	air density, [$kg \cdot m^{-3}$]
σ	source strength, [$m^2 \cdot s^{-1}$]
τ	wing twist angle, [deg]
υ	air kinematic viscosity, [m^2/s]
φ	blade phase angle, [deg]
Φ	velocity potential, [$m^2 \cdot s^{-1}$]
ω	propeller angular velocity, [$rad \cdot s^{-1}$]
$\boldsymbol{\Omega}$	position vector, [m]

Subscript

P	propeller
V	SRV
W	Wing

Chapter 1 Introduction

1.1 Brief history of propeller propulsion systems

With their unusual intellect and talent, the Wright brothers were the first in aviation history to couple the momentum theory of Froude (see Ref. [1] and discussion in Sec. 2.2.1) with the blade element theory of Drzewiecki (see Ref. [2] and discussion in Sec. 2.2.3) in their design of air propellers. With the help of the theory they developed, the Wright brothers were able to design and manufacture twisted airplane propellers [3]. These propellers enabled the first successful controlled, sustained and powered flight in aviation history on 17 December 1903 [4]. In the years thereafter, effort has been dedicated to finding the solution for an optimum propeller design. In 1919, Betz and Prandtl [5] presented the optimum induced velocity distribution for minimum induced loss of a propeller with assumption of infinite number of blades. Later on, with the introduction of the lifting-line theory for propellers (discussed in Sec. 2.2.2), Goldstein [6] derived the expression for the circulation distribution that would give the ideal induced inflow presented by Betz and Prandtl. Combined with the application of Clark Y and R.A.F. 6-series airfoils [7] and later NACA 16-series airfoils [8], the development of this design methodology led to successful propeller propulsion applications at cruise Mach number as high as 0.6 [9] by the mid-1950s.

In the pursuit of even higher cruise speed, turbojet and turbofan propulsion systems dominated both the research in academia and the applications in industry from the mid-1950s until the mid-1970s. These systems enabled flights at cruise Mach number of 0.85 [9].

According to the momentum theory, the ideal propulsive efficiency of an aircraft propulsor η_{ideal} is determined by the freestream velocity V_∞ and the jet speed of the propulsor in the aircraft reference frame V_{jet} as:

$$\eta_{ideal} = \frac{2}{1 + V_{jet}/V_\infty} \tag{1.1}$$

By accelerating a larger amount of air compared to turbojets and turbofans, turboprops generate a lower jet velocity in order to obtain the same thrust, thus achieving higher propulsive efficiencies. However, the lower propulsive efficiencies of turbojet and turbofan propulsion systems compared to turboprops hardly mattered when the fuel costs were low (near 10 cents per gallon in 1973 [10]). By the end of 1973, the fuel costs represented only 12% of total operating expenses and about 20% of cash operating costs of airlines [11].

The situation had been changed dramatically due to the occurrence of the energy crisis which started in 1973. The fuel prices had tripled by 1978, driving the cash-cost percentage

of fuel up to 50% for airlines [12]. As it became clear not only that the Organization of the Petroleum Exporting Countries (OPEC) would not break up but also that further increases in fuel prices would be forthcoming [11], airlines began to take a closer look at the fuel cost per seat, which evoked a resurgence of interest in high-speed propellers for improved fuel savings. Many advanced concepts were proposed, evaluated and used in the design of high-speed propellers for better aerodynamic and acoustic performances in the theoretical and experimental studies carried out by NASA [13,14]. These new concepts included: a) blade-tip sweep and reduced blade thickness in order to reduce noise emissions and minimize compressibility losses at the outboard part of the blades, b) tailored nacelle blockage and spinner area-ruling to reduce blade-to-blade choking and compressibility losses in the blade root region, and c) the advanced airfoil technology [15]. The advanced design concepts suggested that turboprop propulsion could be able to maintain the performance advantage at cruise condition up to Mach number 0.85 as shown in Figure 1.1.

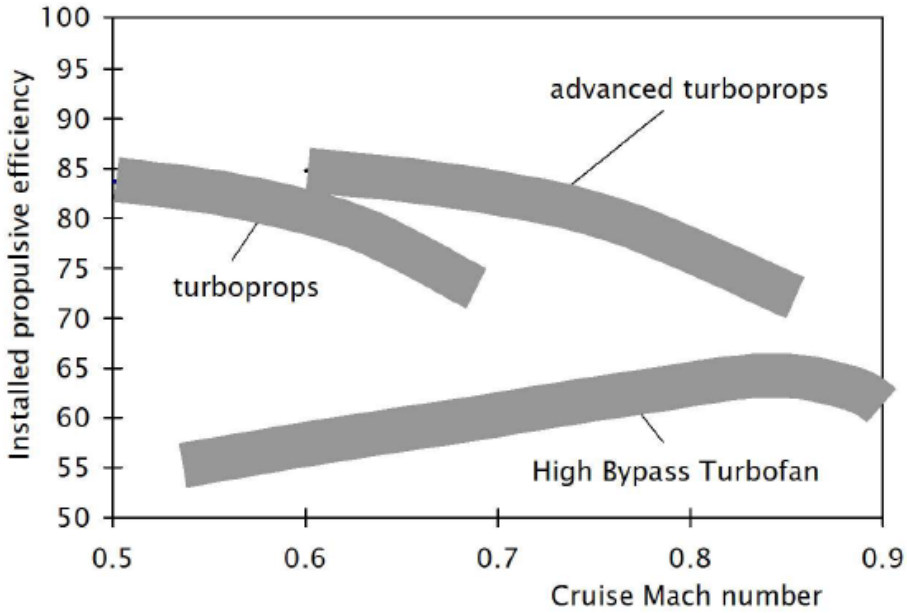

Figure 1.1 Comparison of installed propulsive efficiencies between turboprops and turbofans with respect to cruise Mach number. (Adapted from Veldhuis [16])

Due to the favorable propulsive efficiencies at lower speeds, turboprop aircraft have proven to be the preferred choice for the short-haul airline operations where the missions are climb and descent dominated [17]. As highlighted in a study by Aerei da Trasporto Regionale (ATR) [18], in 2017, fifty percent of the sectors below 330 nautical miles were operated by turboprops. Additionally, in the large regional aircraft segment (60-90 seats) of in-service fleet, turboprop engines and turbojet engines share the market evenly since the year 2003 according to the statistics published by Bombardier Aerospace [19]. Furthermore, the commercial turboprop aircraft manufactures like ATR and Bombardier initiated a new focus on the 90-120 seats segment market where the turbojet-powered aircraft is, so far, the only choice [20]. All of these applications lead to the conclusion that the growth of the fleet operated by turboprop aircraft will be mainly driven by the creation of new routes, which is envisioned to account for 60% of turboprop deliveries up to 2037 [18].

The advantage of turboprop aircraft on take-off, landing and endurance performance

makes them explicitly useful for military tasks, such as steep descents, take-off from short or ruined runways, surveillance, cargo droppings and other tactical missions. It was estimated that around 80% of the top ten military transport aircraft were propeller-driven aircraft [21].

In spite of the high propulsive efficiency of isolated turboprop propulsion systems, further improvement can be made of the overall aerodynamic performance of the aircraft when utilizing the aerodynamic interaction between the propeller propulsion system and other components of the aircraft. One of the ways of achieving this improvement is by utilizing the so-called swirl recovery process [9]. Due to the torque working on the propeller, a rotational motion of the fluid is generated. This rotational motion, expressed as a swirl component in the slipstream, does not result in any useful propulsive power (calculated by ($T_P \cdot V_\infty$) where T_P is propeller thrust and V_∞ is freestream velocity), but causes a decrease in propeller efficiency (defined by $\eta_P = \frac{T_P V_\infty}{P}$ where P is propeller shaft power). In a preliminary analysis performed by Veldhuis [22], the amount of the swirl loss was shown to be related to the loading conditions of the propeller. For a typical cruise condition, a 6.7% propeller efficiency loss due to swirl was predicted out of the 19% total efficiency loss. A similar amount of swirl loss (7%) for cruise conditions was also reported by Kroo [23]. By recovering the momentum in the crosswise direction with other aerodynamic components located in the slipstream, either extra thrust can be produced (as will be discussed in Chapter 3 and Chapter 4) or the overall drag of the aircraft can be reduced (as will be discussed in Chapter 4 and Chapter 5) with the same power input from the propeller. Several types of devices exist which have the ability for swirl recovery. In the next section, a brief review of the research on swirl recovery for propeller propulsion systems is presented.

1.2 Review of swirl recovery for propeller propulsion systems

As discussed in the previous section, swirl recovery is achieved by adding another structural component which is positioned in such a way as to affect the propeller slipstream. In terms of its axial position, this component can be either ahead or behind the propeller, and in terms of motion, it can be either rotational or stationary. On the condition that the swirl-recovery component is also rotating (in the opposite direction with the front propeller stage), it represents the case of contra-rotating propeller (CRP). Figure 1.2 gives an example of CRP setup implemented on the Antonov An-70 aircraft [30].

The contra-rotating propeller performance was previously the focus of a research project led by NASA and US industry in the late 1970s and 1980s [24]. At flight Mach number of 0.75, the propeller efficiency of the CRP model tested in the research project was 86%, about 8% better than that of the equivalent single-rotation propeller (SRP). By splitting the loading between two sets of blades, a CRP enables to realize a smaller radius than a SRP with the same thrust production; this makes it more suitable for high-speed applications. On top of an improved aerodynamic performance, CRP configurations typically entail advantageous solutions for stability control, including a considerable reduction of torque and gyroscopic loads, and enhanced aircraft flutter stability [9]. However, some inherent flaws of CRP

impose a restriction for broader application of this type of propulsion. Examples are the high weight of the propulsion system due to the complex gear system required for obtaining the contra-rotation [25 , 26], together with the additional noise caused by the transient aerodynamic interaction between the two contra-rotating stages [27,28,29].

Figure 1.2 An example of contra-rotating propellers implemented on the Antonov An-70 aircraft. ([30])

When the swirl-recovery component is stationary and located in front of the propeller stage, it in fact is equivalent to a set of vanes which are known as pre-swirl vanes (PSVs), which are often referred to as reaction fins as found in some marine applications (Figure 1.3). A swirling flow opposite to the sense of propeller rotation is generated by PSVs. The propeller blades experience this rotating flow as an additional loading at a constant rotation speed, through which the delivered thrust per unit power is raised. When the increase of the propeller thrust is greater than the drag force experienced by the PSVs, a gain in net thrust is obtained.

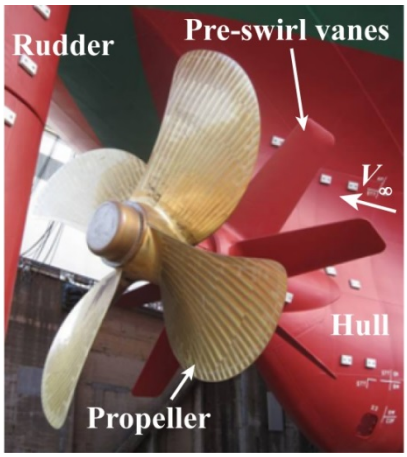

Figure 1.3 An example of pre-swirl vanes applied for marine propellers on a vessel. (Adapted from Kawakita [31])

Since most of the propellers in marine applications are pusher propellers located behind the hulls, many investigations were dedicated to the hydrodynamic design and testing of PSVs for marine propellers [32,33,34]. Fuel savings were reported when PSVs were added. However, to the best of the author's knowledge, no research has been performed on the investigation of PSVs for air propellers. This is probably due to two reasons: firstly, most of the propellers used on modern turboprop aircraft are tractor propellers; secondly, the addition

of PSVs in front of the propeller would lead to significant unsteady loading and subsequent noise production from the propeller blades.

When the swirl-recovery component is stationary and located behind the propeller stage, it is equivalent to a set of vanes known as swirl-recovery vanes (SRVs). The angular momentum that is generated by the propeller (represented by $v_{t,P}$ in Figure 1.4) is recovered by the vanes due to the fact that the angular velocity induced by SRV ($v_{t,V}$) has an opposite direction to that of $v_{t,P}$. In this way, the angular momentum contained in the slipstream is reduced compared to a single rotation propeller.

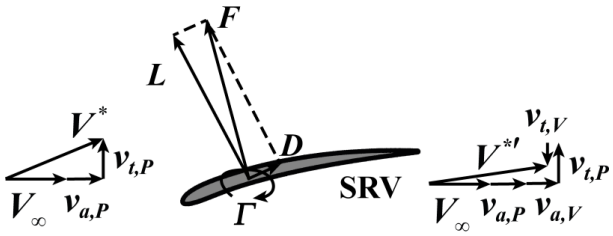

Figure 1.4 Illustration of swirl recovery by SRV.

As part of the Advanced Turboprop Project, SRVs were designed and tested at transonic cruise conditions by NASA in the late 1980s [35] (Figure 1.5). Experimental data showed an extra thrust of 2% from SRVs with constant power input at the design condition of Ma = 0.8 [36]. At lower off-design Mach number of 0.6, the efficiency gain of SRVs was even higher, approaching 4.5%. Besides, the ratio of the vane torque to the rotor torque was rather constant at different speeds. This leads to a reduction of the torque load of the whole propulsion system which is similar to the case of a CRP configuration. With these propulsive and structural benefits, no additional noise was observed by addition of SRVs [37].

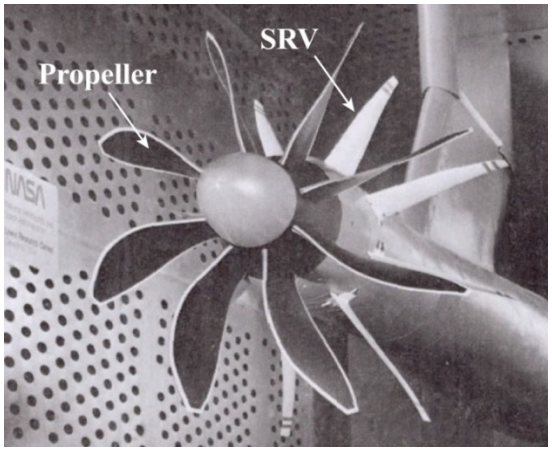

Figure 1.5 SR-7A propeller with installed SRVs model tested in a wind tunnel.
(Adapted from Dittmar [37])

Despite these promising results, research on SRVs was stopped when the energy crisis ended in the 1990s. Until recently, it was reintroduced by research groups at Delft University of Technology and Northwestern Polytechnical University. In the numerical SRV design work performed by Wang [38] and Stokkermans [39], the optimization results have shown extra thrust on the order of 2–5% from SRVs at relatively high propeller loading conditions.

The unsteady interaction between the propeller and the SRVs was analyzed by Li [40], and the main source of unsteadiness on the vane surfaces was due to the impingement of the rotor tip vortices. Particle-image-velocimetry (PIV) measurements discussed in Ref. [41] confirmed a positive swirl recovery by the vanes, while a numerical study of the same configuration predicted an efficiency gain of 0.7%.

In the cases where the propeller is wing-mounted or pylon-mounted, the swirl velocity can also be affected by the wing or the pylon where the propeller is installed. Depending on the location of the blade relative to the wing/pylon, the swirl velocity generated by the propeller can be either recovered or enhanced (Figure 1.6). On the blade-upgoing side, the swirl velocity produces regions of upwash on the wing, augments the section lift and rotates the force vector forward. This induces an equivalent thrust on the wing section. On the blade-downgoing side, the swirl velocity produces regions of downwash on the wing, diminishes the section lift and pivots the force vector further backward resulting in an increased section drag. The necessary condition for the wing drag reduction would require the backward rotated force in the propeller downwash region to be smaller than the forward rotated force in the propeller upwash region. Previous discussion reveals a natural tendency toward this condition since the force is augmented in the upwash region due to the local angle of attack increase and diminished in the downwash region due to the local angle of attack decrease.

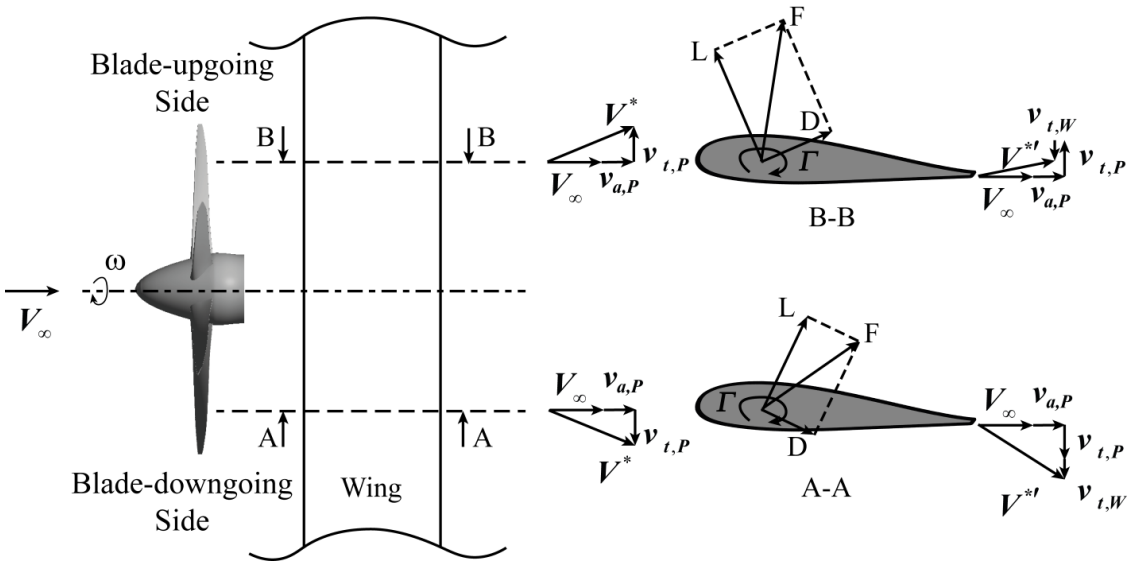

Figure 1.6 Tilting of wing section forces due to propeller-induced swirl velocity in a wing-mounted tractor propeller configuration. Also shown are the swirl velocity reduction on the blade-upgoing side and swirl velocity enhancement on the blade-downgoing side at locations behind the wing.

Moreover, in case of a tractor propeller configuration, the lift distribution of the wing is changed dramatically by the presence of the propeller slipstream. Since the induced drag of the wing is closely related to the lift distribution, the wing self-induced drag is also changed correspondingly. Thus for a tractor propeller configuration, both the propeller-induced drag and the wing self-induced drag should be incorporated in the evaluation of the wing performance. More details will be discussed later in Chapter 4.

The aerodynamic performance of wing swirl-recovery has been investigated both numerically and experimentally. In Kroo's work [23] where the wing lift distribution was

optimized for minimum induced drag in inviscid incompressible flow with constant lift, an increment of 6% in the generalized propeller efficiency, which is defined by

$$\eta_{general} = \frac{\left(T_P + T_{ind}\right)V_\infty}{P} \tag{1.2}$$

where T_{ind} is the induced thrust of the wing by propeller-wing interference, was found in example cases. Similarly, an efficiency gain by wing shape optimization was reported by Veldhuis [16] where both the chord length and twist distributions were optimized. Besides the numerical work, the benefit of wing swirl-recovery was verified experimentally for tractor-propeller configurations by many authors (e.g., Veldhuis [16] and Witkowski [42]).

For a wingtip-mounted tractor propeller configuration where the propeller has a rotation direction opposite to that of the wing tip vortex, the reduction of wing-induced drag (or equivalently the production of induced thrust) is achieved due to two reasons [43]: First, the rotor produces an upwash on the wing part immersed in the slipstream and consequently an induced thrust. This is similar to case of the blade-upgoing side of Figure 1.6. Second, the strength of the wing tip vortex diminishes due to the opposite rotating propeller. Thus at constant wing lift, the downwash induced by the tip vortex decreases over the wing span, and consequently a lower induced drag is found. For a wingtip-mounted pusher configuration where the propeller has a rotation direction opposite to that of the wing tip vortex, the thrust per unit power generated by the blade will be greater than the isolated case [44], which is analogous to the case of PSVs-propeller configuration. Although significant gains in propulsive efficiency may be gained for the tip-mounted propeller, this configuration is beyond the scope of this work. A detailed discussion of aerodynamic and aeroacoustic performance of wingtip-mounted propeller can be found in Ref. [45].

The different configurations of swirl recovery for propeller propulsion systems that were discussed above are summarized in Table 1.1 including four different devices (i.e., CRP, PSV, SRV and upstream or downstream wing/pylon). In modern turboprop aircraft, wing-mounted tractor propellers are commonly used. Considering the applications of swirl recovery system on these turboprop aircraft, swirl recovery by means of SRVs and the trailing wing is selected as the main focus of the current research (shaded in Table 1.1).

Table 1.1 Summary of configurations of swirl recovery for propeller propulsion systems (shaded is the focus of current research)

motion / location	rotational	stationary
in front of the propeller	CRP	PSV / upstream wing/pylon
behind the propeller		SRV / downstream wing/pylon

1.3 Motivation of current work

This study focuses on the swirl-recovery design of a SRVs-wing combination for tractor propeller propulsion systems. Despite previous efforts on the understanding of the swirl-

recovery mechanism, procedures for the parametric design of SRVs are not well developed. A cost-effective design process is required which can efficiently explore the design space of SRVs.

In addition, the design effort of SRVs in previous studies was made solely for uninstalled propeller configurations. When SRVs are introduced in a wing-mounted tractor-propeller configuration, both the SRVs and the wing have the ability of recovering swirl. No investigation has been performed yet on whether it is beneficial to have SRVs for better propulsive performance in the installed configuration.

It can be expected that an integrated SRV design taking the wing effect into account will most likely result in a performance benefit. For example, in the work of Stokkermans [46], SRVs designed for an isolated propeller were investigated in a wing-mounted configuration by means of Reynolds-averaged Navier-Stokes (RANS) simulations. Results have shown that the SRVs performance degrades significantly when mounted upstream of the wing. In such a configuration, flow separation occurred on the vanes due to deviation of inflow angle caused by the wing upwash; this was not accounted for in the design procedure. By manually adjusting the pitch angle of the vanes, potential benefit was gained in terms of either improved wing performance or generalized propeller efficiency.

As the above example illustrates, the process for an integrated swirl recovery design of SRVs-wing combination is still absent. Considering the SRVs designed for uninstalled propellers, the time-averaged inflow velocity to the vanes is assumed to be circumferentially uniform. However, in an installed configuration, the inflow velocity is circumferentially non-uniform due to the presence of the wing. This suggests that the vanes should have different shapes based on their circumferential positions. Moreover, due to the swirl recovery by SRVs, the slipstream has a reduced upwash/downwash effect on the wing performance. Both the magnitude and azimuthal distribution of swirl velocity will be changed in front of the wing so that the tilting of aerodynamic forces on the wing is altered correspondingly. Therefore, an integrated design should be performed combining both the SRVs and the wing performance.

1.4 Research questions and organization of dissertation

Following the motivation described above, the main questions in the current research can be formulated as follows:

What is the principal mechanism of swirl recovery by means of SRVs and a trailing wing? What is the optimum layout for the best swirl-recovery (and subsequent thrust-enhancement) performance for tractor-propeller propulsion systems?

Evaluating isolated swirl recovery and that in combination with the wing, three sub-questions are formulated as follows (Figure 1.7):

- For an uninstalled propeller propulsion system, what is the optimum SRV shape? What are the changes to the generalized propeller efficiency with addition of

SRV?

- For a wing-mounted tractor propeller configuration, what is the optimum wing shape for swirl-recovery purpose? What are the changes to the generalized propeller efficiency by wing shape optimization?
- For a wing-mounted tractor propeller configuration equipped with SRVs, what is the optimum layout of SRVs-wing combination for swirl-recovery purpose? What are the changes to the generalized propeller efficiency with addition of SRV?

Based on the research questions formulated above, the dissertation is organized as follows (Figure 1.7):

In Chapter 2, the working principle of an isolated propeller is explained, followed by the characterization of its slipstream flowfield. Two of the theoretical models that are used for the explanation will also be utilized during the SRV design process in Chapter 3 and Chapter 4. Considering the installed case, the effect of the downstream wing on propeller performance as well as the deformation of the slipstream is discussed. This discussion gives an indication of the interaction phenomena that should be incorporated when simulating the propeller-wing configuration later in Chapter 4.

In Chapter 3, the first research question is investigated. The working principle of SRVs is explained. A hybrid design framework of SRVs for uninstalled propeller is proposed. The design procedure is presented together with a test example, followed by the discussion of the experimental validation of the propeller-SRVs model.

In Chapter 4, both the second and the third research questions are approached. For the second research question, the working principle of swirl recovery of the trailing wing is demonstrated. An optimization framework of the wing shape is elaborated. A case study is performed at the cruise condition of typical turboprop aircraft.

For the third research question, the mechanism of swirl recovery of the SRVs-wing combination is explained. The interference between SRVs and wing is discussed. A design framework of SRVs-wing combination is proposed, and different SRVs-wing layouts are investigated and compared. An optimum SRVs-wing layout is identified which gives the optimal system performance.

In Chapter 5, the inspection of the third research question continues by RANS validation of the optimum SRVs-wing layout identified in the previous chapter. Comparisons are made between the low-fidelity design results and the high-fidelity RANS simulations in terms of wing and SRVs performances. An indication of propulsive benefit by addition of SRV in wing-installed configuration is given.

Ultimately, conclusions are drawn in Chapter 6 and recommendations are presented.

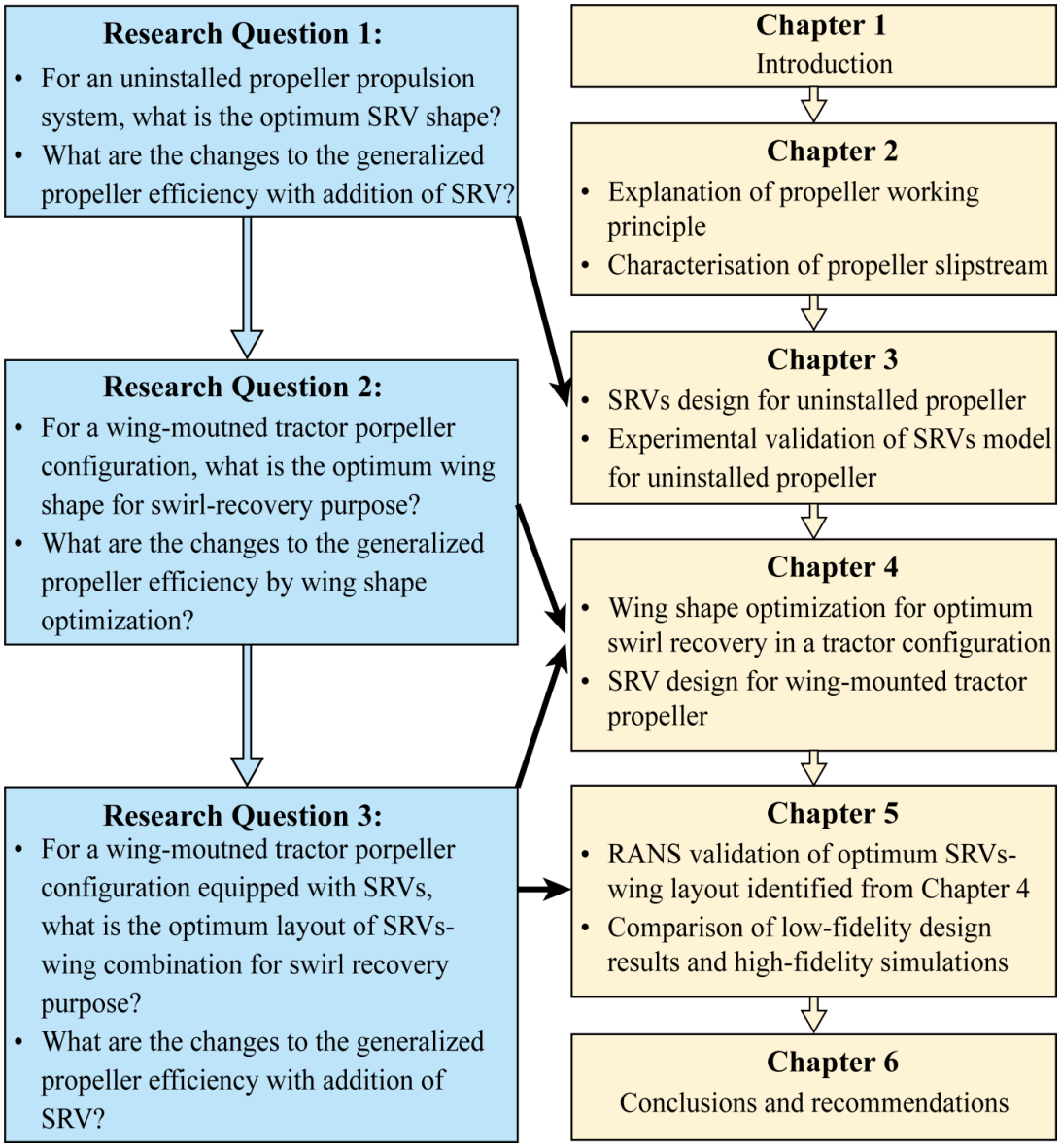

Figure 1.7 Research questions and organization of dissertation.

Chapter 2 Aerodynamic Characteristics of Propellers and Their Slipstream

2.1 Introduction

As discussed in the previous chapter, swirl recovery of propeller propulsion systems (and its subsequent propulsive benefit) is achieved by converting the angular momentum contained in the slipstream into axial momentum with the help of aerodynamic surfaces located behind the propeller. Prior to the design and optimization of these aerodynamic surfaces, a description of the flowfield in the slipstream is required.

Due to the rotation of the propeller, the slipstream generated by the propeller is unsteady relative to a stationary wing-fixed coordinate system. However, in this study, only the steady (or time-averaged) aerodynamic performance is considered. Thus, the flow quantities in the slipstream are circumferentially averaged (representing the time-averaged component) and assumed to vary only radially not circumferentially.

When having a stationary cylindrical coordinate system of which the axial direction is aligned with the propeller rotation axis, the velocity in the slipstream can be decomposed into three components, i.e. the axial, radial, and tangential component. The time-averaged inflow to a downstream SRV or wing consists of the radial profiles of these velocity components. Later in this chapter, the axial velocity profile is analyzed with the help of the propeller momentum theory in Sec. 2.2.1, and the tangential velocity profile is examined with the help of the propeller lifting line theory in Sec. 2.2.2. In order to establish a connection between the blade geometries and their aerodynamic performances, the blade element theory of propellers is discussed in Sec. 2.2.3. The terminology used for description of propeller aerodynamic performance is given in Sec. 2.3. In a wing-mounted tractor-propeller configuration, the characteristics of the slipstream are changed due to the presence of the downstream wing. Thus, the effects of the trailing wing on the propeller performance and the slipstream deformation are discussed in Sec. 2.4 and 2.5 respectively.

2.2 Working principle of propellers and characterization of their slipstream

2.2.1 Propeller momentum theory and axial-velocity profile in the slipstream

In order to analyze the axial-velocity profile in the slipstream, the momentum (or actuator disk) theory of propellers is used. This is done due to the simplicity of this theory that: 1) the geometric details of the propeller blades are neglected and replaced by an actuator disk (as introduced later in this section), 2) the flow is assumed to be steady, and 3) the rotational motion imparted to the fluid by propeller torque is neglected.

The momentum theory was first proposed by Rankine [47] and further developed by Froude [48]. Reviews of the historical developments of the momentum theory can be found in Ref. [49] and [50].

In the actuator disk theory, the propeller is represented by a discontinuity in the pressure distribution on an infinitely thin, permeable disk perpendicular to the freestream which has the same diameter as that of the original blades. The thrust loading of the propeller is assumed to be uniformly distributed over the actuator disk. A schematic representation of the actuator disk model for a propeller is shown in Figure 2.1. The outer boundary of the slipstream is defined by the streamtube that goes through the radius of the actuator disk. Far upstream, the freestream velocity is V_∞ and the static pressure is p_∞. Due to thrust production from the propeller, the flow is accelerated, reaching velocity of $V_\infty + aV_\infty$ and static pressure of p_1 in front of the disk. When passing the disk, the fluid experiences a static pressure increase of $\Delta p = p_2 - p_1$ as a consequence of the thrust production by $\Delta p = T_P / \pi R^2$ where R is the disk radius. Behind the propeller, the static pressure decays gradually to the ambient pressure p_∞ at infinite distance downstream of the propeller, and the velocity increases to $V_\infty + bV_\infty$ at infinity.

In order to preserve the mass flow as the velocity is increased through the actuator disk, the slipstream contracts in front and behind the propeller disk. The contraction ratio, which is defined by the ratio of the slipstream diameter at infinite distance downstream to the actuator disk diameter, is related to the propeller thrust. A higher thrust generation of the propeller would result in a larger contraction ratio. Due to the contraction of the slipstream, when performing SRV design, the diameter of the vanes should be explored in order to achieve the best swirl recovery and propulsive performance. Furthermore, a radial component of the velocity in the slipstream is present due to the contraction. The magnitude of the radial velocity is determined by the contraction ratio and thus the loading of the propeller.

With the help of the actuator disk theory, the influence of a propeller to the surrounding flowfield can be represented by a distribution of momentum source at the location of the propeller while neglecting the geometric details. When representing the propeller by an actuator disk in the three-dimensional computational fluid dynamic (CFD) simulations, the computation time is reduced significantly compared to the full representation of the rotors.

This approach is used later in Chapter 4 when simulating the propeller-wing configurations. The actuator disk model used in Chapter 4 is generalized in the sense that besides the axial momentum generated by the propeller, the tangential momentum is also included. Further details will be given in Chapter 4.

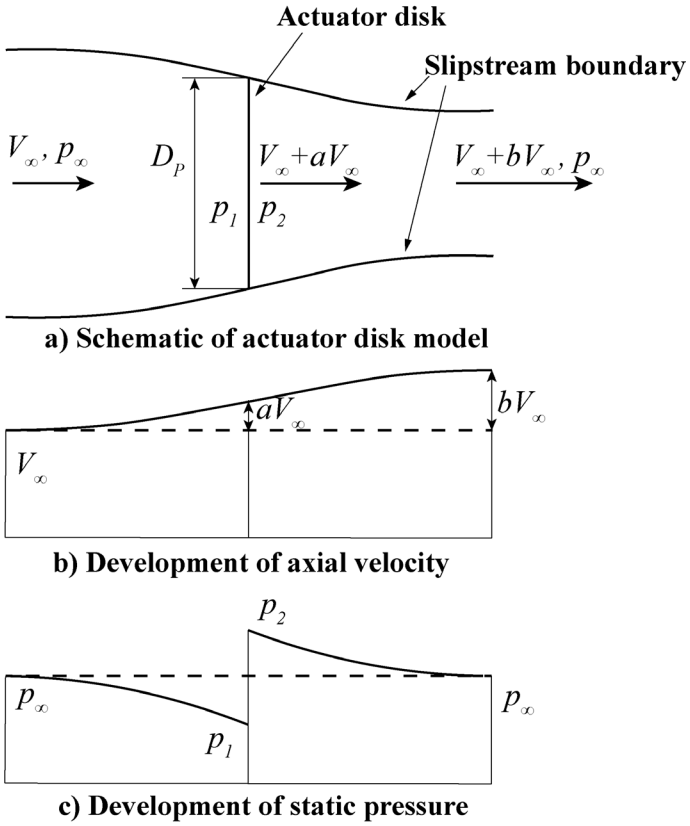

Figure 2.1 Schematic of propeller actuator disk model.

2.2.2 Propeller lifting line theory and tangential-velocity profile in the slipstream

In order to analyze the tangential-velocity profile, the lifting line theory of propellers is used. This theory was first developed by Prandtl [51] for fixed wings and extended by Betz [52] for rotary wings such as propellers. According to this model, the propeller blade is represented by a vortex filament which is bound along the blade's quarter chord line (Figure 2.2). Following the Helmholtz's theorem [53] that a vortex cannot end in a fluid, when the bound vorticity varies in its magnitude along the radius, a free vortex filament is shed from the lifting line. The magnitude of the shed vortex filament is equal to the change in the magnitude of the bound vorticity.

When describing the magnitude of vorticity, the circulation (Γ) is often used. The circulation is defined as the line integral of the velocity vector along a closed contour. It also equals to the surface integral of the normal component (to the surface) of vorticity vector over the area enclosed by that contour. For a typical propeller represented by a lifting line, the bound circulation gets its maximum value $\Gamma_{\max}$ at around 70–75% radius. At radial positions inside of the location where Γ_{max} occurs, due to the positive gradient of $d\Gamma / dr$, the wake

vortex filament shed by the blade ($\Gamma_{wj} = \Gamma_{j+1} - \Gamma_j$) has an axial component pointing downstream and a circumferential component with the opposite direction of propeller rotation (Figure 2.2). Similarly, at radial positions outside of the location where Γ_{max} occurs, due to the negative gradient of $d\Gamma / dr$, the wake vortex filament ($\Gamma_{wi} = \Gamma_{i+1} - \Gamma_i$) has an axial component pointing upstream and a circumferential component with the same direction of propeller rotation.

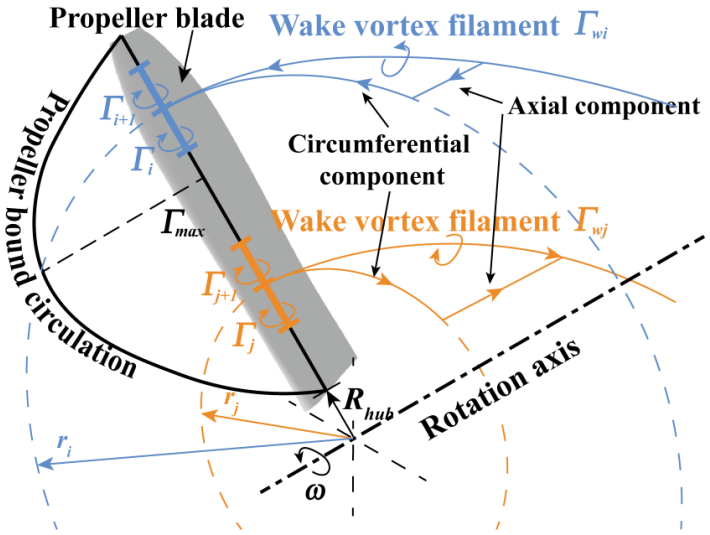

Figure 2.2 Lifting line model of propellers. In this case, a wake vortex filament of strength $\Gamma_{wi} = \Gamma_{i+1} - \Gamma_i$ is released at a radial position r_i, and another wake vortex filament of strength $\Gamma_{wj} = \Gamma_{j+1} - \Gamma_j$ is released at a radial position r_j.

The shed vortex filaments constitute a wake vortex sheet where there can be neither forces, nor a discontinuity of pressure or normal velocity across the vortex sheet. Only a discontinuity of tangential velocity (tangential to the wake vortex sheet) is present through the vortex sheet. In terms of representation of the wake with a quantitative model, there is a hierarchy of wake models available, ranging from a simple prescribed-wake model (not force-free therefore) to a sophisticated free-wake model [54]. In the free-wake model, the wake is discretized into vortex panels, and these panels are convected at local velocities of the flowfield. A series of collocation points is specified on the panels, of which the locations are resolved in order to meet the continuity and discontinuity requirements mentioned in the previous paragraph. As a comparison, in the prescribed-wake model, the wake trajectories are pre-described based on the rotor geometric and operational parameters. The rolling-up of the tip vortices as well as the distortion of the wake shape has been neglected. Thus, the shape of the wake vortex sheet is uniquely related to the distribution of bound circulation of the propeller blade.

The induced velocity in the propeller slipstream can be considered to be the resultant velocity at a point induced by the entire system of the bound and wake vortices. As discussed by Veldhuis [16], when assuming an infinite number of blades, the bound vortex induces no axial but only tangential velocity in the slipstream. In front of the propeller, the tangential velocity induced by the bound vortex is compensated by the component induced by the wake vortex sheet such that the tangential velocity is zero everywhere in front of the propeller as

shown in Figure 2.3. From the propeller plane onwards, the tangential velocity profile remains constant.

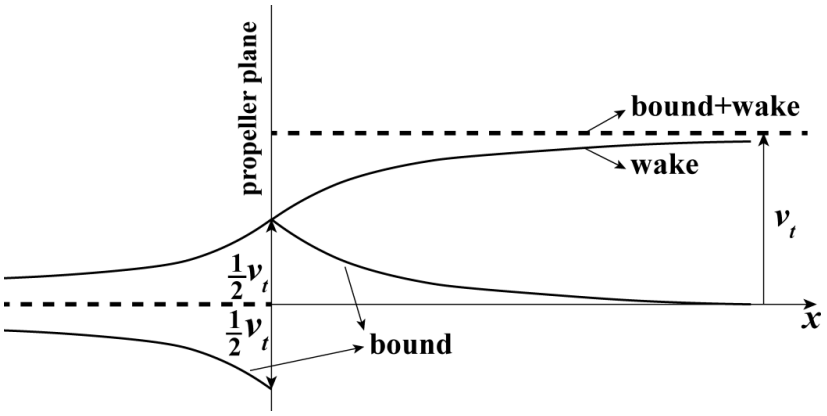

Figure 2.3 Contributions of bound and wake vorticity (solid lines) to the tangential induced velocity in the propeller slipstream, and the resultant component (dashed line).

So far, the generation of both the axial and the tangential velocities are analyzed while not explicitly considering the effect of viscosity. When taking the viscous effect into account, a boundary layer is generated surrounding the blade surface and shed into the slipstream. Therefore, the blade wake, instead of being a shear layer which is infinitely thin as represented in the lifting line model, is of a finite thickness in reality. Due to the viscous effect, the blade is "pulling" the air along with it, such that the viscous blade wake is characterized by lower axial velocity and higher tangential velocity compared to the flow outside the wake. Thus, the flow quantities in the slipstream are circumferentially varying. However, when presenting the flow quantities later in this dissertation, they are circumferentially averaged due to the reason that in this study, only the time-averaged aerodynamic performance is dealt with (as mentioned previously in Sec. 2.1). A typical radial distribution of the axial and tangential induced velocities directly behind the propeller obtained from viscous analysis is presented in Figure 2.4. Due to the non-uniform radial distributions of thrust and torque, the flow quantities exhibit a strong gradient along the radius.

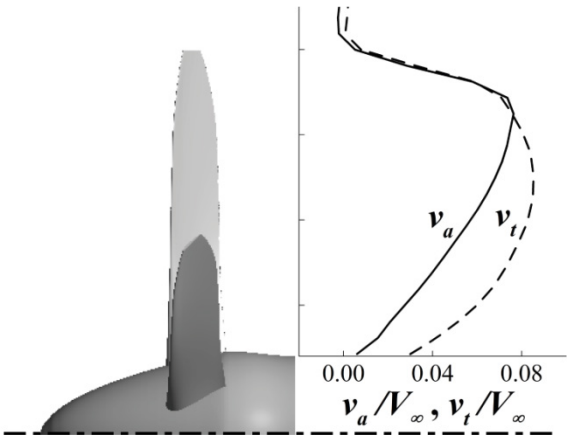

Figure 2.4 Typical radial distributions of axial and tangential induced velocities directly behind a propeller.

2.2.3 Propeller blade element theory and thrust production

The blade element theory of propellers establishes a connection between the blade geometries and their aerodynamic performances. This theoretical model is introduced here in order to: 1) further understand the working principle of propellers, and 2) serve as a building block of theoretical models that will be used in the SRV design process.

In the blade element theory, the propeller blade is cut into elements by streamtubes along the radius. A blade element with a chord length of c and a radial length of dr, located at radius r from the propeller axis, is shown on the left of Figure 2.5. The radial component of velocity is neglected such that the flow around the blade element is assumed to be two dimensional.

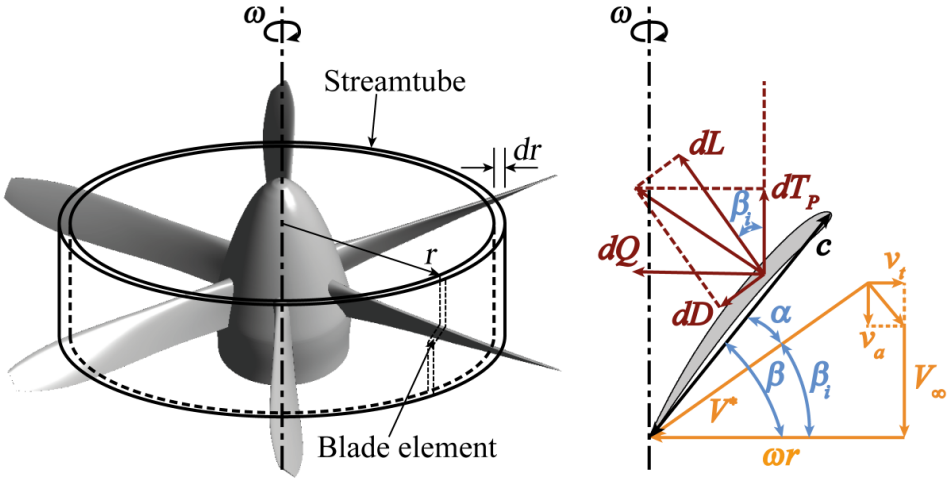

Figure 2.5 Left: A blade element at radius r of a six-bladed propeller; right: velocity and force diagram of the blade element at radius r.

On the right of Figure 2.5 illustrates the velocity and force diagram of the blade element at radius r. Three velocities, i.e. the freestream velocity V_∞, the angular velocity due to rotation ωr (ω is propeller rotation speed), and the axial and tangential induced velocities v_a and v_t, add vectorially to produce a resultant effective velocity V^*. The effective velocity has a magnitude of:

$$V^* = \sqrt{(V_\infty + v_a)^2 + (\omega r - v_t)^2} \tag{2.1}$$

and a pitch angle of:

$$\beta_i = \text{atan}\left(\frac{V_\infty + v_a}{\omega r - v_t}\right) \tag{2.2}$$

Denoting the geometric pitch angle of the blade element as β, the angle of attack of the blade element is then determined by $\alpha = \beta - \beta_i$.

Since the radial component of velocity is neglected, the aerodynamic coefficients of two-dimensional airfoils can be used to predict the elementary lift (dL) and drag (dD) forces as

[55]:

$$dL = \frac{1}{2}\rho V^{*2} C_l c \, dr \tag{2.3}$$

$$dD = \frac{1}{2}\rho V^{*2} C_d c \, dr \tag{2.4}$$

where C_l and C_d are the lift and drag coefficient of the blade element airfoil. The elementary thrust (dT_P) and torque (dQ where Q is propeller torque) can then be expressed as:

$$dT_P = dL\cos\beta_i - dD\sin\beta_i \tag{2.5}$$

$$dQ = (dL\sin\beta_i + dD\cos\beta_i)r \tag{2.6}$$

The overall thrust and torque acting on the blade is the integral of the elementary thrust and torque along the radius as:

$$T_P = N\int_{R_{hub}}^{R} (dL\cos\beta_i - dD\sin\beta_i)\, dr \tag{2.7}$$

$$Q = N\int_{R_{hub}}^{R} (dL\sin\beta_i + dD\cos\beta_i)\, r\, dr \tag{2.8}$$

where R_{hub} is hub radius, and N is number of propeller blades.

It should be noted that various models can be used for the calculation of the induced velocities at blade sections [56]. The lifting line theory discussed in Sec. 2.2.2 is one of the examples. In the lifting line theory, both the strength and the shape of the wake are determined by the bound circulation distribution. The induced velocities on blade sections are determined by the wake strength and shape. Once the induced velocities are known, the aerodynamic forces can be obtained from the blade element theory based on the two-dimensional section profiles, after which the bound circulation distribution can be obtained. In this way, a set of non-linear equations is formed that can be solved iteratively. The combination of the lifting line theory and the blade element theory is used during the SRV design process in Chapter 3 and Chapter 4.

2.3 General terminology for isolated propeller aerodynamic performance

Following the dimensional analysis as presented in Appendix A, the propeller aerodynamic performance is typically represented by the thrust coefficient $C_{T,P}$, the torque coefficient C_Q, the power coefficient C_P, and the efficiency η_P, which are defined as:

$$C_{T,P} = \frac{T_P}{\rho n_s^{\,2} D_P^{\,4}} \tag{2.9}$$

$$C_Q = \frac{Q}{\rho n_s^{\,2} D_P^{\,5}} \tag{2.10}$$

$$C_P = \frac{P}{\rho n_s^{\,3} D_P^{\,5}} \tag{2.11}$$

$$\eta_P = \frac{J \cdot C_{T,P}}{C_P} \tag{2.12}$$

as a function of the advance ratio J and the blade pitch angle $\beta_{0.7R}$ at the operating Reynolds number Re_{tip} and Mach number Ma_{tip}, which are defined as:

$$J = \frac{V_\infty}{n_s D_P} \tag{2.13}$$

$$Re_{tip} = \frac{D_P^2 n_s}{\upsilon} \tag{2.14}$$

$$Ma_{tip} = \frac{D_P n_s}{a_{SoS}} \tag{2.15}$$

where n_s is propeller rotation frequency, υ is air kinematic viscosity, and a_{SoS} is speed of sound in air.

The advance ratio J is the ratio of the propeller tip speed with the freestream velocity. Thus, J is indicative of the relative inflow angle observed from a propeller-fixed coordinate system, and is related to the sectional angle of attack and the blade loading. For a given propeller set at a constant pitch angle $\beta_{0.7R}$, the blade loading (or thrust production) can be adjusted by changing the advance ratio. The thrust coefficient is a measure of the propulsive force generated by the propeller. When including the SRV in the propulsion system, the thrust coefficient can be generalized by defining the thrust coefficient of the SRVs as:

$$C_{T,V} = \frac{T_V}{\rho n_s^{\,2} D_P^{\,4}} \tag{2.16}$$

where T_V is the thrust of SRVs. Therefore, the generalized propeller efficiency can be defined as a function of the generalized thrust coefficient ($C_{T,P} + C_{T,V}$) and the power input from the propeller (C_P) as:

$$\eta_{general} = \frac{J \cdot (C_{T,P} + C_{T,V})}{C_P} \tag{2.17}$$

The thrust production of SRVs will later be discussed in the following chapters.

As an example of the typical propeller performance, Figure 2.6(a) presents the measured performance curves of a six-bladed propeller (Figure 3.5) at a constant blade pitch angle (

$\beta_{0.7R} = 30°$) and Reynolds number ($Re_c^{0.7R} = V_\infty c_{0.7R} / \upsilon = 5.90 \times 10^4$ where $c_{0.7R}$ is the blade chord length at radial position of 0.7*R*). Both the thrust coefficient and the power coefficient increase with the decreasing of the advance ratio. At higher loading conditions of $J < 0.9$, $C_{T,P}$ and C_P flatten out due to the separation of the boundary layer on the blades. The efficiency usually peaks at a high advance ratio close to the windmilling condition, in this case around $J = 1.0$.

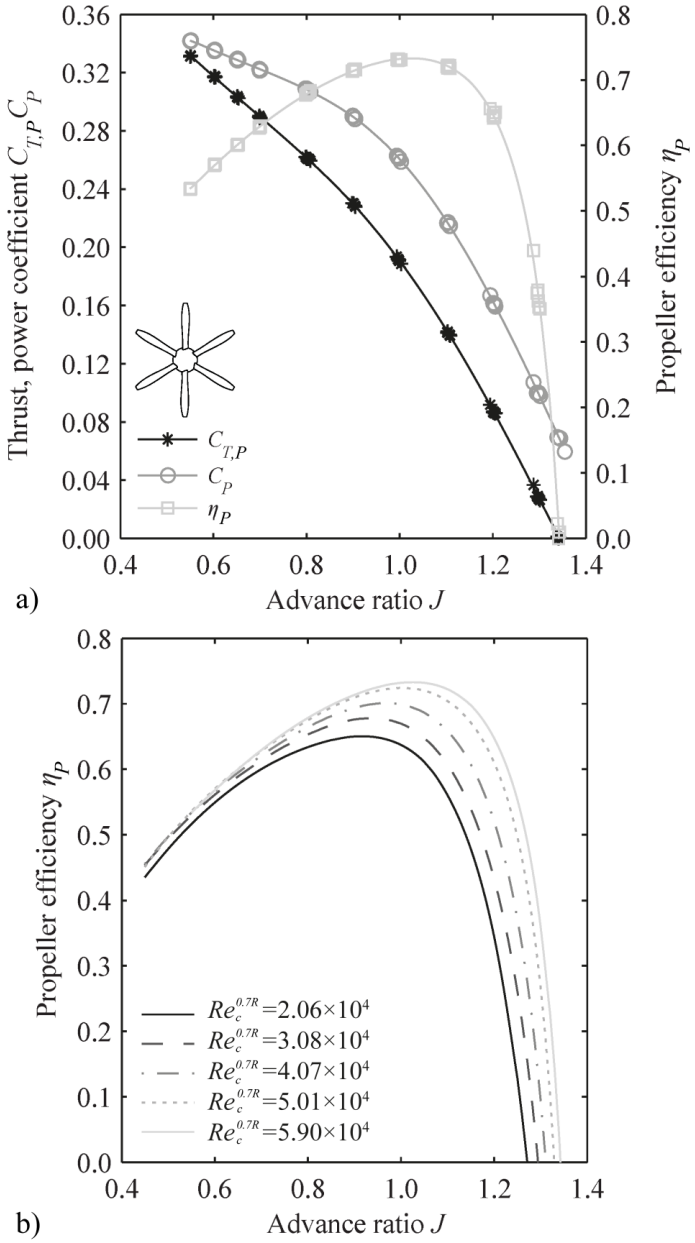

Figure 2.6 Example performance curves measured with the propeller illustrated in Figure 3.5 at $\beta_{0.7R} = 30°$: a) propeller performance operating at $Re_c^{0.7R} = 5.90 \times 10^4$; b) effect of Reynolds number on propeller efficiency. (Adapted from Sinnige [45])

The effect of the Reynolds number on the propeller efficiency is shown in Figure 2.6(b). The efficiency curve shows a dependency on the Reynolds number, which can be explained as follows. With increasing Reynolds number, the boundary-layer thickness on the blades decreases. Thus, the de-cambering effect is weaker at higher Reynolds numbers due to the inverse relationship of the boundary thickness with the Reynolds number, which leads to the

increase of the sectional lift and the reduction of sectional drag. As a result, the thrust increases more rapidly than the torque, and the propeller effciency increases and shifts toward the windmilling advance ratio with increasing Reynolds number.

Nevertheles, the general shape of the efficiency curve remains the same for all the measured Reynolds numbers. Thus, the investigations based on the scaled propeller model in the following chapters (operating at a lower Reynolds number compared to that of real aircraft) can be related to the applicatons on real aircraft by applying corrections (for Reynolds number effect) such as those discussed in Ref. [57]. The same conclusion also holds for compressibility effect up to flight Mach number at which shock waves start to form on the propeller blades. For the operating conditions discussed in this work, such conditions will not occur.

2.4 The effect of the trailing wing on propeller performance

In a wing-mounted tractor-propeller configuration, the characteristics of the slipstream are altered due to two effects:

- the blade loading and thus the flowfield in the slipstream are altered by the presence of the wing;
- the slipstream is deformed due to its interaction with the wing surface;

These two phenomena will be elaborated by the following two sections. In this section, the performance aspect of the trailing wing influence on the propeller is analyzed.

For a typical turboprop aircraft, the propulsion system is installed on the wing. Due to the upwash induced upstream of the wing, the up-going blade experiences a local angle of attack decrease (shown on top-left of Figure 2.7) which leads to a decreased thrust and torque. As a comparison, the down-going blade has a local angle of attack increase (shown on top-right of Figure 2.7), resulting in an augmented thrust and torque. The overall effects on the blade loading are illustrated at the bottom of Figure 2.7 by providing a comparison of the total pressure jump through the propeller disk with and without the trailing wing. Compared to the uninstalled case, the total pressure jump on the blade up-going side is lower and on the blade down-going side is higher.

Despite of this change, the effect of the downstream SRVs and wing on propeller performance is neglected in Chapter 4 when simulating the propeller-SRV-wing configuration. This is done for two reasons. Firstly, since only a component of the wing-induced velocity acts to affect the blade angle of attack, the variation of propeller performance is expected to be small upon time-averaging as observed from experimental tests by Witkowski [58]. Secondly, since the objective of this study is to compare the swirl recovery performance from the wing and the SRVs, it is necessary to have the same velocity input for both cases. Due to the two reasons discussed above, during the design process of swirl recovery system, the amount of the angular momentum in the slipstream is assumed to be constant by neglecting the perturbations to propeller performance from the addition of SRV and/or wing.

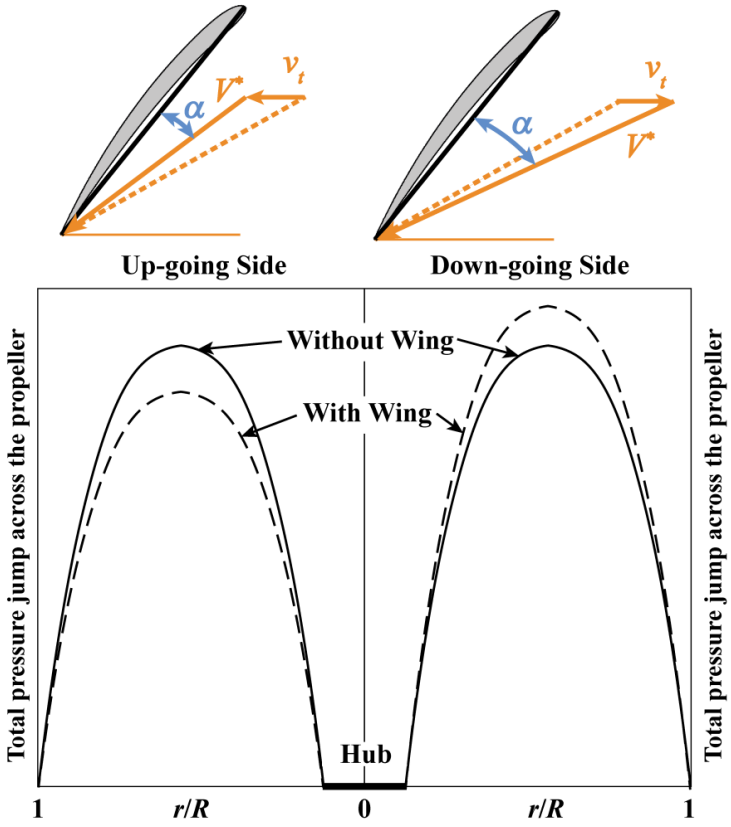

Figure 2.7 Top: variation of sectional angle of attack due to wing-induced velocity on the blade up-going side (left) and down-going side (right); bottom: comparison of total pressure jump across the propeller with and without the trailing wing.

2.5 The effect of the trailing wing on slipstream deformation

Concerning the deformation of the propeller slipstream due to the presence of the trailing wing, non-negligible effects were noticed by many authors [59,60]. Two chronological stages of slipstream deformation are identified. In the first stage ahead of the wing, the slipstream is exposed to the combined flowfield of the freestream and wing-induced velocities. In the second stage, the slipstream is cut by the wing surface. The vorticity embedded in the slipstream interacts with the wing solid surface, generating self-induced deformation. The self-induced deformation works together with the deformation due to wing-induced velocities. As a consequence, when moving along the wing surface, the slipstream experiences spanwise, chordwise and vertical displacements. The mechanism of slipstream deformation during the two stages is detailed below.

In the first stage, as shown in Figure 2.8, due to the wing-induced velocity (an upwash in vertical direction) ahead of the wing, the slipstream exhibits an upward displacement. When the slipstream gets closer to the wing leading edge, the displacement has a higher curvature due to the stronger wing-induced velocities.

In the second stage, there are two main reasons of deformation when the slipstream interacts with the wing surface, i.e., the deformation due to wing-induced velocities (the same situation as in stage one but at a closer distance) and deformation due to vorticity-surface interaction.

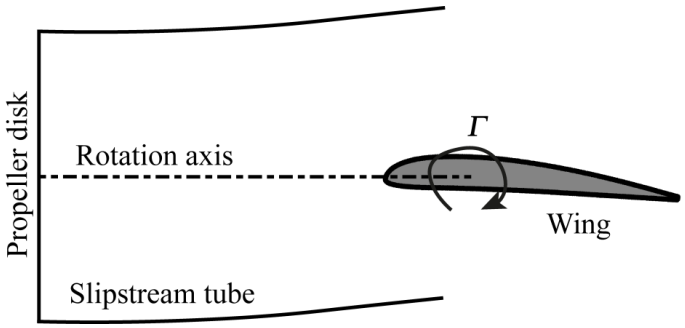

Figure 2.8 Slipstream deformation ahead of the wing due to the wing-induced upwash. The propeller rotation axis goes through the wing quarter-chord line.

2.5.1 Deformation due to wing-induced velocities

In the potential-flow theory where the flow is assumed to be frictionless and irrotational, the wing surface can be represented by distributions of sources and sinks (interpreting wing thickness), and doublets (interpreting wing loading) [61]. The velocity and the correlated pressure fields are the results of the potential flow solution which describes the wing surface as well as the rest of the flow field. When approaching the wing leading edge, the slipstream is deflected by the induced velocities from the wing singularities (sources and doublets), cut by the wing solid surface and flows around the wing leading edge as sketched in Figure 2.9. This phenomenon was observed experimentally by Chiaramonte [60] and described as "expansion" of the slipstream in the vertical direction. Further downstream from the leading edge, on both the suction and the pressure sides, the flow is accelerated from the leading edge up to the minimum-pressure point due to the decrease of the pressure, and decelerated afterwards due to the increase of the pressure (Figure 2.9). However, because of the wing loading, the amount of acceleration and deceleration on two sides is different. This results in a chordwise displacement of the slipstream when reaching the trailing edge of the wing. For example, the chordwise misalignment of the tip vortices on the wing upper and lower surfaces was observed experimentally by Johnston [62].

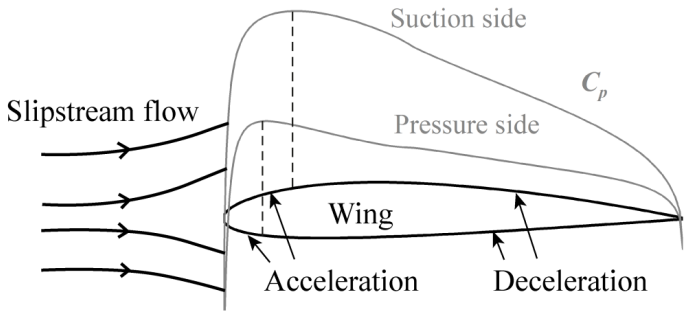

Figure 2.9 Vertical displacement of the slipstream surrounding the wing leading edge (left), and the chordwise acceleration/deceleration of the slipstream due to wing-induced velocities along the wing surface (right).

Besides the chordwise displacement, the slipstream also experiences a vertical displacement. The slipstream, which is an air jet, tends to stay attached to the wing surface in the vertical direction. Thus, the slipstream experiences a vertical displacement due to the convexity and concavity of the wing surface. For example, this phenomenon was observed experimentally in Ref. [63].

2.5.2 Deformation due to the interaction between vorticity in slipstream and wing surface

The flowfield induced by singularities with presence of solid boundaries can be simulated by "method of images" [64]. When the vorticity embedded in the slipstream interacts with the wing surface, only the component of vorticity vector that is parallel to the surface imposes an image vorticity vector by the wing due to the image effect.

Close to the leading edge of the wing, the normal vector of a small portion of the wing surface has a major component in horizontal direction. The circumferential component of the wake vortex filaments interacts with this part of the wing by the image effect as illustrated in Figure 2.10. At radial positions inside of the location where $\Gamma_{\max}$ occurs, the effect that the solid wall has upon the flow field can be described with the help of a virtual image vortex Γ_{wj}' inside the wing surface, which induces an inward velocity on the wake vortex filament Γ_{wj}. At radial positions outside of the location where $\Gamma_{\max}$ occurs, the virtual image vortex representing the wing surface Γ_{wi}' induces an outward velocity on the wake vortex filament Γ_{wi}. Consequently, the wake is stretched along the spanwise direction. However, since only a small portion of the wing surface has a normal vector with major component in horizontal direction, the interaction between the circumferential component of the wake vortex filaments and wing surface happens within a very short period of time and thus has limited influence on the slipstream deformation.

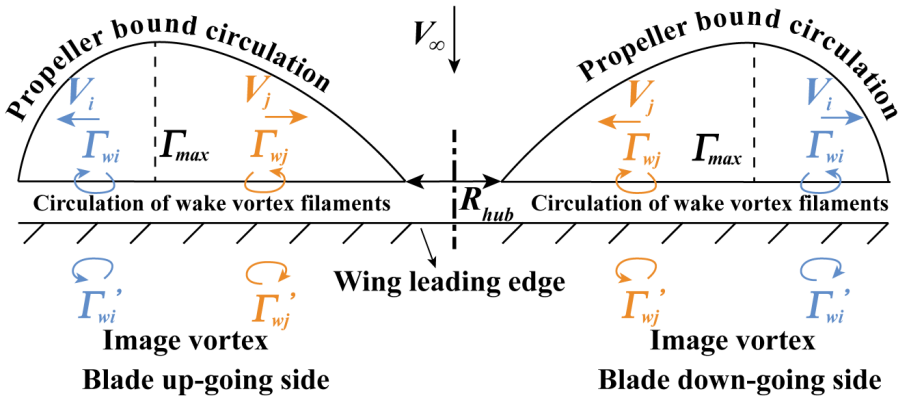

Figure 2.10 Slipstream deformation due to interaction between the circumferential component of wake vortex filaments and the wing solid surface (top view).

Downstream of the wing leading edge, the interaction between the axial component of the wake vortex filaments and the wing surface plays a dominant role in slipstream deformation (Figure 2.11). Concerning this type of interaction, there are four different cases depending on the circumferential location (blade up-going or down-going side) and vertical position (above or below) relative to the wing surface. As was shown in Figure 2.2, the axial component of the wake vortex filament Γ_{wj} / Γ_{wi} points downstream/upstream at radial positions inside/outside of the location where $\Gamma_{\max}$ occurs. On the blade up-going side above the wing surface at inner radius, Γ_{wj} generates an image vortex Γ_{wj}' pointing upstream,

which induces an outward velocity on Γ_{wj}. At an outer radius, Γ_{wi} generates an image vortex Γ_{wi}' pointing downstream, inducing an inward velocity on Γ_{wi}. Following the same procedure, the wing lower surface and blade down-going side can be analyzed.

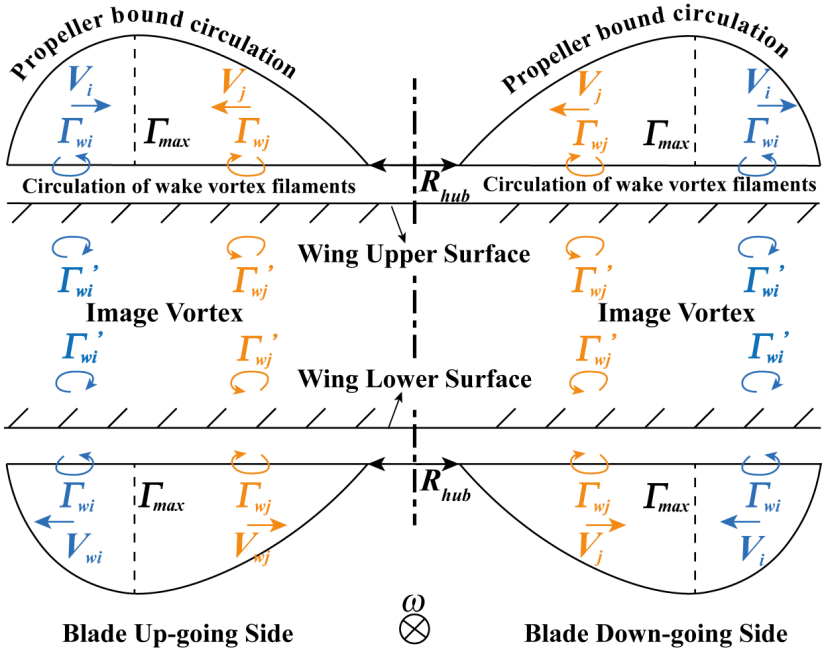

Figure 2.11 Slipstream deformation due to interaction between the axial component of wake vortex filaments and the wing surface (front view).

From the above analysis, it can be concluded that on the blade advancing sides (lower surface on the blade up-going side and upper surface on the blade down-going side), the slipstream tends to flatten out along the span on the wing surface, and on the blade retreating sides (upper surface on the blade up-going side and lower surface on the blade down-going side), the slipstream tends to contract along the span on the wing surface. Figure 2.12 shows an example (taken from the material discussed in Chapter 4) of the computed slipstream deformation represented by the total pressure distribution behind the wing. Both the flattening out on the blade advancing sides and the contraction on the blade retreating sides of the slipstream can be observed. This conclusion of the slipstream spanwise displacement is also consistent with the experimental observations of the rotor tip-vortex trajectory on the wing surface from Chiaramonte [60] and Johnston [62], and the total pressure measurements of slipstream behind the wing from Veldhuis [16].

As discussed above, the propeller slipstream is deformed by the presence of the wing. In a tractor propeller-wing configuration, the performance of the downstream wing is influenced by the slipstream to a great extent. Thus, when evaluating the wing performance with a tractor propeller in Chapter 4, the interaction between the slipstream and wing surface should be modeled adequately. Moreover, when designing SRVs for installed propeller, it is also necessary to simulate the slipstream-wing interaction in order to provide an accurate input for SRV design process. This is especially important when the SRVs are located behind the wing, since the deformation of slipstream is severer behind the wing than in front of the wing. The simulation of propeller-wing configuration is detailed later in Chapter 4.

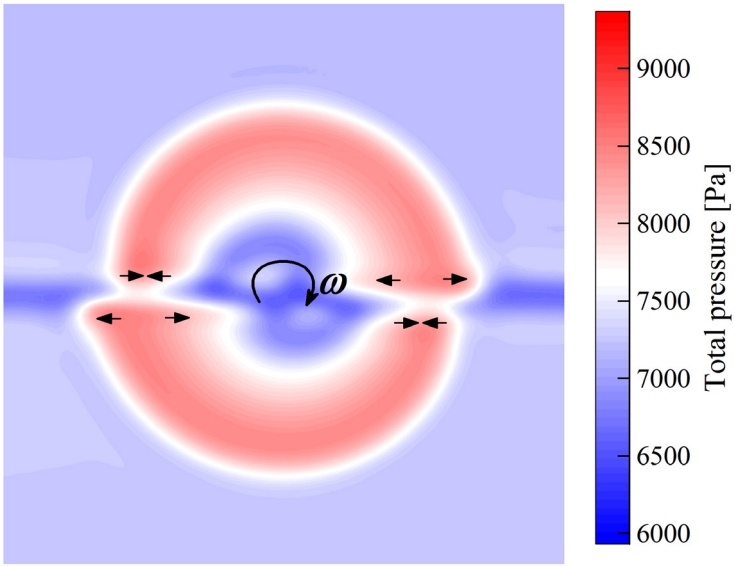

Figure 2.12 An example of the computed slipstream deformation represented by the total pressure distribution behind the wing. The arrows illustrate the flattening out of slipstream on the blade advancing sides and the contraction of slipstream on the blade retreating sides.

2.6 Conclusion

In this chapter, the working principle of propellers is explained and the propeller slipstream is characterized by the utilization of the models based on momentum theory, the blade element theory, and the lifting line theory.

For swirl-recovery purpose, the aerodynamic surfaces inside the slipstream should be designed based on the characteristics of the slipstream. Thus, an accurate description of the flowfield surrounding the propeller is required which should provide a good estimation of both the overall propeller performance and the induced-velocity distributions in the slipstream. The methodology used in order to achieve this will be discussed in Chapter 3. Moreover, in the design process of SRVs, the combination of the blade element theory and the lifting line theory is utilized, which will be detailed in Chapter 3.

For the installed propeller case, the effects of the trailing wing on the propeller performance and the slipstream deformation are presented in qualitative sense. However, the effect of the trailing SRVs and wing on propeller performance is ignored when simulating the propeller-SRV-wing configuration in Chapter 4. This enables the establishment of a fast and computationally-efficient design process of the swirl-recovery components (i.e., the SRVs and the wing). The slipstream deformation, on the other hand, is taken into account in order to obtain reasonable evaluation of the performance of these components.

In the next chapter, the SRV design process for uninstalled propeller propulsion systems based on the lifting line theory and the blade element theory discussed in this chapter is presented. An experimental test for validation of the design procedure is carried out.

Chapter 3 Design and Experimental Validation of Swirl-Recovery Vanes for Uninstalled Propeller Propulsion Systems

3.1 Introduction

As mentioned in Sec. 1.2, the SRV concept was proposed by NASA in the late 1980s and revisited recently by research groups at Delft University of Technology and Northwestern Polytechnical University. Despite the previous effort, procedures for the parametric design of SRVs are not well developed. In the numerical SRV design process performed by Wang [38] and Stokkermans [39], the design problem was set up by combining a blade analysis tool with an optimization routine. However, the results of optimization routines are susceptible to the definition of the initial point. Furthermore, a global optimum design can typically not be guaranteed, but only assumed after performing a series of optimizations with different initial designs or by utilizing a global optimization algorithm. Both approaches will lead to an increase in computational time [65], thus making them unsuitable for parametric design of SRVs.

Because of the long history and wide application of aerial and marine propellers, the design process of propellers is well developed. A variational design approach used to design marine propellers [66] can be used for SRV design due to its fast turnaround time and reasonable accuracy. In this approach, as described by Hildebrand [67], an auxiliary function is formed, which includes both the objective function and the constraints multiplied by a Lagrange multiplier. By setting the partial derivatives of the auxiliary function to the design variables to zero, the objective function is minimized while respecting the constraints. As a result, the optimum is obtained without applying a dedicated optimization routine, thus reducing computational time. This variational approach is appropriate for parametric study due to the fact that the geometric details are not necessarily needed at the initial design stage.

This chapter presents a hybrid framework for SRV design following a variational approach based on the optimum circulation distribution on the SRVs, which allows for a fast

---

The work of this chapter has been published entitled “Design and Experimental Validation of Swirl-Recovery Vanes for Propeller Propulsion Systems” in *AIAA Journal*, Vol. 56, No. 12, 2018, pp. 4719-4729.

computation and optimization of the final vane shape. A universal explanation of swirl recovery mechanism is presented. Prior to the SRV design procedure, the flow around the isolated propeller is simulated by a RANS-based solver and given as input to the SRV design tool. The model is coupled with a low-fidelity lifting-line code to produce a relatively good prediction of blade forces, while maintaining the efficiency and feasible turn-around times for quick convergence of the optimal blade parameters. To allow for a subsequent validation of the design method, a set of SRVs was designed for a six-bladed propeller and tested in a low-speed wind tunnel. The measured propulsive performance of the SRVs is compared to the numerical predictions. The computed velocity profiles downstream of the propeller with and without SRVs installed are validated by PIV measurements.

3.2 Mechanism of swirl recovery

The mechanism of swirl recovery by SRV and wing was explained separately in Sec. 1.2 by investigating the induced velocities of the blade/wing element. In this section, a universal explanation of swirl recovery mechanism is provided utilizing the lifting line theory discussed in Sec. 0. The viscous forces exerted on the blades are neglected for simplicity.

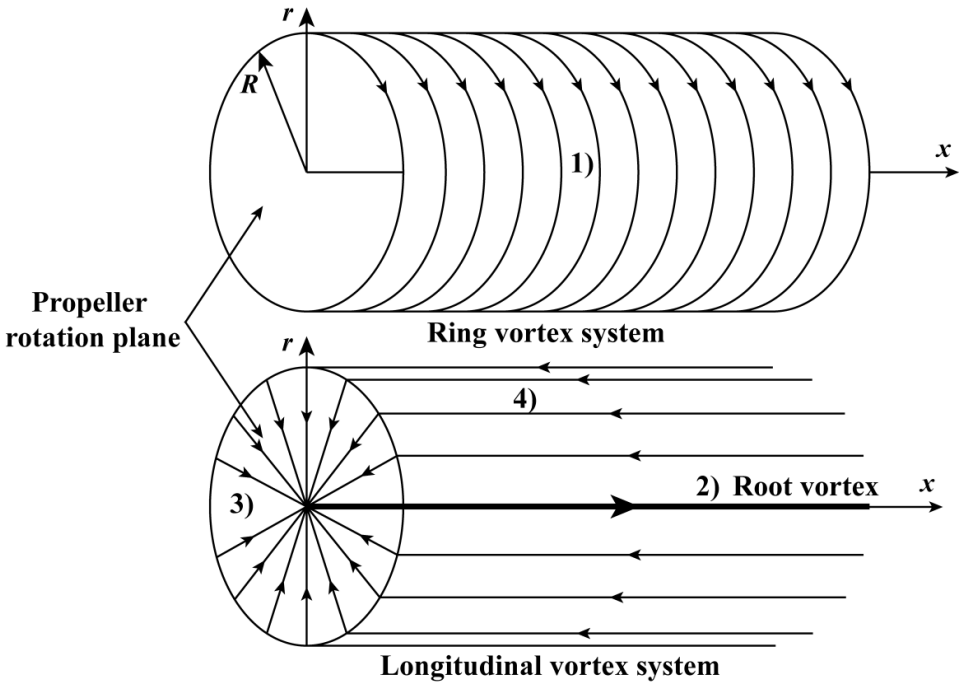

Figure 3.1 Representation of the propeller by the combination of the ring vortex system and the longitudinal vortex system (neglecting slipstream contraction for simplicity). (Reproduced from Conway [68])

In the lifting line theory, the instantaneous velocity field in the slipstream is related to the instantaneous vorticity distribution via the Biot-Savart law. On the other hand, the time-averaged induced velocity field is determined by the time average of the vorticity distribution. In case of a propeller, the time-averaged induced flowfield can be represented by that induced by superposition of (Figure 3.1):

1) a vortex tube consisting of ring vortices distributed over a contracting tube (though contraction is neglected in Figure 3.1 for simplicity) which result from the circumferential

component of the wake vorticity;

2) a constant-strength root vortex along the axis of symmetry which is the axial component of the wake vorticity shed at the blade root;

3) a surface distribution of vorticity on the slipstream surface normal to the ring vortices which is the axial component of the wake vorticity shed at the blade tip;

4) a distribution of radial vorticity on the propeller rotation plane representing the lifting lines of the propeller blades.

The longitudinal vortex system, which consists of 2), 3) and 4), is responsible for the generation of swirl velocity in the slipstream, while the ring vortex system 1) is responsible for the generation of axial and radial velocities in the slipstream.

When conceptualizing the mechanism of swirl recovery for a propeller propulsion system, only one of the blades is considered. The propeller has a counter-clockwise rotation when seen from behind as sketched in Figure 3.2. Since only the swirl velocity is of interest, the ring vortex system is neglected and the propeller blade is simplified into a horseshoe vortex with strength of Γ_1, where the root and tip vortex filaments are aligned with the freestream velocity. The bound vorticity vector points inward, while the root and tip vorticity vectors have a positive-x and a negative-x direction respectively. Inside the slipstream, the tip and root vortices, as well as the bound vorticity, introduce swirl velocities that have the same direction with that of the propeller rotation (counter-clockwise seen from behind). In order to recover the swirl velocity generated by Γ_1, a horseshoe vortex with the opposite direction to that of Γ_1 (with strength of Γ_2) is introduced, such that the induced swirl velocity by Γ_2 would have the opposite direction with those induced by Γ_1. In this way, Γ_2 generates a swirling flow opposite to the sense of propeller rotation, leaving less rotational kinetic energy in the slipstream.

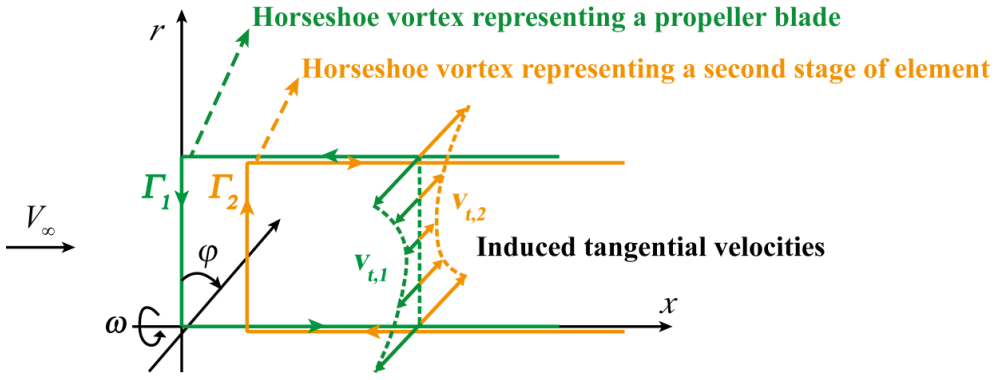

Figure 3.2 Demonstration of swirl-recovery mechanism for propeller propulsions. In this case, both the propeller blade and the second stage of element are simplified into a horseshoe vortex.

As discussed in Sec. 1.2, in terms of axial position, the second load-carrying element Γ_2 can be either ahead or behind Γ_1, and in terms of motion, Γ_2 can be either rotational or stationary. On the condition that the element that generates Γ_2 is also rotating (in the opposite direction with Γ_1), it represents the case of CRP. When the element that generates

Γ_2 is stationary and located in front/behind of the propeller stage, it corresponds to PSVs/upstream wing and SRVs/downstream wing respectively.

It should be noted that the SRV is propulsive beneficial due to its capability of providing extra thrust without consuming any extra power. Swirl recovery is just the mechanism of the thrust enhancement from the SRV. Thus, during the optimization of the SRV, the objective function is set as the maximum thrust provided by the SRV instead of the maximum swirl recovered by the SRV as discussed in the next section.

3.3 Design of the SRVs

3.3.1 SRV design procedure

The SRV design procedure is simplified into three steps as shown in Figure 3.3. At the beginning of the procedure, the inflow conditions to the SRVs need to be determined. This can be done either experimentally by a wind-tunnel test, or numerically from a simulation of the isolated propeller as done in this work. In the second step, the optimal loading distribution on the SRVs is determined. The third step then constitutes an airfoil design routine to achieve the optimal loading distribution.

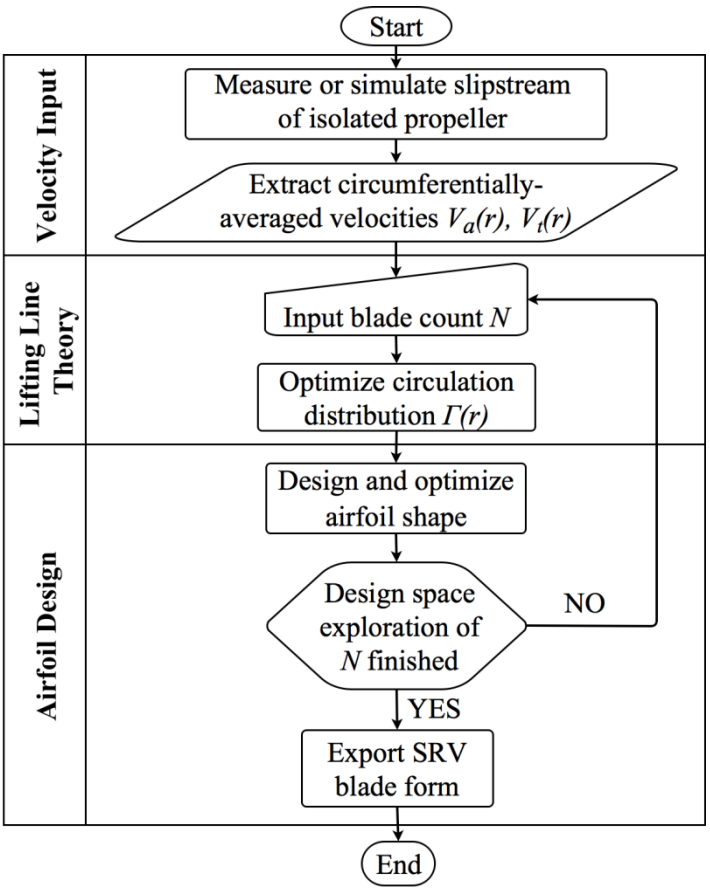

Figure 3.3 Framework of the SRV design procedure.

Prior to the design of the SRVs, a description is required of the flowfield at the position of the SRVs. This is achieved by performing a numerical simulation of a given isolated propeller based on the RANS equations. The propeller used in this research represents a

scaled-model of a conventional propeller of a typical regional turboprop aircraft. It features six blades and a diameter of 0.406 m. The hub of the propeller has a diameter of 0.084 m, and the blade pitch angle equals 30° at 70% of the radius. The sectional twist angle (relative to the 0.7*R* section) and chord length distributions are presented in Figure 3.4. The layout of the propeller is shown in Figure 3.5.

3.3.1.1 SRV design input from numerical simulation of the isolated propeller

Since the propulsive performance of SRVs is directly related to the velocity distributions in the slipstream (or equivalently the performance coefficients of the propeller) regardless of the detailed blade geometry, the propeller model used in this research is considered to be generic.

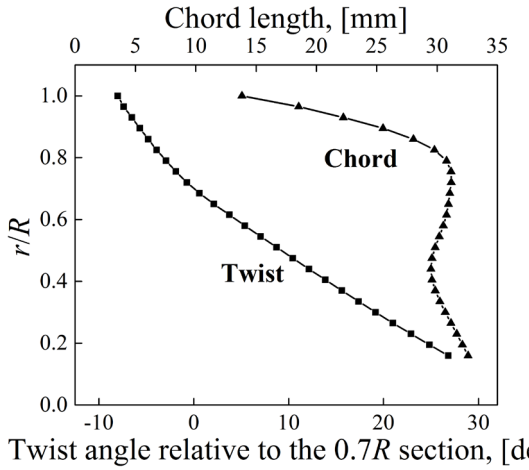

Figure 3.4 Sectional twist (relative to the 0.7*R* section) and chord length distributions of the 6-bladed propeller used in this research.

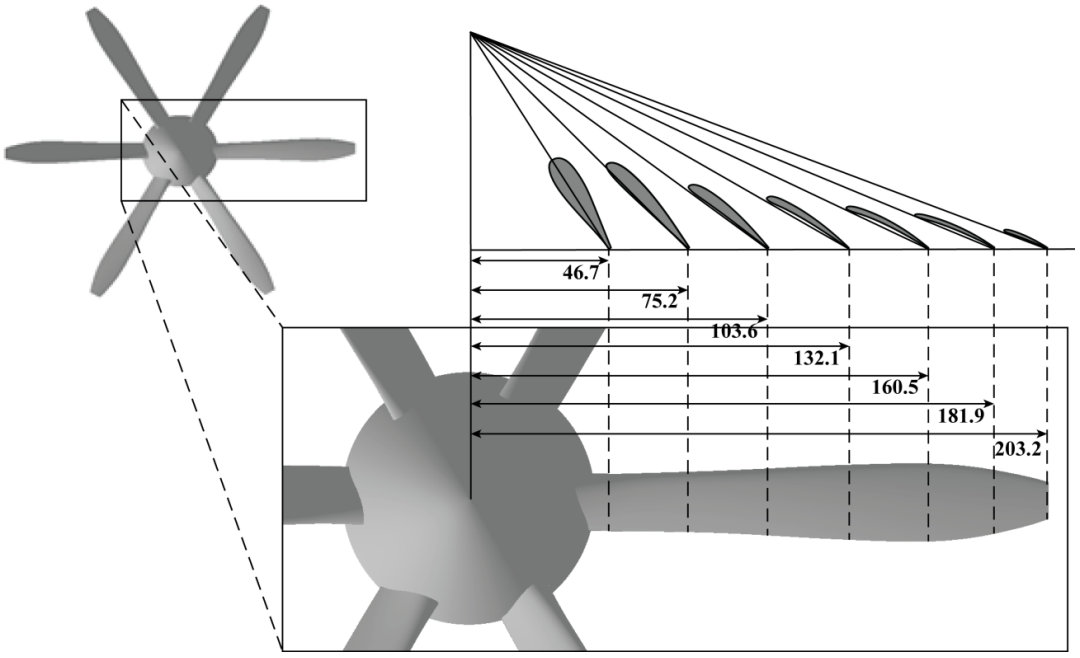

Figure 3.5 Layout of the 6-bladed propeller used in this research. It represents a typical propeller that is used in modern turboprop designs. Dimensions in millimeters.

The computational domain for the propeller calculation consists of a cylinder extending about 10 times the propeller radius in all three (upstream, downstream and radial) directions from the propeller-disk plane. This domain is larger than that was used in Ref. [69], which was already shown to be able to guarantee that the flowfield around the propeller blades was not perturbed by the boundary conditions. The mesh is generated by combining two separate blocks as shown in Figure 3.6. For the cylindrical block surrounding the propeller (region I in Figure 3.6a), a structured mesh is generated using NUMECA® Autogrid. Because of the symmetry of the propeller, only one blade sector of 60° needed to be meshed. The boundary layers on the blade and hub are resolved using 25 layers of hexahedron elements. For the second mesh block, an unstructured mesh is generated in ANSYS® ICEM. In order to ensure an adequate resolution of the propeller slipstream at the position of the SRVs, smaller tetrahedral elements are arranged in a cylindrical area downstream of the propeller block (region II-1 in Figure 3.6a).

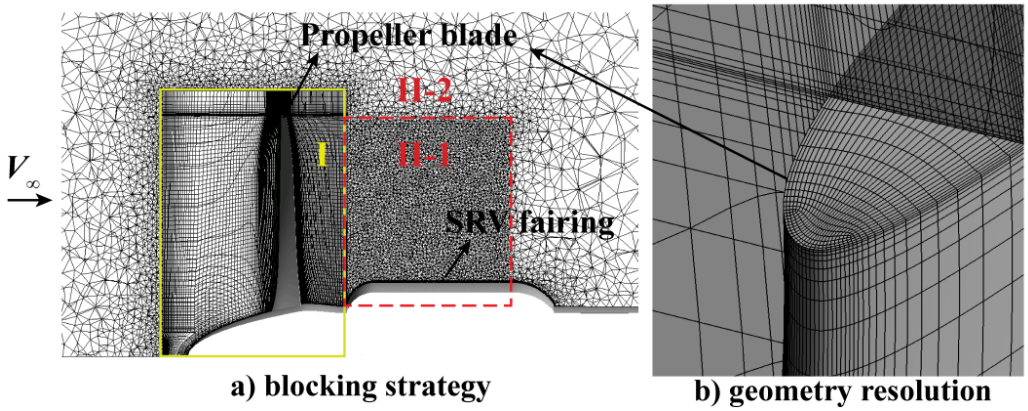

Figure 3.6 Hybrid computation mesh for the isolated propeller.

The inlet of the domain is modeled as a velocity inlet, with a turbulence intensity of 5%. Combined with a relatively high eddy viscosity ratio (the ratio between the turbulent viscosity and the molecular dynamic viscosity equals 10), this results in a turbulence level at the propeller plane equal to the level of 0.5% characteristic [70] of the wind tunnel used for the validation experiment (discussed in Sec. 3.4). At the outlet of the domain, the average static pressure is prescribed to be equal to the undisturbed static pressure. The SRV fairing (later shown in Figure 3.17), which was required to house the instrumentation of the SRVs in the validation experiment, is modeled with a no-slip wall boundary condition. In contrast, the nacelle behind the SRV fairing, which extends further downstream to the outlet, is modelled as a free-slip wall to reduce the number of grid points. The utilization of free-slip wall condition is considered to be acceptable since this part of nacelle is behind the field of interest where the SRVs are located. On the sides of the domain, periodic boundary conditions are specified. The conservation equations are solved based on a rotating reference frame. The alternate rotation model is utilized for the advection term in the momentum equation. With the alternate rotation model, instead of advecting the relative frame velocity, the flow solver advects the absolute frame velocity [71].

The Shear Stress Transport turbulence model, which gives good prediction of adverse pressure gradient flows (e.g. in the propeller studies of Refs. [72] and [73]), is used. The

automatic wall treatment, which automatically switches from wall-functions to a low-*Re* near wall formulation as the mesh is refined [71], is adopted. The simulation is performed at a freestream velocity of 29 m/s, which is equal to the maximum value attainable in the wind tunnel used for the validation experiment (see Sec. 3.4). The corresponding Reynolds number based on freestream velocity and the blade chord length at radial position of 0.7*R* is 5.90×10^4. It should be noted that the flow is assumed to be fully turbulent in the RANS-based simulation, which may result in slightly different velocity distributions of the slipstream compared to the laminar-turbulent boundary layer that is likely to be found on the propeller blades. A high loading condition of the propeller, which corresponds to a typical take-off setting, was chosen as the design point to compensate for the low freestream dynamic pressure, thus obtaining a measurable thrust on each vane. The selected operating point corresponds to a computed propeller thrust coefficient of $C_{T,P} = 0.322$.

A grid refinement study was carried out on three meshes: coarse ($y^+ = 4$, $Z = 1.05$ million), medium ($y^+ = 2$, $Z = 1.68$ million) and fine ($y^+ = 1$, $Z = 2.63$ million). The propeller thrust coefficient is plotted in Figure 3.7 with respect to the mesh size factor ($Z^{-2/3}$). As the mesh size reduces, the propeller thrust coefficient approaches an asymptotic value of $C_{T,P} = 0.3233$. This value is obtained by applying Richardson's rule [74] using the predictions of the medium and fine meshes, with a refinement ratio $q = 2$ and order of convergence $b = 2.27$.

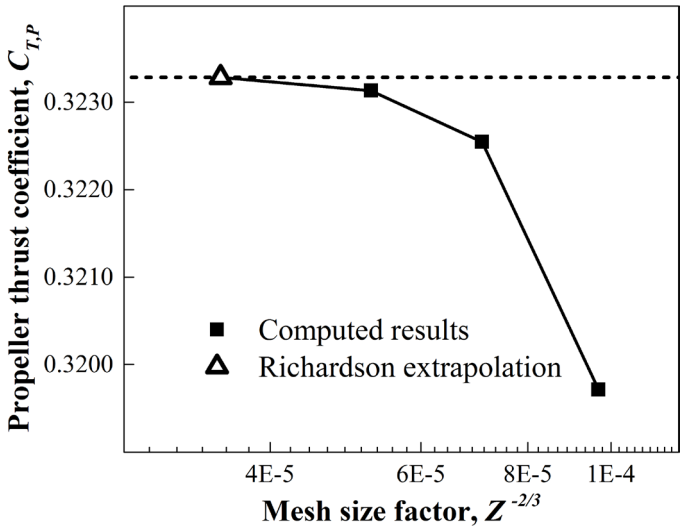

Figure 3.7 Result of the mesh refinement study showing the propeller thrust coefficient as function of the mesh size factor $Z^{-2/3}$.

In order to verify asymptotic convergence of the tested meshes, the grid convergence index (GCI) is determined for both the medium and fine meshes. A percentage of $GCI_{fine,medium} = 0.14\%$ is achieved with the fine mesh and $GCI_{medium,coarse} = 0.69\%$ with the medium mesh. When comparing these two values by:

$$\frac{GCI_{fine,medium}}{GCI_{medium,coarse}} \cdot q^b = 1.0018 \tag{3.1}$$

the ratio is approximately one which indicates that the solutions are well within the asymptotic range of convergence.

The radial distributions of the circumferentially-averaged axial velocity V_a, and tangential velocity V_t, are critical input information for the SRV design. The results obtained using the three meshes are compared in Figure 3.8. A survey plane was located at the SRV mid-chord position at 0.61R downstream of the propeller.

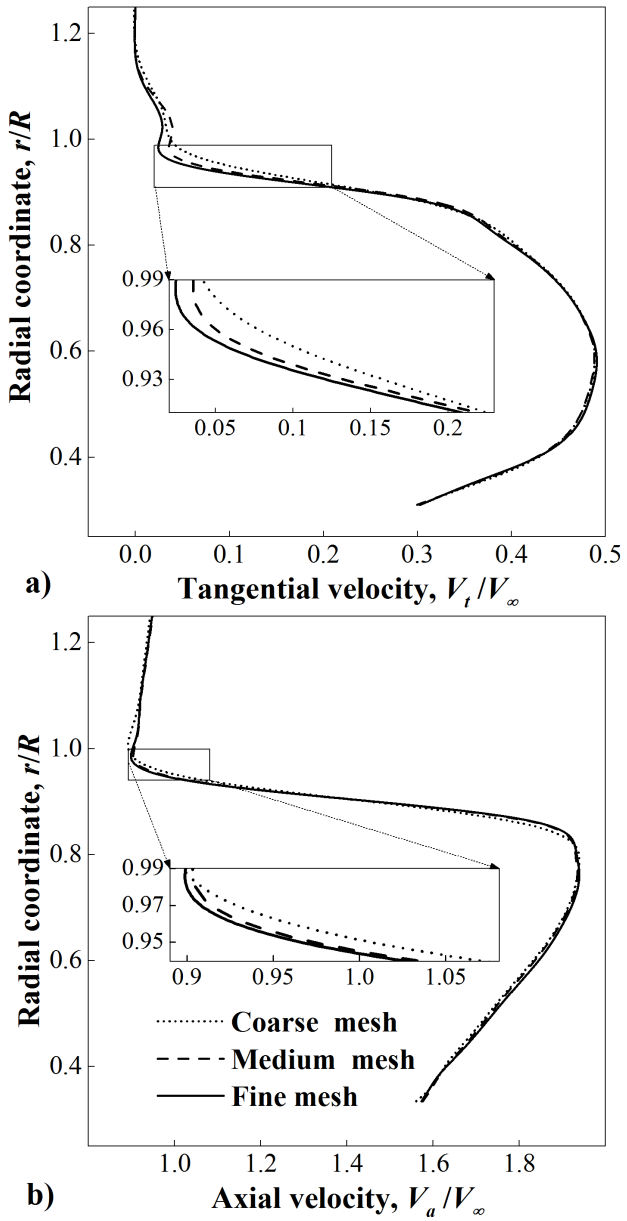

Figure 3.8 Comparison of computed circumferentially-averaged tangential and axial velocity distributions from different meshes at $J = 0.6$, $C_{T,P} = 0.322$ and $\beta_{0.7R} = 30°$.

A maximum difference of 0.36 m/s (1.2% of the freestream velocity) is observed for the tangential velocity when comparing the results obtained with the medium and the fine meshes. The difference of the integrated angular momentum on the survey plane between the medium and the fine meshes is, however, less than 0.5%. Since the thrust produced by SRVs is proportional to the amount of the angular momentum in the slipstream, the fine mesh is thus considered to be converged. For the axial velocity, the maximum difference is 0.27 m/s

(0.9% of the freestream velocity), occurring in the blade tip region. The reason why the computed velocities from the coarse mesh differ more from the other two meshes is due to the larger element size in the slipstream. In the simulation with the coarse mesh, the blade tip vortex is more spread out compared to the results obtained with the medium and fine meshes, leading to a faster decay of both the axial and the tangential velocities toward the outer undisturbed flow.

The axial and tangential velocity distributions from the CFD simulation are taken directly as the inflow condition for the SRV design, based on the assumption that the upstream effect of the SRVs on the time-averaged propeller performance is negligible. This is confirmed by both the propeller-loading measurements and the pressure measurement behind the propeller, as discussed later in Sec. 3.4.4.

3.3.1.2 Determination of optimal circulation distribution on the SRVs

The optimal circulation distribution on the SRVs is obtained with a model based on lifting line theory as discussed in Sec. 2.2.2 and also the beginning of this chapter. In the lifting line theory, the N vanes are simplified into N straight lifting lines with equal angular spacing and identical loading. Thus, sweep, lean and skew are not included in the current design method. The contraction of SRV slipstream is neglected due to the fact that the thrust produced by the SRVs is only a few percent of propeller thrust [38,39]. A prescribed-wake model is used, which consists of constant pitch, constant radius helical vortices, the direction of which is aligned with the effective inflow velocity V^* at the vane position including the induced velocities. The velocities and forces (per unit radius) on the vane section are shown in Figure 3.9.

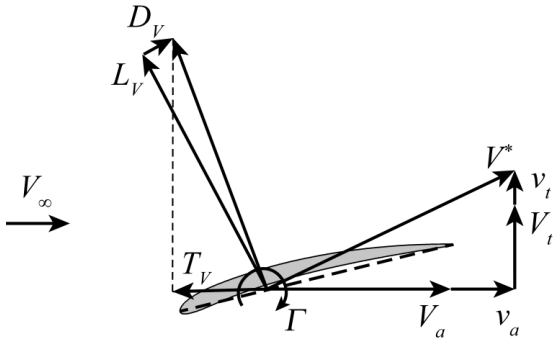

Figure 3.9 Velocity and force diagram of SRV section.

The thrust of the SRVs comes from the axial component of the lift and drag acting on the vanes. The Kutta–Joukowski (K–J) theorem is applied to determine the local lift on each vane section. By applying the K–J theorem, two main assumptions are made: First, the radial component of the slipstream velocity is neglected such that the flow surrounding the vane is two dimensional (2D) on each radial section. Second, each 2D section has a uniformly-distributed inflow of V^*. The thrust generated by the SRVs can then be expressed as:

$$T_V = \rho N \sum_{m=1}^{M} \left((V_{t_m} + v_{t_m}) \Gamma_m - \frac{1}{2} V_m^* C_{d_m} c_m (V_{a_m} + v_{a_m}) \right) \Delta r_m \qquad (3.2)$$

with the subscript *m* indicating each radial segment of the SRV. In order to maximize the thrust, the partial derivative of T_V with respect to the circulation distribution is set to zero:

$$\frac{\partial T_V}{\partial \Gamma_m} = 0 \tag{3.3}$$

where the derivative is given by:

$$\begin{aligned}\frac{\partial T_V}{\partial \Gamma_m} = {} & (V_{t_m} + v_{t_m})\Delta r_m + \sum_i \frac{\partial v_{t_i}}{\partial \Gamma_m}\Gamma_i \Delta r_i \\ & - \sum_i \frac{1}{2}\frac{\partial V_i^*}{\partial \Gamma_m} C_{d_i} c_i (V_{a_i} + v_{a_i})\Delta r_i \\ & - \sum_i \frac{1}{2} V_i^* \frac{\partial (C_{d_i} \cdot c_i)}{\partial \Gamma_m}(V_{a_i} + v_{a_i})\Delta r_i \\ & - \sum_i \frac{1}{2} V_i^* C_{d_i} c_i \frac{\partial v_{a_i}}{\partial \Gamma_m}\Delta r_i\end{aligned} \tag{3.4}$$

The partial derivatives of the induced tangential and axial velocities with respect to the circulation of the horseshoe vortex, called "induction factors", are computed based on the analytical equations derived by Wrench [75] for constant-pitch helical horseshoe vortices. Moreover, it was verified that both the magnitude and the form of the C_d and *c* distributions have a negligible effect on the circulation distribution obtained by solving Eq. (3.3), as also found by Epps [76]. Therefore, the three terms on the right hand side of Eq. (3.4) containing $(C_d \cdot c)$ can be neglected and the vane optimization with respect to the drag component is performed in a separate subsequent step. In this way, a non-linear system of equations is formed which can be solved by Newton's method. In the optimization of the vane geometry, no feedback of the SRVs to the propeller is taken into account. Hence, in this formulation, $\{\Gamma, v_a, v_t\}$ are taken as the vector of unknowns updated and solved by the Newton solver [76].

3.3.1.3 Airfoil design of SRV sections

Having determined the optimal circulation distribution using the lifting line approach described above, the airfoil shape is designed and optimized to minimize the drag of the SRVs while maintaining the desired circulation distribution. On each vane section, with the constraint of the circulation magnitude, the drag term $(C_d \cdot c)$ is set as the objective function to be minimized. Airfoil profiles may be considered as made up of thickness profile forms disposed about a mean line. As discussed in Ref. [77], the airfoil thickness is of particular importance from a structural standpoint. The mean line form is also important since it determines some of the most important aerodynamic properties of the airfoil section, e.g., the angle of zero lift, the pitching moment characteristics, and the stall behavior. To guarantee an airfoil design that complies with acceptable aerodynamics performance and structural characteristics, the airfoil geometry was parameterized using five variables as in the NACA 4-digit airfoils: the maximum thickness *t*, chordwise position of maximum thickness t_p,

maximum camber *h*, chordwise position of maximum camber h_p, and chord length *c*.

It is an intrinsic characteristic of a propeller that the slipstream exhibits a strong but periodic unsteadiness, resulting from the passages of the blade wakes and tip vortices. For example, the dynamic pressure profiles in front and behind the propeller at 50% radial position were plotted in Fig.7 of Ref. [40]. A sinusoidal variation was observed upstream of the propeller due to the potential effect of the blade, with the period length coherently dependent on the number of blades. Downstream of the propeller, the potential effect is also present. Besides the potential effect, the viscous forces exerted on the blades lead to the generation of the boundary layer. Once the boundary layer is shed into the slipstream, a wake region was identified from the dynamic pressure profiles which was characterised by a deficit in axial velocity and a peak in tangential velocity as shown in Figure 3.10.

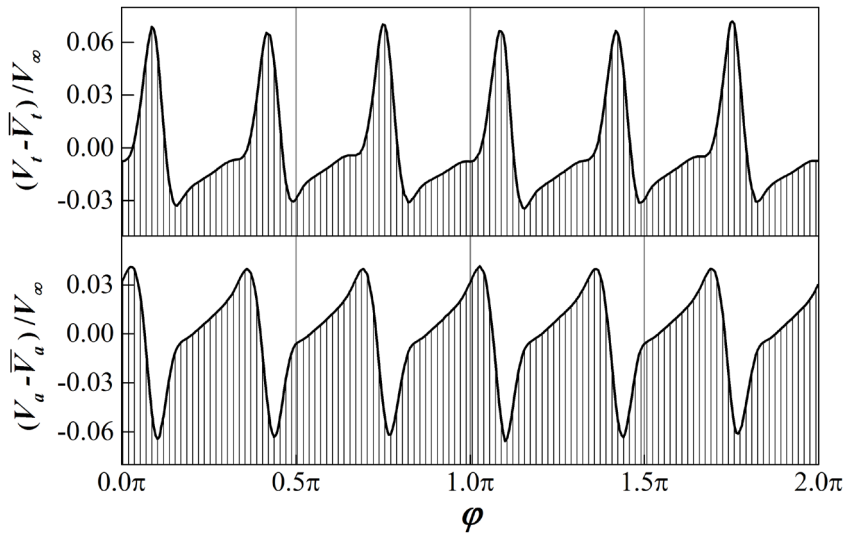

Figure 3.10 Tangential (upper) and axial (lower) velocity distributions at 0.5*R* behind the propeller on the $r = 0.5R$ circle obtained from the RANS simulation of the isolated propeller of Figure 3.5 at $J = 0.6$, $C_{T,P} = 0.322$ and $\beta_{0.7R} = 30°$.

When the SRV encounters the propeller blade wake, the deficit in axial velocity as well as the peak in tangential velocity leads to a sudden increase in angle of attack of the vane section [38,39]. This leads to strong periodic variations in angle of attack, making it important to have a large stall margin for the SRV airfoils. A robust optimization is used and two operating conditions are chosen: the design point at which the design lift coefficient is achieved and the stall angle of the profile (i.e. the angle of attack at maximum lift coefficient). Given a weight factor w_1 for the drag term at stall and another weight factor w_2 for the stall margin; the objective function *F* for the airfoil design is defined as:

$$F(t,t_p,h,h_p,c) = \frac{[(C_d \cdot c)_{des.}]_{opt.}}{[(C_d \cdot c)_{des.}]_{ini.}} + w_1 \frac{[(C_d \cdot c)_{stall}]_{opt.}}{[(C_d \cdot c)_{stall}]_{ini.}} - w_2 \frac{[(\alpha_{stall} - \alpha_{des.})]_{opt.}}{[(\alpha_{stall} - \alpha_{des.})]_{ini.}} \quad (3.5)$$

where the subscript *ini.* denotes the initial status and *opt.* the optimized results. The weight factor w_1 and w_2 can be chosen based on the magnitude of the inflow angle variation of individual SRV sections, of which both were set to 0.5. A minimum relative thickness *t* of 2% was taken as lowest limit for manufacturing. Initial cases were randomly sampled in the

design space at the beginning of the optimization loop. A pattern search algorithm, which is a robust and gradient-free optimization algorithm [78], was utilized. The airfoil performance was determined with XFOIL [79]. The corresponding Reynolds number was calculated based on the local flow parameters, where the velocity term included both the slipstream inflow velocities and the induced velocities.

3.3.2 Parametric study of key SRV design parameters

The impact of the blade count and radius on the thrust production by the SRVs is studied by performing parametric studies in which both variables are varied systematically. For each variation, an optimized design is generated using the approach defined in Sec. 3.3.1.

3.3.2.1 Optimal SRV blade count

As discussed in Sec. 3.3.1, the thrust produced by the SRVs is the result of the axial component of the lift and drag acting on them. It can be expected that by increasing the number of vanes, more residual swirl in the propeller slipstream can be recovered due to the increased solidity. The theoretical maximum in terms of thrust production can be found when the blade count goes to infinity. However, at the same time the viscous drag of the SRVs also increases. Therefore, the optimal performance is obtained as a compromise between maximum swirl recovery and minimum viscous drag on the SRVs. This tradeoff is investigated by computing the SRV performance as a function of the number of vanes, both with and without including the viscous drag in the computations. The propeller geometry and operating conditions are the same as introduced before, and the corresponding results are shown in Figure 3.11a.

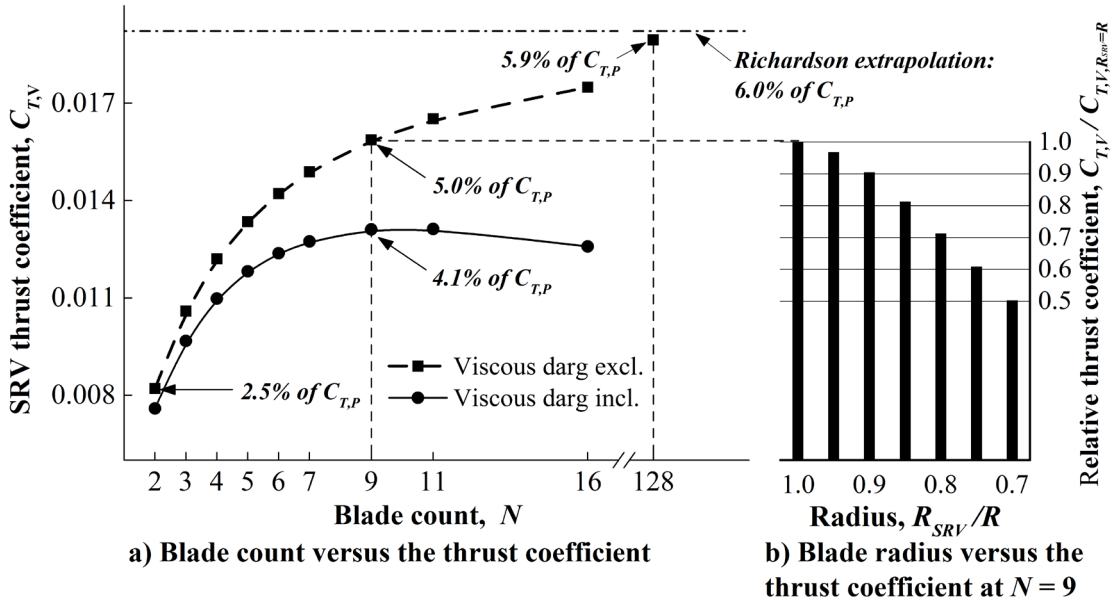

Figure 3.11 Parametric study of SRV design in terms of blade count and radius at $J = 0.6$, $C_{T,P} = 0.322$ and $\beta_{0.7R} = 30°$.

In the case where the viscous drag is neglected, the thrust increases asymptotically with the blade count, from 2.5% of the propeller thrust with 2 vanes up to 5.9% with 128 vanes.

The asymptotic value of the SRV thrust coefficient was estimated by Richardson extrapolation using the computed results for N = 2, 16, and 128. With the refinement ratio q = 8 and the order of convergence b = 0.892, the asymptote of the thrust coefficient of the SRV $C_{T,V}$ was estimated to be 6.0% of the propeller thrust. However, the viscous drag of the SRVs increases approximately linearly with the blade count. Therefore, the optimum number of vanes is obtained when the increment in thrust by addition of an extra vane is compensated by its own drag. As also shown in Figure 3.11a, when taking into account the effects of viscous drag, the optimal number of SRVs occurs at N = 9, for which the predicted SRV thrust is 4.1% of the propeller thrust. The SRV designed at the optimum blade count (N = 9) is illustrated in Figure 3.12, together with the six-bladed propeller.

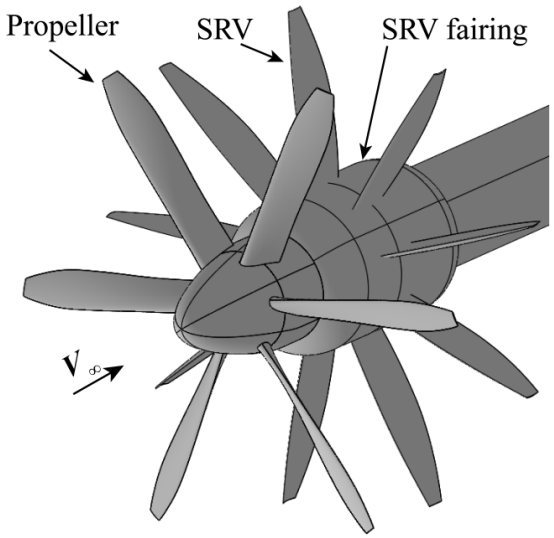

Figure 3.12 Illustration of the six-bladed propeller and SRV designed at blade count N = 9 and radius the same with that of the propeller.

However, despite the identification of this optimum blade count, for the validation experiment (see Sec. 3.4), only 4 SRVs were used because of the limited space available in the SRV fairing for the instrumentation of the individual SRVs. It should be noted that the weight penalty resulting from the addition of SRVs is not considered, which should be included when performing the aircraft design equipped with propeller and SRVs.

3.3.2.2 Effect of SRV cropping

The SRV performance discussed above was obtained under the hypothesis that the radius of the SRVs is the same as that of the propeller. However, as seen in earlier research on CRPs [27], when the second blade row has the same radius as that of the first row, the tip vortices from the first rotor periodically impinge on the leading edge of the second rotor (e.g. Figure 11 of [80]). The resulting unsteady loading leads to an elevated noise level [81] as well as structural vibrations [82]. Therefore, the characterization of the SRV performance as a function of the vane radius is important during the definition of the optimal SRV design, since with decreasing vane radius, less swirl can be recovered by the SRVs. The effect of the SRV radius on the thrust was studied by systematically varying the SRV radius for a fixed blade count of 9 without including the viscous drag. The results are depicted in Figure 3.11b. When the radius is reduced to 0.95R, 97% of the thrust generated by the uncropped SRVs

($R_{SRV} = R$) is obtained. From this point onward, the thrust coefficient of the SRVs decreases with reduction of the radius, down to 50% of the thrust of uncropped SRVs for the case of an SRV radius of 0.7 times the propeller radius. For the validation experiment (see Sec. 3.4), the SRV radius was kept equal to the propeller radius to maximize the thrust contribution of the SRVs, accepting the potential associated noise penalty.

3.3.3 Design of SRVs for the validation experiment

The design method outlined in Sec. 3.3.1 was applied to define the shape of the SRVs used for the validation experiment. Due to the constraint of limited space for installation and instrumentation of the vanes in experiments as mentioned in Sec. 3.3.2.1, a blade count of 4 was selected, with an SRV radius equal to the radius of the propeller. The vanes are discretized into 20 lifting segments. The resulting optimal circulation distribution is shown in Figure 3.13a, together with the distribution of the sectional pitch angle.

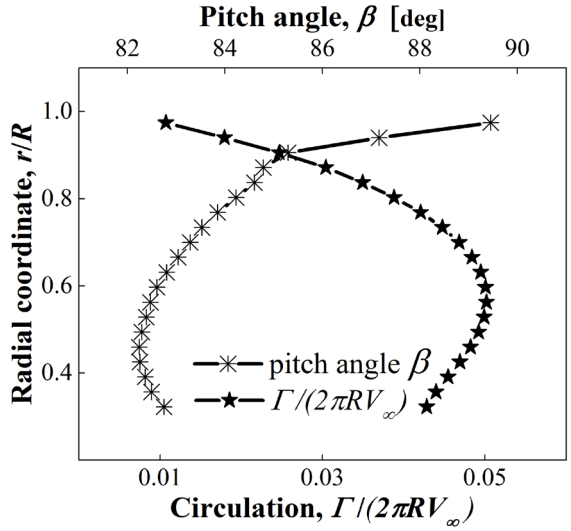

a) Radial distributions of pitch angle and circulation

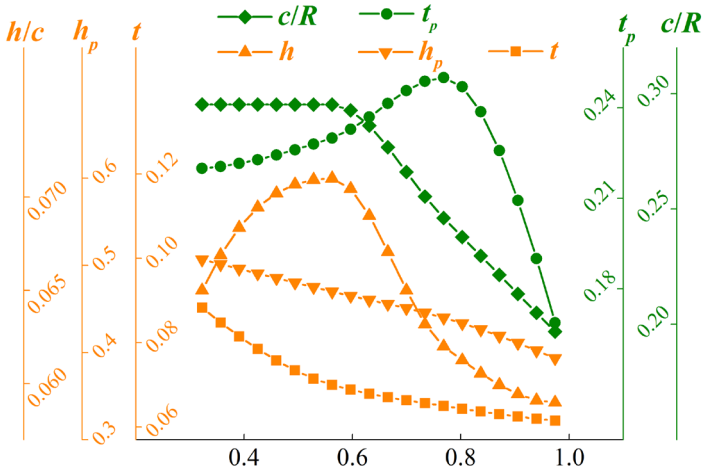

b) Blade form curves

Figure 3.13 Blade form curves of SRVs designed with blade count $N = 4$ and radius the same with that of the propeller at $J = 0.6$, $C_{T,P} = 0.322$ and $\beta_{0.7R} = 30°$.

Following the steps shown in Figure 3.3, after having determined the optimal circulation distribution from the lifting-line method, the airfoil sections need to be designed to achieve minimum drag on the vanes. In the wind-tunnel test, the typical Reynolds number on the vane sections (based on the freestream velocity and the chord length of the vanes) was on the order of 10^5, at which serious deterioration of the lift and drag may occur due to the laminar separation bubbles [83,84]. On the other hand, the inflow of the SRVs is highly turbulent because of the presence of the propeller upstream of it. In a tractor-propeller configuration, the boundary layer on the part of the wing immersed in the propeller slipstream alternates between laminar and turbulent states, due to the periodic perturbation caused by the passages of the viscous wakes of the propeller blades [85,86]. The SRVs would experience a similar cyclic state change in the boundary layer, promoting transition on the vanes. Before the test, it was not known which of these two effects would dominate. Therefore, it was decided to use forced transition in the airfoil design process, assuming an instantaneous transition to turbulence without accounting for transition device drag. During the airfoil optimization, an optimum chordwise transition position of $x/c = 0.6$ was found to result in the most efficient suppression of the laminar separation bubble and thus minimum drag on the vane section at mid-radius. Therefore, this setting was implemented for all vane sections. The implications of this choice will be further discussed in Sec. 3.4.3.

Following the design procedure described in Sec. 3.3.1, the vane planform is obtained by airfoil optimization performed in two steps. First, individual optimizations are performed to minimize drag at four representative sections: the root section ($r/R = 0.32$), the section at maximum circulation ($r/R = 0.56$), the tip section ($r/R = 1.00$), and the section between the point of maximum circulation and the tip ($r/R = 0.78$). The resulting optimized airfoil shapes at these sections are used as starting condition for the overall vane planform optimization, with the objective to minimize the total drag of the vane (thus also including the drag at the intermediate stations). The design parameters of the airfoils at the intermediate sections are obtained by interpolation with a piecewise cubic Hermite polynomial. The local angle of attack on each vane section is also determined during the airfoil design process. By adding the local angle of attack to the inflow angle obtained from the lifting-line analysis, the pitch angle was determined and the twist distribution is obtained.

The final geometry characteristics of the airfoils are depicted in Figure 3.13b. The airfoils feature a forward maximum thickness position and a backward maximum camber position, which creates a negative pressure plateau on the front part on the suction side as shown in Figure 3.14. This front-loaded type of distribution tends to enhance the thrust production from the vanes since only the axial component of aerodynamic forces contributes to the SRV performance.

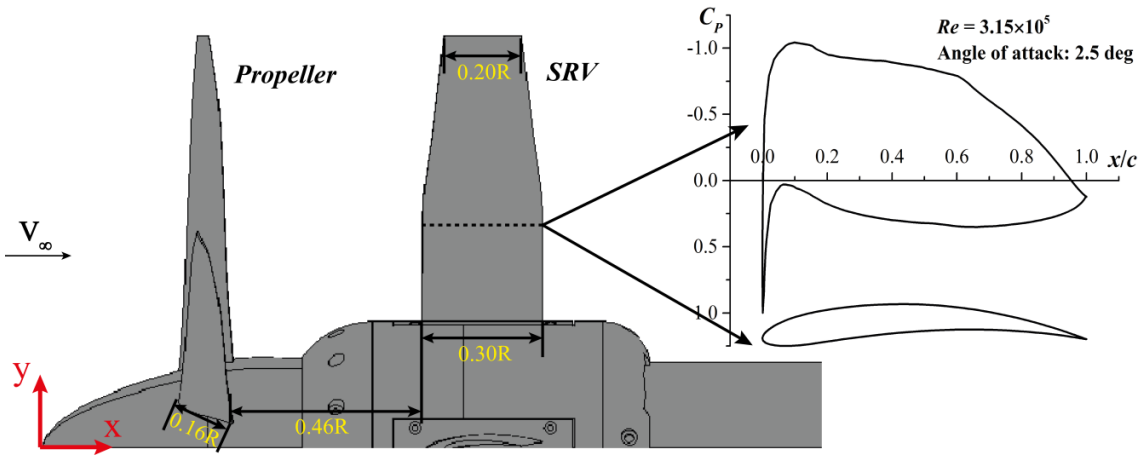

Figure 3.14 Sketch of the propeller, the designed SRVs and the coordinate system (dimensions in millimeters).

3.4 Experimental validation

3.4.1 Experimental setup

Experiments were conducted with the designed SRVs and the propeller model described in Sec. 3.3.3 in the Open Jet Facility at Delft University of Technology. The octagonal test section of the tunnel has a width and height of 2.85 m (15.1*R*) and a contraction ratio of 3:1. A honey comb flow rectifier along with five screens ensures a straight flow with relatively low turbulence level of about 0.5%, and a maximum flow speed of 29 m/s. The propeller axis is oriented parallel to the centerline of the wind tunnel so that the whole setup is placed at zero angle of attack. The model placed in front of the open jet is shown in Figure 3.15.

The propeller was driven by a Tech Development Inc. 1999 pneumatic motor, and featured an integrated six-component Rotating Shaft Balance (RSB, see Figure 3.16) to measure the propeller forces and moments during operation. A detailed description of the RSB is provided in Ref. [87]. The RSB data were acquired at a sampling rate of 10 kHz, and subsequently phase-averaged based on a simultaneously recorded one-per-revolution trigger signal. In this paper, only the time-averaged out-of-plane components of the propeller loading (thrust and torque) are discussed. The RSB measurements were taken for the configurations with and without the SRVs installed to assess the upstream effect of the SRVs on the propeller loading. The uncertainty of the RSB data was reduced by performing advance ratio sweeps five times for each configuration, after which curve fits were generated to model the thrust and torque response of the propeller as a function of the advance ratio.

For comparison purposes, the thrust level of the propeller was also determined using a Pitot-static pressure probe that was positioned at 0.10*R* behind the propeller at a radial position of 0.75*R*. The probe had an outer diameter of 2.5 mm and inner diameter of 1.3 mm. Analysis of the results obtained from the RANS simulation indicates that the maximum crossflow angle to the probe was less than 20°. As indicated in Ref. [88], at such angles the measurement error remains within 1% of the dynamic pressure. Therefore, no corrections were applied for the misalignment of the Pitot probe with the local velocity direction. The pressure measurements were obtained by a Mensor® differential digital pressure gauge, with

the ambient pressure outside the airstream taken as reference pressure. The sampling frequency was set to 10 Hz in order to obtain a statistically converged dataset by averaging over 15 seconds of measurement time.

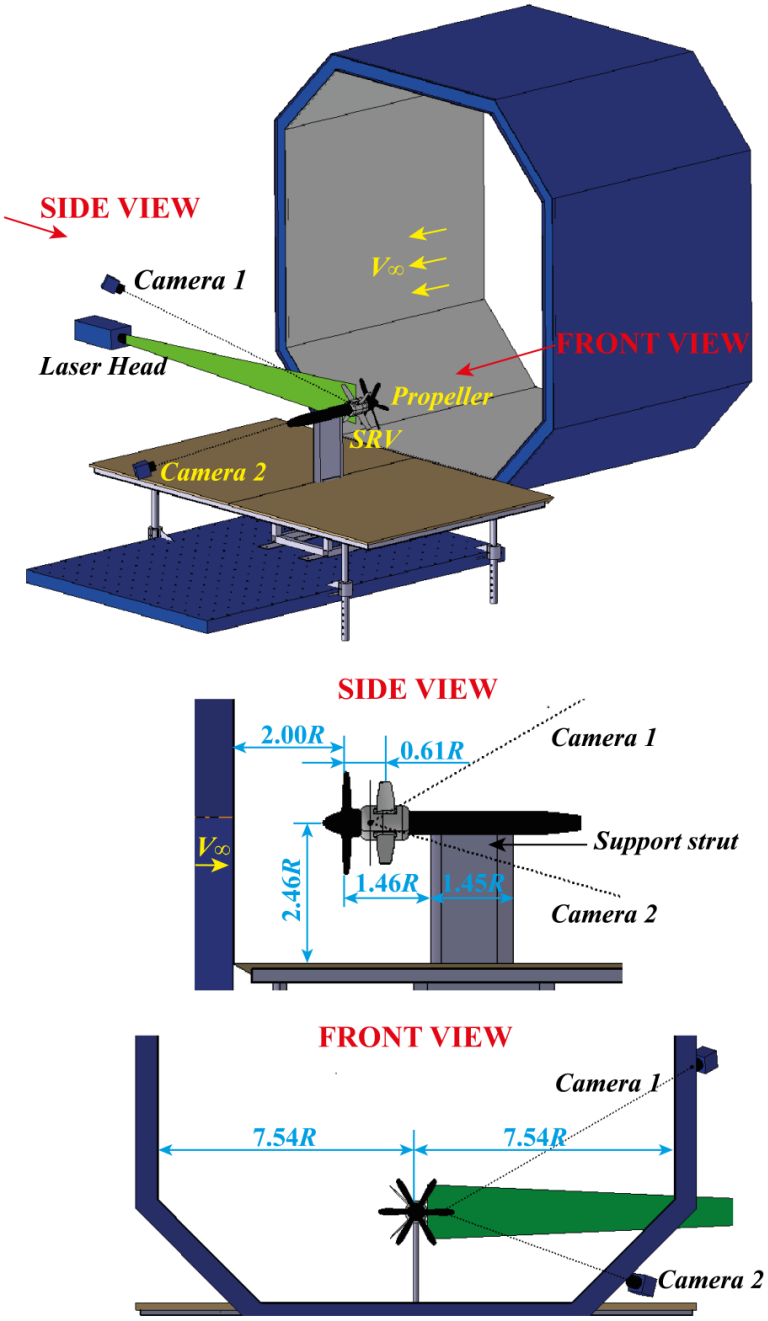

Figure 3.15 Sketch of the experimental setup in the Open Jet Facility of Delft University including a sketch of the PIV measurement setup.

A fairing was required to house the instrumentation and support structure of the SRVs (Figure 3.17). This fairing should be considered as an artifact of the test setup, which would not be present in a full-scale propeller-SRV configuration. The fairing had an outer radius of 63mm (31% of propeller radius) and was mounted directly on the nacelle. A sliding system for each SRV was positioned inside the fairing, providing freedom to axial translation while constraining translation and rotation in the other five directions. The sliding system consisted of a steel track that was fixed to the fairing and two linear sliding units with two sets of linear ball bearings each. Each SRV was mounted on two sliding units; a load cell with maximum

capacity of 20 N was installed on each track in front of the vane measuring the axial thrust per vane. The sampling frequency of the load cell measurements was set at 50 kHz for a total measurement time of 15 seconds corresponding to about 1800 propeller revolutions at a propeller rotation frequency of 120 Hz at $J = 0.6$. It should be noted that the nonzero adhesion force of unknown magnitude of the sliding system always needs to be exceeded whenever the vanes are producing either thrust or drag. In this respect, the load cell readings corresponded to the net SRV thrust minus the adhesion force, thus indicating the lower bound of the thrust that the SRVs produced. Forced transition was achieved on the SRVs by implementing a zig-zag strip on the suction side. The strips had a thickness of 0.2mm and sweep angle of 90°, and were located at $x/c = 0.5$ to guarantee a successful transition at 60% of the vane chord. Measurements were performed both with and without transition strips to verify whether there is a need for forced transition during the airfoil design step.

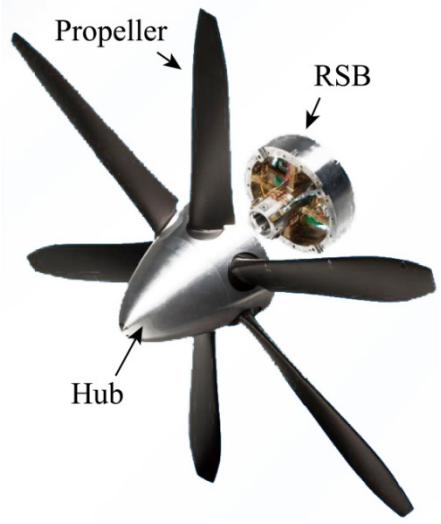

Figure 3.16 Illustration of the six-bladed propeller, the hub, and the RSB. (Adapted from Nahuis [87])

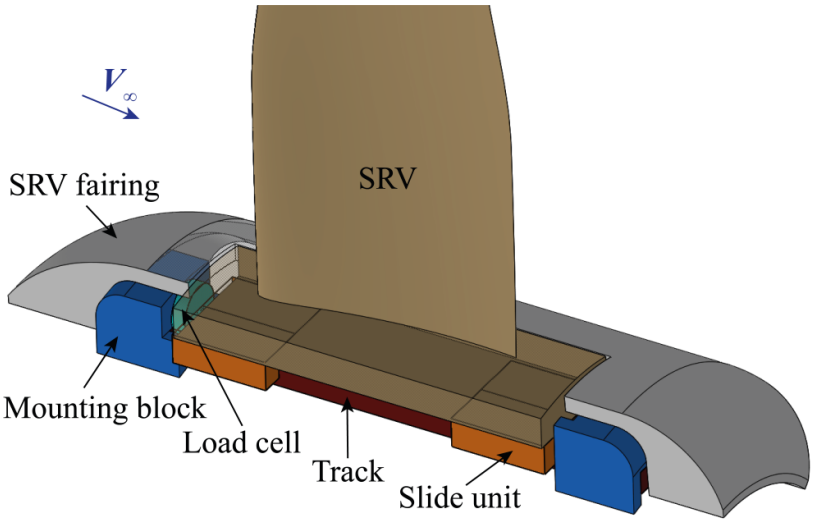

Figure 3.17 Section view of the SRV fairing showing the installation and positioning of the load cell for thrust measurement of the vane.

Measurements of the flowfield surrounding the SRVs were taken using stereoscopic particle-image velocimetry. A Quantel® Evergreen Nd:YAG laser with a maximum pulse energy of 200 mJ was used to illuminate the particles, forming a laser sheet of about 2 mm

thickness. Two LaVision Imager Pro LX cameras were used, with a resolution of 4870 × 3246 pixel and a pixel pitch of 7.4 μm/pixel. A lens with focal length of 200 mm was used for the lower camera, while a larger focal length (300 mm) was adopted for the upper camera to compensate for the longer distance to the measurement plane (Figure 3.15). The field of view spanned around 225 × 150 mm, resulting in a digital resolution of 21.6 pixel/mm. The measurement planes were located at 0.4 c_r upstream and downstream of the SRVs. A SAFEX® Twin Fog Double Power smoke generator was used to produce seeding particles with an average diameter of 1 μm. For each test case, a total number of 1000 statistically independent image pairs were acquired and the resulting vector fields were averaged such that the measurements represent the time-averaged flowfield. The final interrogation window size of 48 × 48 pixel with 75% overlap resulted in a spatial resolution of 0.55 mm.

3.4.2 Uncertainty analysis of experimental measurements

The calibration uncertainty of the RSB data for the static out-of-plane components (which corresponds to the propeller thrust and torque) is smaller than 0.25% of full range [87], i.e. 0.875 N and 0.075 N·m respectively. With an assumption of linear uncertainty propagation, the uncertainties of thrust and torque coefficients are calculated to be 0.0019 and 0.00039 at an advance ratio $J = 0.6$. This estimate does not include potential additional calibration errors due to rotational effects and bias errors during the measurements. The Pitot pressure measurement has an uncertainty of 1.5 Pa, corresponding to an uncertainty of the pressure coefficient of 0.0029 at a freestream velocity of 29 m/s.

The rated accuracy of the load cell used to measure the SRV thrust is 0.1% of full range (0.02N), resulting in an uncertainty of thrust coefficient of 4.2×10^{-5} at an advance ratio J of 0.6. As mentioned in Sec. 3.4.1, there are adhesion forces acting on the sliding units of the measurement system. These adhesion forces are proportional to the loading of the vanes. Considering the fact that the gravitational force of the vanes plays a different role for the vanes at different azimuthal positions (supporting or opposing the aerodynamic side force and torque), the adhesion forces on the vanes are different. Thus, the main uncertainty of the load cell measurements comes from the uncertainty of the adhesion forces of the sliding units. The resulting uncertainty can be obtained by calculating the standard deviation of the thrust measured from different vanes, which will be presented when discussing the SRV performance.

The uncertainty quantification of PIV results was performed based on correlation statistics [89]. This method utilizes the differences between two interrogation windows. The calculated displacement field is used to map back the second image onto the first one. By calculating the position of the particle in each interrogation window, the residual disparity in the position of matching particles gives an estimate of the measurement uncertainty. The uncertainty of the instantaneous velocity components is 0.73 m/s for the in-plane components and 0.85 m/s for the out-of-plane component (approximately 3% of the freestream velocity). Since vector fields were averaged from the 1000 samples, the uncertainty of the time-averaged results is reduced after averaging.

3.4.3 Characterization of propulsive performance of the SRVs

The total thrust coefficient of the SRVs obtained from the load cell measurements is depicted as a function of propeller advance ratio in Figure 3.18. It should be mentioned again that the experimental results only represent the *minimum* thrust generated by the SRVs, as discussed in Sec. 3.4.1. The measured SRV thrust increased gradually from 1.5% of the propeller thrust at the low propeller loading condition of $J = 1.0$ up to 2.6% of the propeller thrust at the highest loading condition of $J = 0.55$. At the J value for which the SRV was optimized ($J = 0.6$), an SRV thrust of 2.6% of the propeller thrust was measured in the experiment for the SRVs with free transition, compared to 3.4% predicted by lifting-line theory. With transition strip installed, only 2.4% of the propeller thrust was produced at the design point. This could be the result of the added drag due to the tripping device. The absence of the performance penalty expected for the clean configuration due to laminar separation could be due to the turbulent perturbations upstream of the vanes caused by the periodic passage of the propeller blade wakes, as discussed before in Sec. 3.3.3. No evidence was found in the present experiments of the possible performance penalty through re-laminarization and the formation of a separation bubble on the SRVs, as reported by Renoud in Ref. [86] for a propeller nacelle. The passage of turbulent segments on the vane's suction side may have stabilized the transitional and turbulent boundary layers and eliminated the possible laminar separation. Thus, the addition of the transition strip did not decrease the total drag but only caused extra device drag.

As can be seen from Eq. (3.2), the thrust generated by the SRV is proportional to the angular velocity in the slipstream. Moreover, the angular momentum contained in the slipstream is proportional to the torque exerted on the propeller blades. Thus, it can be expected that the thrust coefficient of the SRV is proportional to the torque coefficient of the propeller. This is confirmed by plotting the torque coefficient of the propeller with respect to the advance ratio in Figure 3.18. The correlation between $C_{T,V}$ and C_Q can be observed.

As shown previously in Figure 3.10, the flowfield in the slipstream exhibits periodic change due to the rotation of the propeller. Thus, the propulsive performance of the SRVs demonstrates fluctuations corresponding to the periodic inflow conditions. As an example, the unsteadiness of $C_{T,V}$ at $J = 0.6$ from one of the vanes without transition strip is shown in Figure 3.19 within one propeller revolution. With the sampling frequency of the load cell at 50 kHz and propeller rotation frequency at 120 Hz, the measurements have a temporal resolution of 0.9°. At each propeller phase angle, results were phase-averaged over the 1800 samples, as shown as the solid line in Figure 3.19. Assuming the load cell reading at each propeller phase angle to have a normal distribution, the confidence interval with 95% confidence level would lie within 1.96 times the standard deviation around the mean value. This is depicted as the gray area in Figure 3.19.

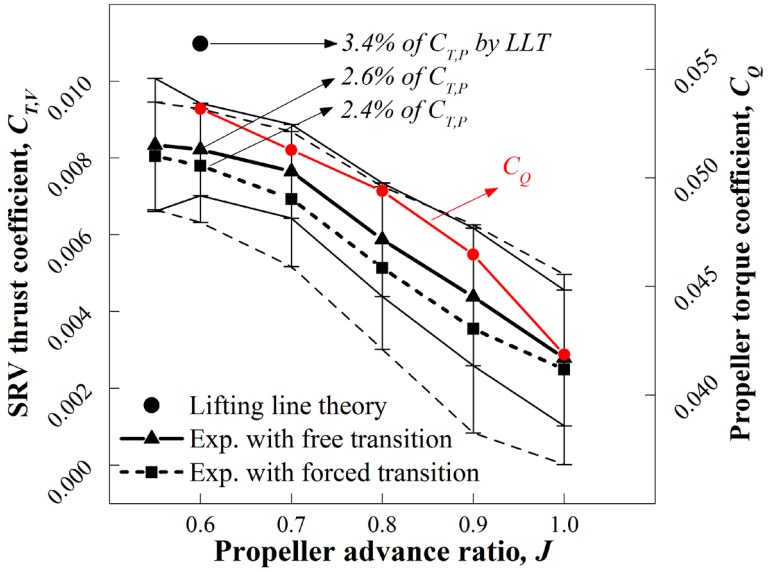

Figure 3.18 Black curves represent time-averaged propulsive performance of the SRVs measured with the load cells. LLT denotes the result computed with lifting-line theory. Red curve illustrates the torque coefficient of the propeller measured with RSB, showing the correlation between the thrust of SRVs and the torque of the propeller.

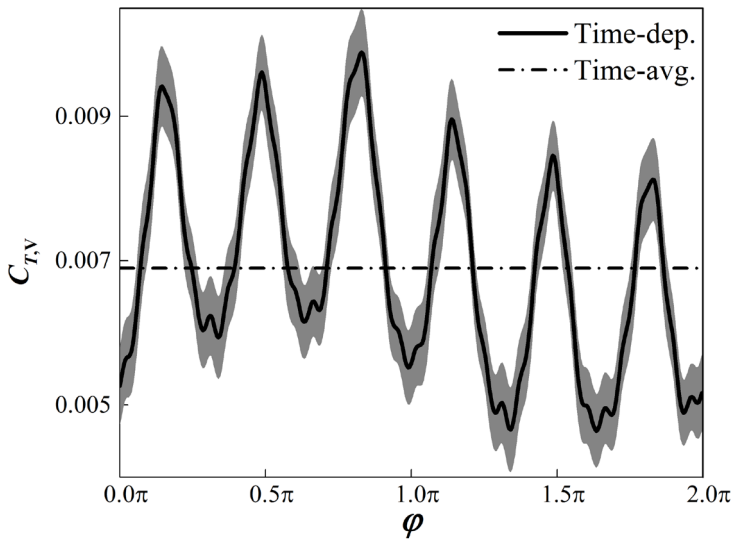

Figure 3.19 Unsteady propulsive performance of one SRV at $J = 0.6$ without transition strip measured using the load cell sketch in Figure 3.17. The 95% confidence level is indicated by the gray area.

Six peaks are observed in the time-dependent thrust coefficient. These are the direct result of the periodic encounter with the wakes and tip vortices of the six propeller blades on the SRVs. When neglecting the viscous drag, it can be known from Eq. (3.2) that the sectional thrust is proportional to the sectional tangential inflow velocity and the sectional circulation as:

$$T_{V_m} = \rho(V_{t_m} + v_{t_m})\Gamma_m \Delta r_m \tag{3.6}$$

Firstly, the peak of the tangential velocity in the wake region leads directly to the increase of the sectional thrust. Secondly, both the peak of the tangential velocity and the deficit of the axial velocity in the wake lead to the increment of the local angle of attack, and further the increment of the sectional circulation. The two reasons together lead to the increment of the sectional thrust when the section encounters with the blade wake. However, unlike the

distinct peak or valley observed in the velocity distribution on a certain radial circle in Figure 3.10, the variation of the vane thrust is more uniformly distributed. This is because the sections at different radial positions encounter with the blade wake at different time instants.

3.4.4 Characterization of propulsive performance of the propeller

The propulsive performance of the propeller was obtained from the RSB measurements, of which the results are shown in Figure 3.20. The propeller characteristics with and without the addition of the downstream SRVs are compared in the top part of the figure. Each symbol represents a data point and the overall trend was estimated by curve fitting with a 4th-order polynomial. In terms of the efficiency, the fitting curve was computed from those of C_T and C_Q following the definition of the propeller efficiency. The adjusted R-squares of all fits were greater than 0.9997, which indicates good fits of the data points. The fitting curves for the SRV on and off case almost coincide, which means that the upstream effect of SRVs is negligible. This confirms the assumption made in the design procedure, as discussed in Sec. 3.3.1.

The propeller performance obtained from the numerical simulation of the propeller at J = 0.6 is also shown in Figure 3.20. The numerical results are observed to have a good agreement with the experimental data. Compared to the thrust coefficient of 0.323 measured by the RSB at the design condition, a $C_{T,P}$ of 0.322 was estimated by the simulation, corresponding to a relative error of 0.3%. Considering the combination of propeller and SRVs as a propulsion system, the performance was compared with that of the isolated propeller as shown in the bottom part of Figure 3.20. The black and blue columns, which represent the cases for the propeller with SRVs off and on respectively, were taken from the fitting curves at each advance ratio. After adding the SRV thrust coefficient $C_{T,V}$ from Figure 3.18 to the measured propeller thrust coefficient, the red column of $C_{T,P} + C_{T,V}$ represents the thrust of the propulsion system. Since the vanes do not require any power input, the torque coefficient of the system was the same as that of the propeller (with SRVs installed), as shown in the mid row of Figure 3.20. The resulting propulsive efficiency was then computed at each advance ratio, as depicted in the last row of Figure 3.20. A prevalent feature of the efficiency plot is that the system efficiency has improved at all advance ratios by installation of the SRVs. At the design condition of J = 0.6, the propulsive efficiency increased from 0.581 to 0.596, while at J = 0.7, the efficiency went up from 0.644 until 0.660, and at J = 1.0, the efficiency improved from 0.767 to 0.779. However, as mentioned in Sec. 3.3.2, these numbers do not account for the weight penalty resulting from the addition of SRVs. An aircraft design study would need to be performed to estimate the performance benefit at airplane level, which was considered out of the scope of the present work.

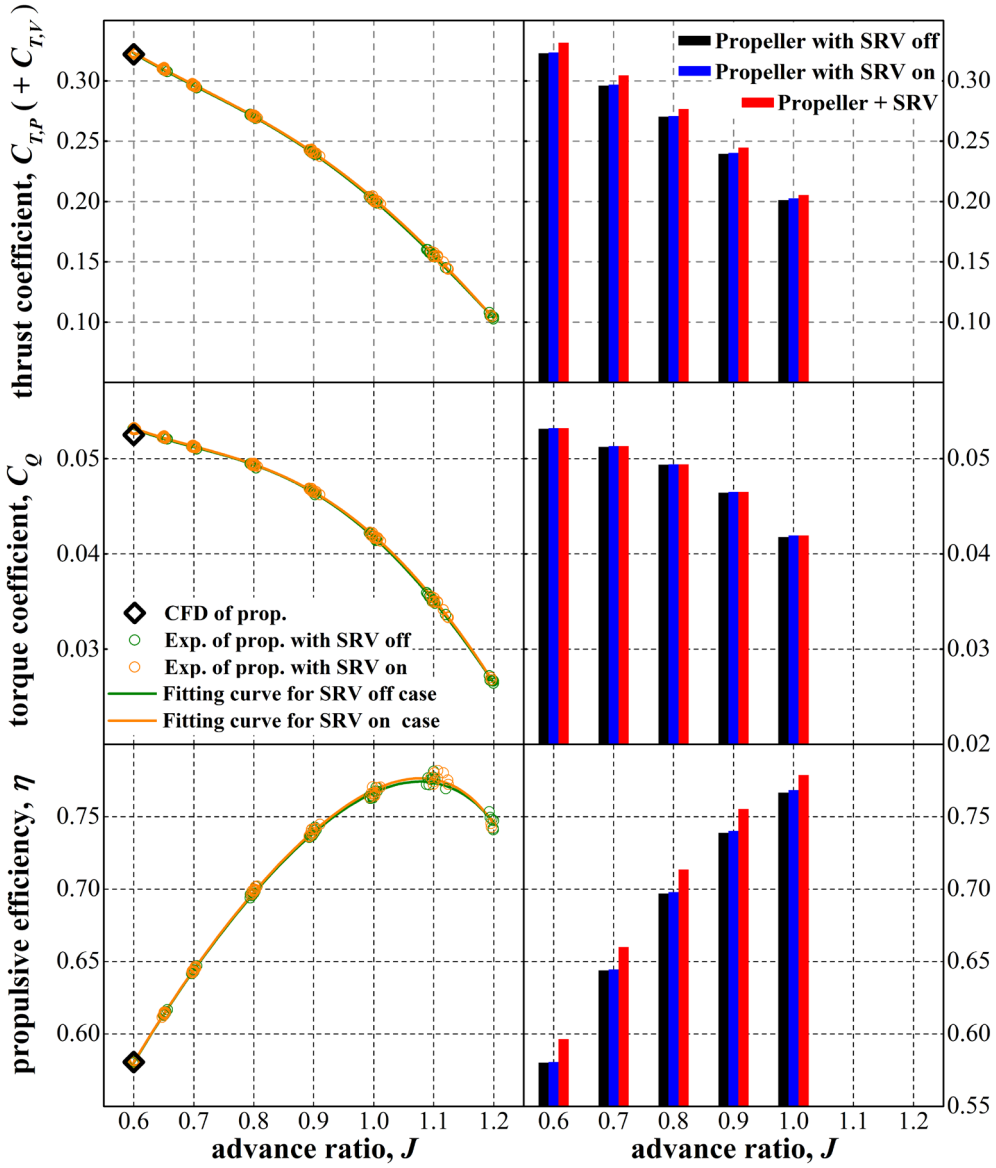

Figure 3.20 Comparison of the propulsive performance of the propulsion system with and without the SRVs installed.

The power exerted by the propeller on the air results in a rise in total temperature, total pressure, and angular momentum in the slipstream. Besides the shaft forces discussed above, the dynamic pressure behind the propeller is also indicative of the propeller loading. Therefore, measurements of the dynamic pressure were taken at 0.24R behind the propeller at an advance ratio of J = 0.6 and a radial coordinate of r/R = 0.75. The resulting pressure coefficient was 4.147 (±0.003 with 95% confidence level) with SRVs installed and 4.157 (±0.001 with 95% confidence level) without SRVs, corresponding to a change of only 0.24%. This once more confirms that the disturbance of the propeller inflow due to the presence of the SRVs is negligible, which can be explained from the relatively large spatial separation between the propeller and the SRVs, and the low loading and solidity of the vanes [41].

3.4.5 Flowfield description by PIV measurements

The input velocities from the RANS simulation of the propeller were validated by PIV measurements on vertical planes positioned at 0.065R upstream and downstream of the location of the SRVs, for the configuration without SRVs installed. Figure 3.21 compares the

circumferentially-averaged axial and tangential velocity profiles as measured during the experiment with the results obtained from the RANS simulation. The axial positions of the measurement planes are indicated by the red dashed lines. In the upstream plane, reasonable agreement is observed between computed and measured data, both in terms of the general shape of the velocity profile and the magnitude of the tangential and axial velocities. The maximum difference between the experimental and numerical results was 1.1 m/s, corresponding to 3.8% of the freestream velocity. This amount of velocity difference would lead to a SRV thrust difference of less than 1.5%. In the downstream plane, this observation also applies for the axial velocity, but in terms of the circumferential velocity a slightly larger difference is visible. This is attributed to the coarser mesh density in this plane, since the downstream plane is outside of the dense grid region arranged around the SRVs (Figure 3.6).

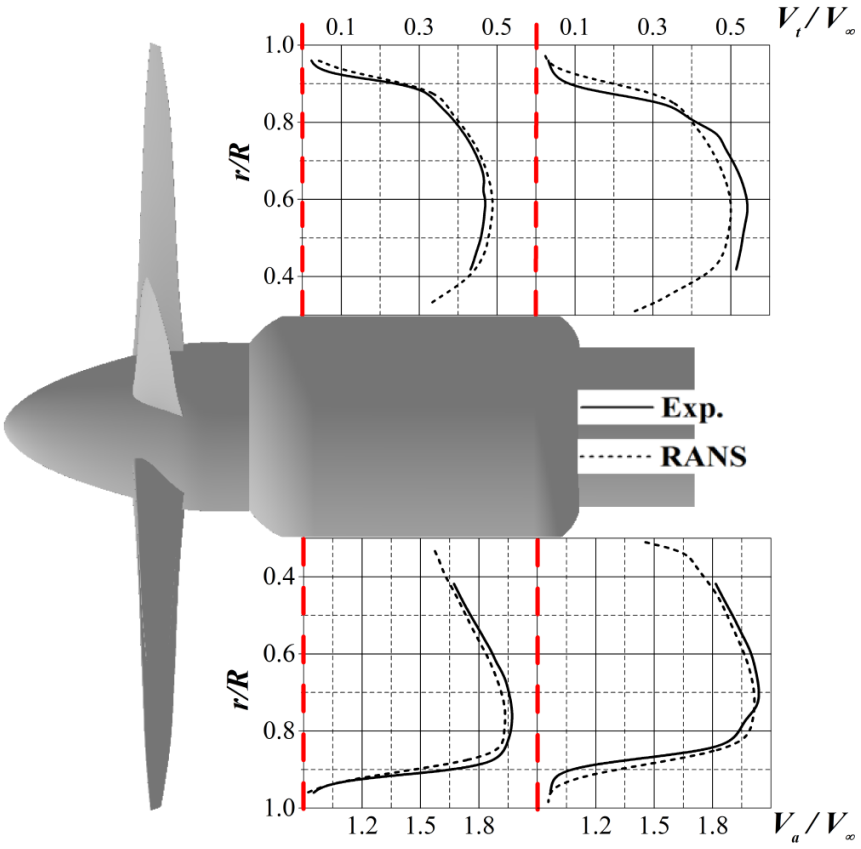

Figure 3.21 Validation of the input velocities from RANS simulation of the propeller by PIV measurements at $J = 0.6$, $C_{T,P} = 0.322$ and $\beta_{0.7R} = 30°$.

The PIV measurements also quantified the swirl recovery achieved by the SRVs, as shown in Figure 3.22. In the plane upstream of the SRVs, no obvious change was observed after installation of the SRVs. At this position, the flowfield can only be affected by the vanes due to potential-flow effects, but the plane was far enough away from the SRVs to make the changes to the flowfield insignificant. From this observation, it can also be expected that the installation of the SRVs has negligible influence on the propeller performance, which is consistent with the measurement data discussed in Sec. 3.4.4. In the plane downstream of the SRVs, the swirl was reduced by installation of the SRVs, with the amount of swirl recovery increasing toward the nacelle. When integrated along the radius, 42% of the angular momentum was recovered by the SRVs.

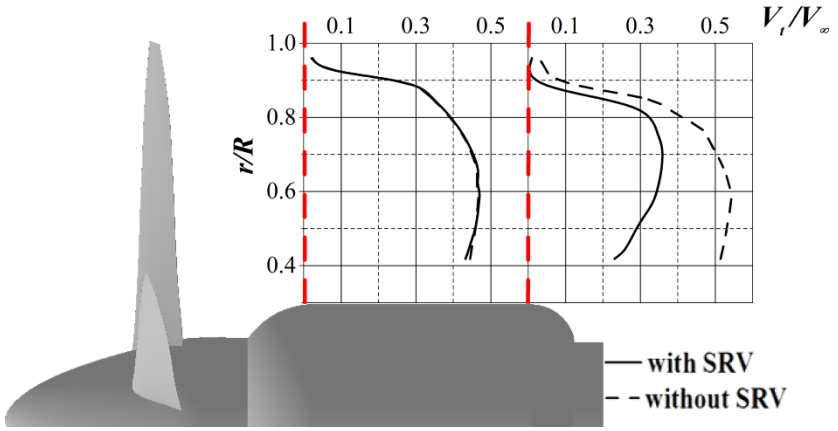

Figure 3.22 Quantification by PIV measurements of swirl recovery by the SRVs at $J = 0.6$, $C_{T,P} = 0.322$ and $\beta_{0.7R} = 30°$.

3.5 Conclusion

A hybrid framework for SRV design is introduced in this chapter which is based on a lifting line model. The design procedure consists of three steps. Firstly, the inflow velocities are prescribed, as obtained from a numerical simulation of the isolated propeller or from an experiment. Secondly, the optimum loading distribution of the SRVs is determined by lifting line theory with the objective of maximum SRV thrust. Thirdly, an airfoil design routine is performed to optimize the SRV airfoil sections and the planform geometry for minimum overall viscous drag. The design method allows for a fast turnaround time, and is thus suitable for system level design and parameter studies.

As a test example, a set of SRVs was designed for a six-bladed propeller at a high propeller loading condition ($C_{T,P} = 0.322$) with a Reynolds number of 5.90×10^4 relative to the blade chord length at 70% radial position and freestream velocity of 29 m/s. The flowfield around the propeller was simulated with a RANS solver, after which the resulting velocity fields in the propeller slipstream were used as input to the SRV design procedure. A parametric study was performed of the SRV performance as a function of the blade count and radius. It was concluded that the maximum SRV thrust could be obtained with a blade count of 9 and vane radius equal to that of the propeller. For this case, it was estimated that 4.1% of the propeller thrust could be produced by the SRVs.

To validate the design routine, an experiment was performed with a propeller and SRVs in a low-speed open-jet wind tunnel. Because of practical constraints, a blade count of 4 was chosen instead of the identified optimum of 9. The thrust generated by the SRVs was measured with load cells mounted on sliding bearings. At the J value for which the SRV was optimized ($J = 0.6$), the SRVs generated a thrust of 2.6% of that of the propeller, which is smaller than the value of 3.4% predicted by the lifting line method. The fact that the installation of the SRVs does not increase the required power input, this indicates the same amount of improvement in the system propulsive efficiency. The thrust coefficient of the SRVs diminishes to 1.5% of the propeller thrust at a cruise condition of $J = 1.0$.

The propeller performance was characterized by balance measurements. The

measurements showed that the upstream effect of the SRVs on the propeller performance was negligible. Since the SRVs provided thrust at all the measured advance ratios ($J = 0.6$ up to 1.0), and did not require any extra power input, the propulsive efficiency of the system (propeller + SRVs) improved accordingly, for all flight phases considered.

The above chapter demonstrates that it is possible to obtain propulsive gains by installing SRVs in the wake of an isolated tractor propeller. Most propellers, however, do not fly in isolated configurations, but are mounted on wings. In the next chapter, the swirl recovery design is provided for the wing-installed tractor propeller configuration. A design framework based a multi-fidelity optimization algorithm is established. Different swirl-recovery layouts are investigated in order to identify the optimum layout giving the optimal system performance.

Chapter 4 Numerical Investigation of Configurations with Optimum Swirl Recovery for Installed Propeller Propulsion Systems

4.1 Introduction

In the previous chapter, the design process of SRVs for uninstalled propeller propulsion systems was established. The design procedure is presented together with a test example, followed by the discussion of the experimental validation of the propeller-SRVs model. In this chapter, the swirl recovery design is dedicated for the wing-installed tractor propeller configuration.

Since propeller propulsion has a long history in aviation, many studies have been dedicated to its integration with other aircraft components. It was recognized that the aerodynamic interaction between the propeller and other aerodynamic surfaces produces both time-averaged and unsteady loads which have an effect on the aircraft aerodynamic performance, stability and control, structural loading, and production of noise and vibration [90,91]. Among many investigations of the propeller effect on the wing performance, Kroo [23] and Miranda [92] demonstrated numerically that reduction of drag can be achieved by propeller-wing interaction due to the recovery of the swirl in propeller slipstream by the trailing wing. This conclusion was verified experimentally for tractor-propeller configurations by Witkowski [42]. As pointed out by Veldhuis [16], further performance improvement of drag reduction can be obtained by properly adapting the wing loading distribution.

As mentioned in Sec. 1.3, in the study of Stokkermans [46], SRVs designed for isolated propeller were investigated in wing-mounted configuration by means of RANS simulations. Results showed that the SRVs performance degrades significantly due to flow separation caused by wing-induced velocities. However, by manually adjusting the pitch angle of the

---

The work of this chapter has been published entitled "Numerical Investigation of Configurations with Optimum Swirl Recovery for Propeller Propulsion Systems," in *AIAA Journal*, Vol. 57, No. 4, 2019, pp. 1502-1513.

vanes in RANS simulations, benefit was gained in terms of either improved wing performance or system propulsive efficiency. This implies that an integrated SRV design taking the wing effect into account will most likely result in a performance benefit in practice.

As demonstrated by Witkowski [42], the drag reduction due to a propeller slipstream for a wing-tractor configuration originates from the tilting of the aerodynamic force by the swirl velocity in the propeller slipstream. When SRVs are introduced in the slipstream, both the magnitude and azimuthal distribution of swirl velocity will be changed in front of the wing so that the tilting of the force on the wing will be changed correspondingly. Therefore, an integrated design should be performed combining both thrust production from the vanes and induced-drag reduction from the wing.

Although SRV design for maximum thrust and wing optimization for minimum induced-drag have been investigated separately, it has not been studied yet whether it is beneficial to combine these two components. No research has been performed on how to integrate SRV with a wing that employs a propeller propulsion system. This chapter is conducted to fill this gap.

4.2 Methodology

Since there are three components in a tractor propeller-SRV-wing system, three modules in the design procedure are established correspondingly. These three modules are: 1) the analysis module of the isolated propeller to establish the flowfield of slipstream, 2) the SRV design module in the propeller-wing-induced velocity field, and 3) the wing analysis module in the propeller-SRV induced velocity field. The modular design process of SRV and/or wing for a tractor propeller is shown in Figure 4.1. It should be noted that the analysis of this chapter is performed with neglect of viscosity, and the effect of including viscosity will be further investigated in the next chapter.

The description of the velocity field induced by the propeller is achieved by performing a RANS simulation of the isolated propeller as was done in Sec. 3.3.1. The perturbations of the propeller performance due to the addition of the SRV and the wing are neglected as was mentioned in Sec. 2.4, so that during the design process of swirl recovery system, the amount of the swirl in the slipstream is maintained constant.

With respect to SRV and wing design, a multi-fidelity optimization algorithm is utilized. A potential flow-based analysis is adopted as the low-fidelity method for fast convergence. The solutions to the Euler equations are used as the high-fidelity method for higher accuracy of performance determination of the whole system. The multi-fidelity optimization is a double-loop process including an inner loop and an outer loop. The inner loop corresponds to a lift-constrained drag-minimization problem performed with low-fidelity method, and the outer loop corresponds to an alignment procedure between the low-fidelity model and high-fidelity model using a correction algorithm. The details of each design/analysis module and the optimization process are described as follows.

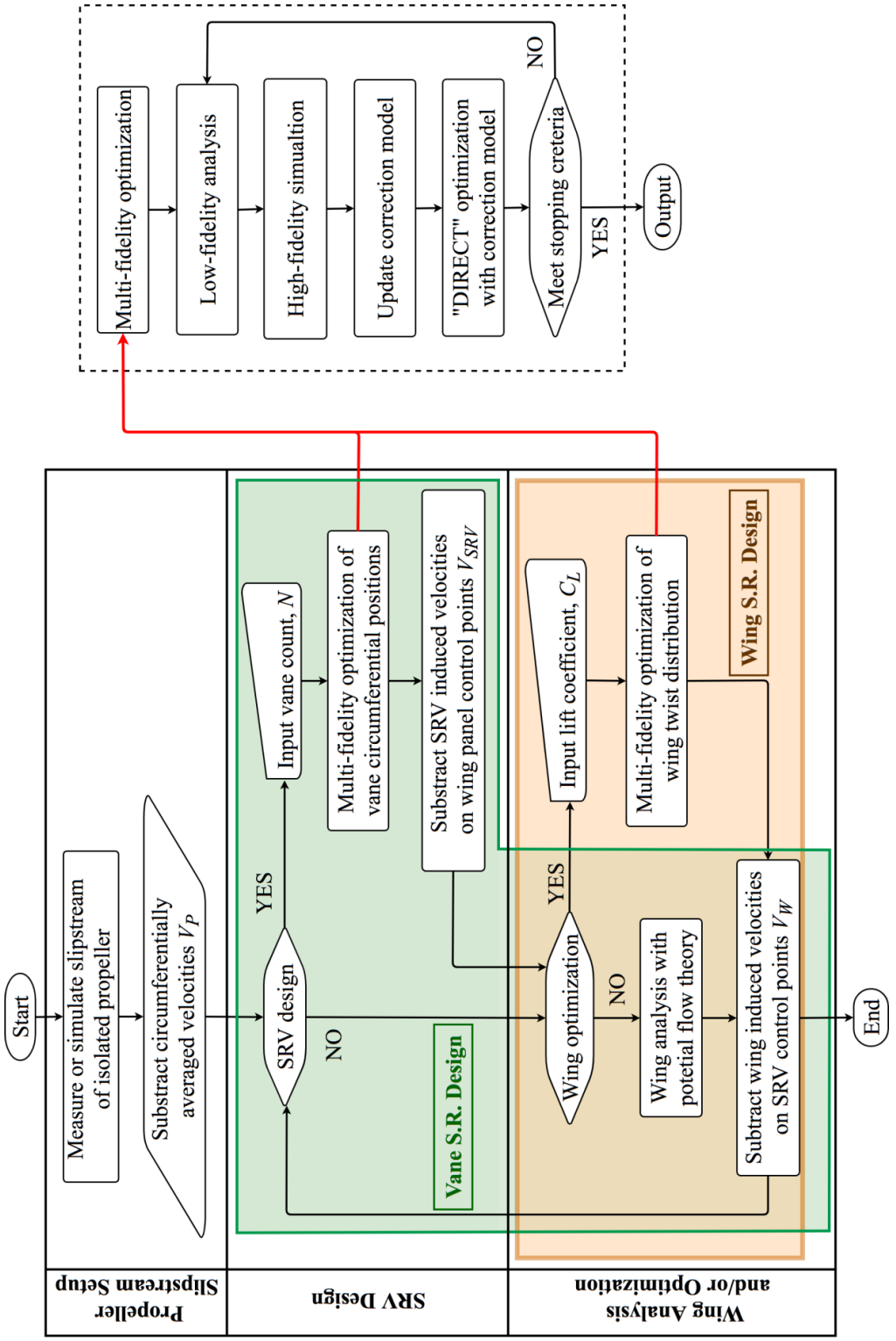

Figure 4.1 Modular design process of swirl recovery system for installed tractor propellers.

4.2.1 Propeller slipstream setup

Since the cruise phase of flight accounts for the most significant portion of total mission fuel burn for commercial flights [93], the design condition is set as the cruise condition of a typical turboprop aircraft ATR-72. The aircraft is equipped with two sets of propeller propulsion systems [94]. The properties of the aircraft and its cruise flight condition are listed in Table 4.1.

Table 4.1 Properties of ATR 72 aircraft [95,96]

Variable	Value
Wing area, S	61 m^2
Maximum take-off weight, m_{MTO}	22800 kg
Cruise altitude	5000 m (air density ρ = 0.7364 kg/m^3)
Cruise speed (Ma)	140 m/s (0.44)
Lift-to-drag ratio at cruise, L/D	17.2

Based on the aircraft properties listed above, the lift and drag coefficients of the aircraft at cruise condition are calculated to be:

$$C_{L,aircraft} = \frac{m_{MTO} g}{\frac{1}{2}\rho V_\infty^2 S} = 0.5076 \approx 0.5 \tag{4.1}$$

$$C_{D,aircraft} = \frac{C_{L,aircraft}}{L/D} = 0.0294 \tag{4.2}$$

The lift of the aircraft is assumed to be only from the wing such that $C_{L,W} = C_{L,aircraft} = 0.5$. The drag experienced by the aircraft should be compensated by the two sets of the propeller propulsion systems in order to achieve equilibrium condition during cruise. This can be achieved by the propeller of Figure 3.5 ($D_P = 0.406$, $N = 6$) at an advance ratio J of 2.4 and the blade pitch angle (measured at 70% radius) at 50° according to the RANS simulation presented below.

In the RANS simulation, the computational mesh of the isolated propeller is the same as that was described in Sec. 3.3.1, where the simulation results were validated by experimental data in terms of both the propeller performance coefficients and the velocity distributions in the propeller slipstream. Since the current case is performed at more benign conditions (lower propeller thrust coefficient and higher Reynolds number) compared to the previous validation, no new validation is considered as necessary. The propeller is positioned at zero incidence angle relative to the freestream velocity. The thrust coefficient $T_{C,P}$ (multiplied by two since there are two propellers on the aircraft) is computed to be ($T_{C,P}$ is defined based on the freestream dynamic pressure and the wing area):

$$T_{C,P} \equiv \frac{T_P}{0.5\rho V_\infty^2 S} = 0.0294 = C_{D,aircraft} \tag{4.3}$$

and the propeller efficiency is computed to be $\eta_P = 81.0\%$.

In Figure 4.2, the axial development of the circumferentially-averaged axial velocity V_a and tangential velocity V_t produced by the propeller is depicted on five survey planes perpendicular to the propeller axis. Their axial distance to the propeller plane ranges from $0.5R$ to $2.5R$. It can be observed that the distributions of V_t exhibit a negligible change when the slipstream develops downstream. While, the axial velocity increases along the axis up until the plane at $x = 1.5R$ and keeps practically constant afterwards.

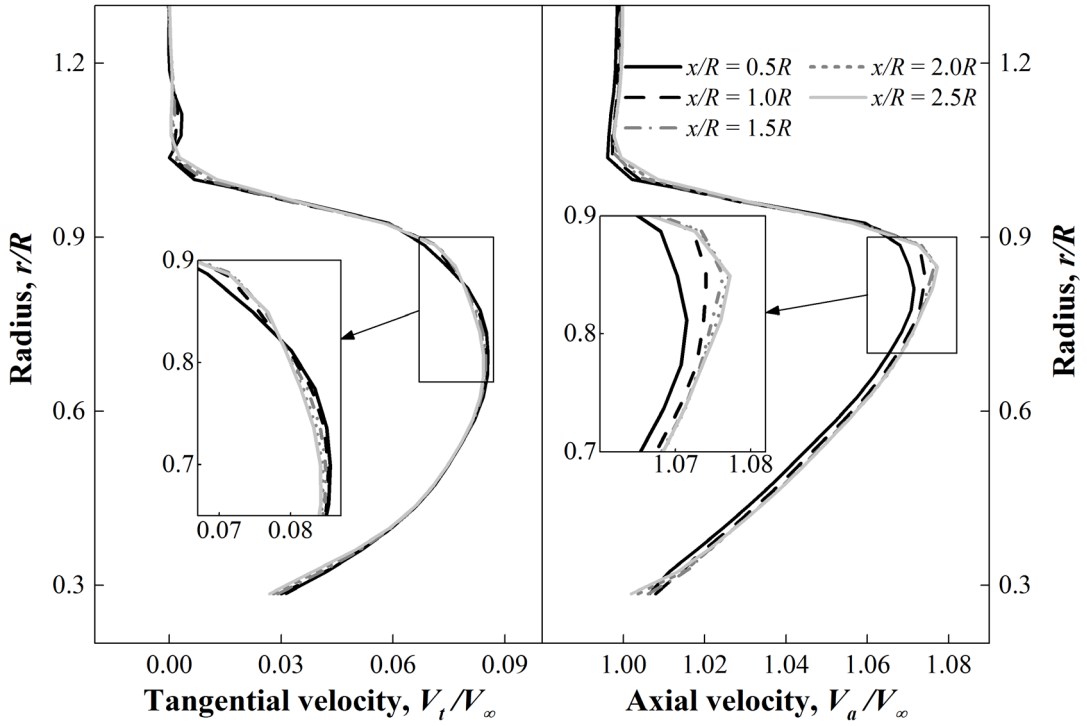

Figure 4.2 Circumferentially-averaged tangential (left) and axial (right) velocity distributions in propeller slipstream obtained from RANS simulation of the isolated propeller at $J = 2.4$, $T_{C,P} = 0.0294$ and $\beta_{0.7R} = 50°$.

4.2.2 Low-fidelity potential flow-based analysis of propeller-SRV-wing configuration

The flowfield of propeller slipstream is determined by a RANS simulation of the isolated propeller as discussed above, and the circumferentially-averaged velocity distributions in the slipstream are taken as input information for SRV and wing design. A lifting line model is used for SRV design and a surface singularity method is utilized for wing performance analysis. A full coupling between SRV design and wing analysis is established where iterations are performed until both are converged. However, the upstream effect of the wing and the SRVs on propeller performance is neglected. This is considered to be acceptable since the main focus of this chapter is on the comparison of the swirl-recovery performance of the wing and the SRVs at a given propeller working condition. Moreover, in the potential flow-based analysis, the deformation of the propeller slipstream due to its interaction with either SRV or wing is also neglected. The neglect of the slipstream deformation will be corrected by the high-fidelity method during the multi-fidelity optimization process.

4.2.2.1 SRV design with circumferentially non-uniform inflow

A design procedure of SRVs for uninstalled propeller was established in Sec. 3.3.1 based on a lifting-line model. From time-averaged point of view, the velocity field behind the isolated propeller is circumferentially uniform. Hence, the SRVs designed for an isolated propeller are uniformly distributed along the azimuthal direction, and all of the vanes have the same loading distribution. However, in installed configuration, the circumferential uniformity is altered by the wing-induced velocities. The design procedure of SRVs is thus adapted in the way that first, the vane loadings are uniquely dependent on their azimuthal positions with specific inflow velocities, and second, the azimuthal positions of the vanes (φ as defined in Figure 4.3) are optimized for maximum thrust production. The azimuthal angle of SRV φ is defined as 0° and 180° when the vane is in vertical position and points upward and downward respectively, while 90° and 270° indicate the vane in their horizontal position on the blade-downgoing and upgoing side respectively.

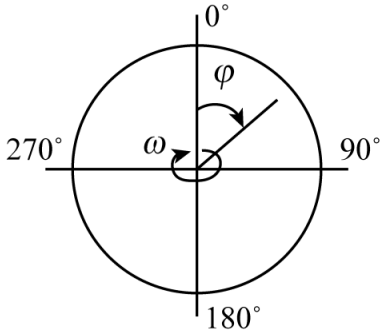

Figure 4.3 Definition of the azimuthal angle φ of the SRV
(front view, the propeller has a clockwise rotation).

For determination of azimuthal angles of SRVs, the global optimization algorithm DIRECT (abbreviation of "DIviding RECTangles") is used which will be introduced later in Sec. 4.2.4. With the azimuthal positions fixed, the determination of the optimum loading distributions of the vanes is required. The inflow velocities at vane positions are obtained by summation of freestream velocity, and velocities induced by the propeller and the wing. Following the velocity and force diagram shown in Figure 3.9 and the terms used previously in Sec. 3.3.1, the SRV thrust is determined by application of the Kutta-Joukowski's theorem which can be expressed as:

$$T_V = \rho N \sum_i \sum_j \left[(V_{t_{i,j}} + v_{t_{i,j}}) \Gamma_{i,j} - \frac{1}{2} V_{i,j}^* C_{d_{i,j}} c_{i,j} (V_{a_{i,j}} + v_{a_{i,j}}) \right] \Delta r_{i,j} \tag{4.4}$$

The axial and tangential inflow velocities include both the propeller-induced and the wing-induced components such that the influences from both the propeller and the wing on SRV performance are taken into account. In order to have maximum thrust, the partial derivative of T_V with respect to the circulation distribution is set to zero:

$$\frac{\partial T_V}{\partial \Gamma_{i,j}} = 0 \tag{4.5}$$

where the derivative is given by:

$$\begin{aligned}\frac{\partial T_V}{\partial \Gamma_{i,j}} = (V_{t_{i,j}} + v_{t_{i,j}})\Delta r_{i,j} + \sum_{\bar{j}}\sum_{\bar{i}} \frac{\partial v_{t_{\bar{i},\bar{j}}}}{\partial \Gamma_{i,j}} \Gamma_{\bar{i},\bar{j}} \Delta r_{\bar{i},\bar{j}} \\ - \sum_{\bar{j}}\sum_{\bar{i}} \frac{1}{2} \frac{\partial V^*_{\bar{i},\bar{j}}}{\partial \Gamma_{i,j}} C_{d_{\bar{i},\bar{j}}} c_{\bar{i},\bar{j}} (V_{a_{\bar{i},\bar{j}}} + v_{a_{\bar{i},\bar{j}}}) \Delta r_{\bar{i},\bar{j}} \\ - \sum_{\bar{j}}\sum_{\bar{i}} \frac{1}{2} V^*_{\bar{i},\bar{j}} \frac{\partial (C_{d_{\bar{i},\bar{j}}} \cdot c_{\bar{i},\bar{j}})}{\partial \Gamma_{i,j}} (V_{a_{\bar{i},\bar{j}}} + v_{a_{\bar{i},\bar{j}}}) \Delta r_{\bar{i},\bar{j}} \\ - \sum_{\bar{j}}\sum_{\bar{i}} \frac{1}{2} V^*_{\bar{i},\bar{j}} C_{d_{\bar{i},\bar{j}}} c_{\bar{i},\bar{j}} \frac{\partial v_{a_{\bar{i},\bar{j}}}}{\partial \Gamma_{i,j}} \Delta r_{\bar{i},\bar{j}}\end{aligned} \tag{4.6}$$

As discussed in Sec. 3.3.1, the distributions of the sectional drag coefficient C_d and chord length *c* have negligible effect on the optimum circulation distribution. Thus, the terms including either C_d or *c* on the right hand side of Eq. (4.6) can be neglected and Eq. (4.5) can be rewritten as:

$$\frac{\partial T_V}{\partial \Gamma_{i,j}} = (V_{t_{i,j}} + v_{t_{i,j}})\Delta r_{i,j} + \sum_{\bar{j}}\sum_{\bar{i}} \frac{\partial v_{t_{\bar{i},\bar{j}}}}{\partial \Gamma_{i,j}} \Gamma_{\bar{i},\bar{j}} \Delta r_{\bar{i},\bar{j}} = 0 \tag{4.7}$$

The partial derivatives of the induced tangential velocities with respect to the bound circulations ($\frac{\partial v_{t_{\bar{i},\bar{j}}}}{\partial \Gamma_{i,j}}$) are computed by Biot-Savart's law. A non-linear system of equations is formulated with circulation strength of vane lifting segments as independent variables. The equation system is solved by Newton's method.

Once the circulation distributions of the vanes are determined, the induced velocities from the vanes on the wing collocation points can be calculated using Biot-Savart's law. In order to perform Euler simulation in the high-fidelity process, the vane shapes also need to be determined. With a prescribed circulation distribution, there are infinite numbers of vane shape which can achieve this distribution. The one used here employs a NACA 2412 airfoil shape. The chord length of the vane sections is proportional to their local circulations with the maximum equals that of the propeller root. The local incidence angles of the vane sections are adjusted to maintain the desired circulation distribution.

4.2.2.2 Wing analysis with surface singularity method

The wing performance is obtained with potential flow-based surface singularity (or panel) method considering interaction effects from the propeller and SRVs. The details are given as below.

1) Potential flow formulation

When the flow surrounding the wing is assumed to be inviscid, irrotational and incompressible, a scalar velocity potential Φ_{Total} can be defined such that the continuity of

mass is governed by the Laplace's equation as:

$$\nabla^2 \Phi_{Total} = 0 \tag{4.8}$$

Following Green's identity, applying the boundary element discretization of Laplace's equation to a traditional wing geometry results in the following integrals for calculating the perturbation potential from the wing ($\Phi_W = \Phi_{Total} - \Phi_\infty - \Phi_P - \Phi_V$ where Φ_P and Φ_V are perturbation potential from the propeller and SRV respectively):

$$\Phi_W = \frac{1}{4\pi}\int_{S_{bound}+S_{wake}} \mu \frac{\partial}{\partial \boldsymbol{n}}\left(\frac{1}{\|\boldsymbol{\Omega}\|}\right) dS - \frac{1}{4\pi}\int_{S_{bound}} \sigma\left(\frac{1}{\|\boldsymbol{\Omega}\|}\right) dS \tag{4.9}$$

where μ and σ are strength of doublet and source respectively, $\boldsymbol{n}$ is outward unit normal vector of wing panels, S_{bound} and S_{wake} refer to the singularities distributed on the wing surface and wake respectively, and $\boldsymbol{\Omega}$ is the position vector. By applying Dirichlet boundary condition, the internal potential is set to zero as:

$$\frac{1}{4\pi}\int_{S_{bound}} \mu_b \frac{\partial}{\partial \boldsymbol{n}}\left(\frac{1}{\|\boldsymbol{\Omega}\|}\right) dS - \frac{1}{4\pi}\int_{S_{bound}} \sigma\left(\frac{1}{\|\boldsymbol{\Omega}\|}\right) dS + \frac{1}{4\pi}\int_{S_{wake}} \mu_w \frac{\partial}{\partial \boldsymbol{n}}\left(\frac{1}{\|\boldsymbol{\Omega}\|}\right) dS = 0 \tag{4.10}$$

where μ_b and μ_w are doublets distributed on the wing surface and wake respectively, and the wake potential jump μ_w is determined by a Kutta condition imposed at the trailing edge of the lifting surface. The wake is prescribed as a drag-free wake of which the panels are aligned with the freestream velocity. Setting up the source strength to:

$$\sigma_i = \boldsymbol{n_i} \cdot (\boldsymbol{V_\infty} + \boldsymbol{V_{P,i}} + \boldsymbol{V_{V,i}}) \tag{4.11}$$

($\boldsymbol{V_P}$ and $\boldsymbol{V_V}$ are propeller and SRV induced velocities on the wing collocation points respectively) results in the value of the doublets as unknowns.

2) Panel pressure and force

Once the strengths of singularities are determined, the velocity induced by the wing $\boldsymbol{V_W}$ is computed by calculating the gradient of the doublet distribution. The pressure on the wing surface can be obtained through Bernoulli's equation. To account for the compressibility effect, the Prandtl-Glauert correction is applied, and the pressure coefficient is given as:

$$C_{p,i} = \left(1 - \frac{(\boldsymbol{V_\infty} + \boldsymbol{V_{P,i}} + \boldsymbol{V_{V,i}} + \boldsymbol{V_{W,i}})^2}{(\boldsymbol{V_\infty} + \boldsymbol{V_{P,i}} + \boldsymbol{V_{V,i}})^2}\right) / \sqrt{1 - M_{a_\infty}^2} \tag{4.12}$$

The aerodynamic force on the panel can be computed as:

$$\Delta \boldsymbol{F_i} = -C_{p,i}\left[\frac{1}{2}\rho(\boldsymbol{V_\infty} + \boldsymbol{V_{P,i}} + \boldsymbol{V_{V,i}})^2\right]\Delta S_i \boldsymbol{n_i} \tag{4.13}$$

The total force of wing is then obtained by integrating the forces of all the wing surface panels.

3) Induced drag calculation by Trefftz-plane analysis

The induced drag of the wing is calculated by the Trefftz-plane analysis. The readers can refer to Ref. [16] for the physical explanation and equation derivation of this method. The Trefftz-plane analysis has been proven by many authors to be capable of providing accurate predictions of the induced drag [97,98]. The calculation can be accomplished by virtue of Kutta-Joukowski's theorem in the drag direction on the Trefftz-plane by calculating the line integral:

$$D_I = \frac{1}{2}\int \rho\left(\boldsymbol{V}_{P,i} + \boldsymbol{V}_{V,i} + \boldsymbol{V}_{W,i}\right)\cdot \boldsymbol{n}_i \Gamma_i dl_i \tag{4.14}$$

Originating from three different sources of induced velocities on the wing, three components are identified, i.e. the wing self-induced drag (by $\boldsymbol{V}_W$), the propeller-induced drag (by $\boldsymbol{V}_P$), and the SRV-induced drag (by $\boldsymbol{V}_V$). All these induced drag components are computed by the method proposed by Blackwell [99]. It should be noted that the viscous drag of the wing is assumed to be constant, thus it is not included in the optimization procedure.

4.2.3 High-fidelity Euler equation-based simulation of propeller-SRV-wing configuration

In the potential flow-based method, the deformation of the slipstream is neglected. This is done in order to achieve fast computation when performing optimization. However, as observed by Veldhuis [16] and discussed in Sec. 2.5, a strong deformation of the slipstream symmetry exists when the wing is positioned at a positive angle of attack. The inaccuracy resulting from the neglect of the slipstream deformation can be corrected by a higher fidelity method which employs full coupling interaction of the propeller slipstream, SRV and wing. Since the aerodynamic theory used in the potential flow method is inviscid, a natural choice for the higher fidelity model is an Euler equation-based solver.

The propeller in Euler equation-based simulation is represented by an actuator disk in order to maintain the same velocity distributions in the slipstream as those obtained from the RANS simulation. The radial distributions of propeller thrust and torque are replaced by axial and angular momentum sources in the actuator disk model. The resolution of the wing solid surface, the refinement of propeller slipstream region, the wake of the wing, and tip vortex region of the wing are similar to that discussed by Lötstedt [100], where the mesh size and topology were validated by the experimental data for a tractor propeller-wing configuration. The same strategy was also applied to the vanes by scaling down the mesh size based on the chord length ratio of the SRV and the wing. The simulations were performed with the finite volume-based solver ANSYS® CFX.

4.2.4 Global optimization by DIRECT algorithm

The design of the swirl recovery system for propeller propulsion system is achieved by optimizing the summation of the thrust production from the vanes and the induced drag reduction of the wing, while maintaining total lift constant. The optimization problem can be

stated as follows:

$$\begin{aligned} &\underset{X\in\Re^D}{\text{minimize}} && -T_{C,V}(X)+C_{D,i}(X) \\ &\text{subject to} && C_{L,W}(X)+C_{L,V}(X)=\text{constant} \end{aligned} \tag{4.15}$$

where the thrust and lift coefficients of SRV ($T_{C,V}$ and $C_{L,V}$), and the induced drag and lift coefficients of the wing ($C_{D,i}$ and $C_{L,W}$), are all defined based on the freestream dynamic pressure and the wing area as:

$$T_{C,V}, C_{L,V}, C_{D,i}, C_{L,W} = \frac{T_V, L_V, D_I, L_W}{0.5\rho V_\infty^2 S} \tag{4.16}$$

The gradient-free DIRECT optimization algorithm is used to achieve a global optimization, where DIRECT stands for "DIviding RECTangles" [101]. This optimization algorithm, which was proposed by Jones [101], is a modification of the standard Lipschitzian approach [102]. By identifying the potentially optimal intervals, the algorithm balances its effort between global and local searches of the objective function to guarantee a global optimum. The successful application of DIRECT algorithm in aerodynamic optimization has been reported by many authors [103,104,105]. This algorithm is found suitable for global optimization problems with bound constraints and a real-valued objective function where the objective function is a "black box" function or evaluation. The non-linear constraint of the constant total lift in Eq. (4.15) is treated implicitly during the optimization loop in the way that for a given wing geometry, the wing angle of attack is adjusted to acquire the desired total lift. The incidence of the propeller and the SRV, however, is kept constant (at zero angle of attack). Thus, the original non-linear constraint optimization problem is relieved to a bound constraint optimization problem that can be solved by DIRECT optimization as:

$$\begin{aligned} &\underset{X\in\Re^D}{\text{minimize}} && -T_{C,V}(X)+C_{D,i}(X) \\ &\text{subject to} && X\in[X_{\min}, X_{\max}] \end{aligned} \tag{4.17}$$

4.2.5 Multi-fidelity optimization using shape-preserving response prediction algorithm

To reduce the number of evaluations of the high-fidelity models, a surrogate-based optimization (SBO) technique is utilized. Normally, the figures of interest in the optimization are aligned between the low-fidelity and high-fidelity models using a correction procedure. In case of aerodynamic shape optimization, since the figures of interest ($T_{C,V}, C_{D,i}, C_{L,W}$ and $C_{L,V}$ in this case) are simply scalars for a given design input, a large amount of low- and high-fidelity data are required to generate the response surfaces of the figures of interest. In order to reduce the computation time, the model alignment procedure adopted in this work is performed not directly to the figures of interests, but to the intermediate simulation results, more specifically, the circulation distribution of the vanes, and the lift and circulation distributions of the wing. As the objective and constraint of the optimization problem are

uniquely determined by these distributions, alignment of the corresponding distributions for the low- and high-fidelity models will result in an alignment of the objective and constraint. Thus, the low-fidelity potential flow-based surrogates are corrected to become a reliable representation of the high-fidelity Euler equation-based model. By using the SBO technique, the optimization burden is shifted to the low-cost low-fidelity surrogate model, whereas the high-fidelity model is referenced occasionally for verification purposes only.

The shape-preserving response prediction (SPRP) methodology [106] is adopted for the model alignment. In Figure 4.4, an example of the application of SPRP alignment procedure on the wing circulation distribution is depicted. We denote the circulation distributions from the Euler solution and potential flow-based results as Γ_E and Γ_p respectively. At the beginning of multi-fidelity optimization, the global optimization is carried out based on the low-fidelity method so that Γ_p is obtained. After that, the optimum design obtained from the low-fidelity optimization is simulated by high-fidelity Euler solver so that Γ_E is obtained. The SPRP alignment is established by determining the translation vectors of corresponding circulation distributions, i.e., the difference between Γ_p and Γ_E. The model alignment between low fidelity and high fidelity is constructed assuming that the change of Γ_E due to adjustment of the wing shape in the next iteration of global optimization can be predicted using the change of Γ_p. Thus, the SPRP model is applied to the samples of the low-fidelity analysis during the new iteration of global optimization. The formulations for the vane circulation and wing lift distribution are analogous.

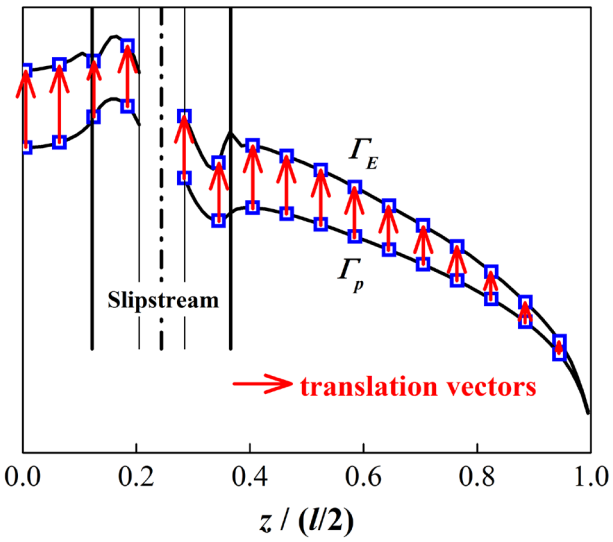

Figure 4.4 Correction of the wing circulation distribution obtained from the low-fidelity potential-based model by that obtained from the high-fidelity Euler equation-based model utilizing SPRP methodology.

4.3 Swirl recovery design of trailing wing for a tractor propeller

In order to compare the capability of swirl recovery from the trailing wing and the SRV, the swirl recovery design is implemented firstly on the trialing wing (twist distribution) without the SRV installed as introduced in this section (Sec. 4.3), and secondly on the SRV

with an untwisted wing as introduced in Sec. 4.4. Comparison of swirl recovery from the wing and the SRV is then made in Sec. 4.5.

The propeller model shown in Figure 3.5 is used throughout this chapter. The geometry of the wing model (Figure 4.5) is based on a scaled down and simplified version of the Fokker 50 wing, where Fokker 50 is a turboprop-powered airliner. The wing is scaled down such that the ratio of the propeller diameter to the wing span is kept constant. The dihedral of the outer 75% wing span, the sweep and twist of the quarter chord line of the original wing are neglected. These simplifications are considered reasonable since the goal is just to have a representative wing for a tractor configuration. Since the mechanism of swirl recovery is inherently inviscid, the conclusion drawn from the investigation of the scaled model is justifiable to the original aircraft regardless of the Reynolds-number difference. The propeller has an inboard-up rotation. Its rotation axis is one propeller diameter from the wing root in spanwise direction. The rotation plane is parallel to and one propeller diameter upstream of the wing quarter chord line.

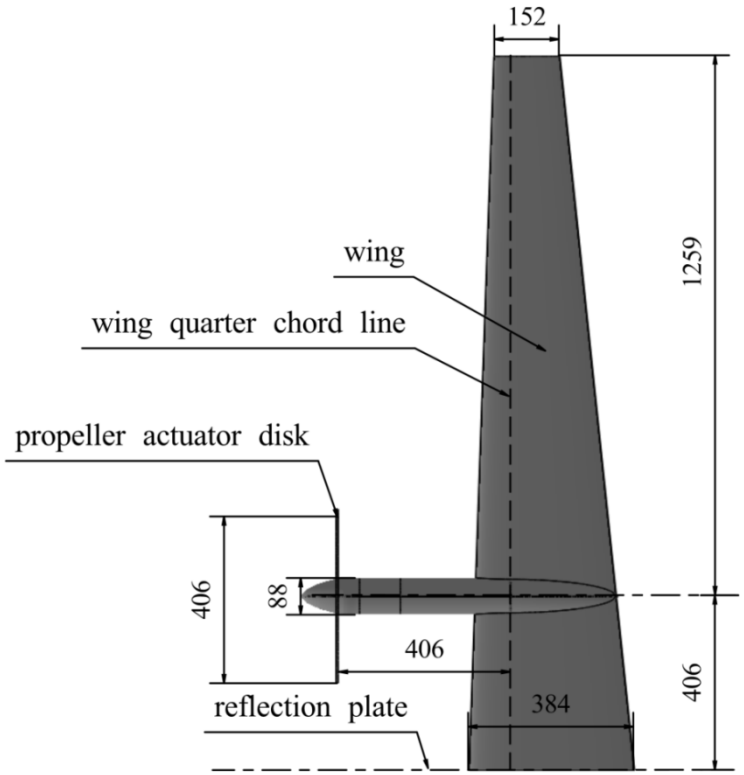

Figure 4.5 Dimensions of the propeller and wing model (unit in millimeters, top view). The geometry of the wing model is based on a scaled down and simplified version of the Fokker 50 wing.

The swirl recovery by a trailing wing with a tractor propeller results in a reduction in wing-induced drag, of which the mechanism was well explained by Witkowski [42]. In order to achieve the lift distribution with minimum induced drag, the twist distribution is optimized. The distribution is represented by a B-spline curve with 8 control points located at 8 spanwise locations as shown in Figure 4.7. The upper and lower bounds of twist angle are set to 0° and 8° respectively (so that the range is larger than the maximum difference of the optimum twist angles). The half wing is mirrored to the full span in the analysis of potential-based method. The wing lift coefficient, which equals 0.5 at cruise condition as calculated in Sec. 4.2.1, is set as an implicit constraint during the twist optimization. The wing is

represented by singularities distributed on 200 spanwise panels and 23 chordwise panels. Since the lift and circulation distributions will be corrected by the high-fidelity Euler solutions, these panel numbers are adequate to resolve the integrated loads ($C_{L,W}$ and $C_{D,i}$) within 0.1% of accuracy when provided with the distributions obtained by high-fidelity solutions.

4.3.1 Convergence of multi-fidelity optimization

As illustrated in Figure 4.1, the multi-fidelity optimization is a double-loop procedure. The inner loop is performed on the low-fidelity potential-based method with DIRECT global optimization algorithm, and stopped when the number of evaluations exceeds 100 times the number of design variables (which is 8 in this case). The outer loop is terminated when the difference of induced drag between the current and the previous loop is less than 0.2 counts (1 count corresponds to drag coefficient of 0.0001).

As shown in Figure 4.6, the multi-fidelity optimization of wing twist distribution has converged after 3 outer loops. At top of the figure, the convergence history of each inner loop (DIRECT global optimization) is illustrated, and at bottom the optimum twist distributions of different inner loops are compared. The induced drag has decreased by 3.9 counts after optimization compared to that of the untwisted wing. This amount of drag reduction is equivalent to 1.3% of propeller thrust. The optimum twist distributions of three inner loops exhibit the same shape which further confirms the convergence of the multi-fidelity optimization. In general, the optimum twist distribution is characterized by higher value inside the slipstream, and lower value at the tip. Due to the lift constraint, the loading is allocated more to the region where the lift-drag ratio is higher, which is the wing part immersed in the slipstream. The twist angle is lowest at the wing tip to reduce the strength of tip vortex and thus to reduce tip loss.

4.3.2 Design space exploration of twist distribution by DIRECT algorithm

By balancing between global and local searches, the DIRECT algorithm is guaranteed to converge to the global optimum provided that the objective function is continuous [101]. Figure 4.7 illustrates the response surface of the wing-induced drag against twist angles at control points obtained from the third inner loop. It should be noted that each scatter point in this figure represents multiple samples in the optimization due to the fact that for a given combination of two of the twist angles (τ_i, τ_j), there are multiple combinations of other twist angles (τ_k, k = 1~8 and $k \neq i, j$) evaluated during the optimization. Of all the samples, only the one with minimum response value is collected and shown in the contour.

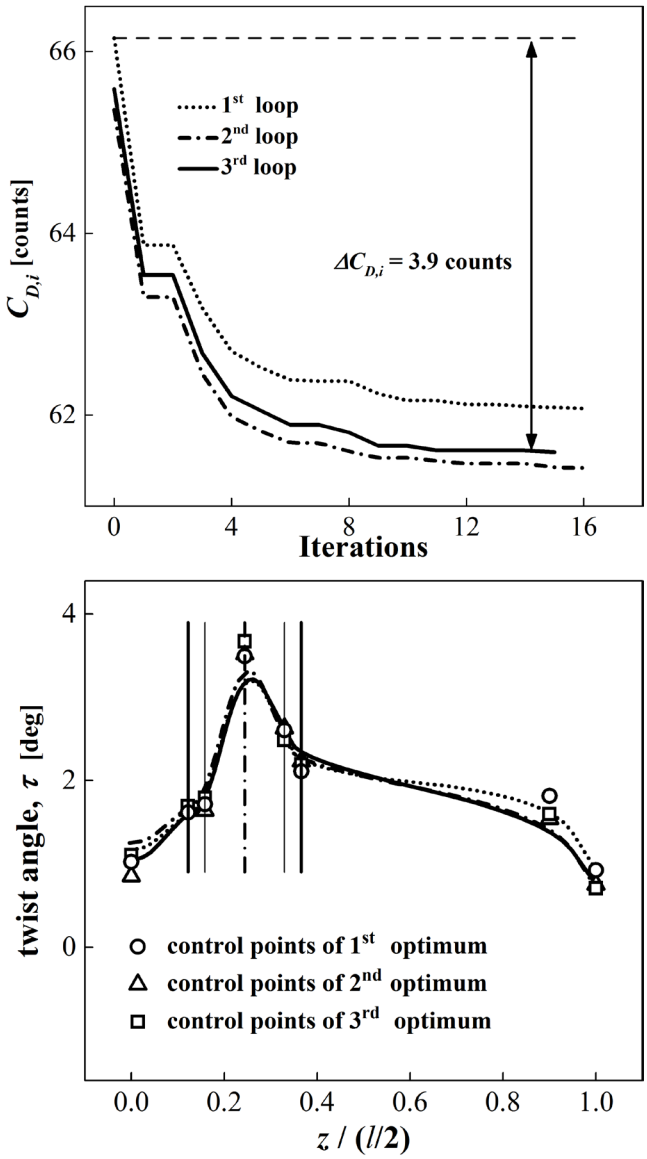

Figure 4.6 Convergence of multi-fidelity optimization of wing twist distribution;
top: convergence history of each inner loop during DIRECT optimization,
bottom: comparison of optimum twist distributions to show convergence of the outer loop.

It can be seen from Figure 4.7 that the design space is fully explored and the response surfaces exhibit a single minimum. However, this does not mean that the twist optimization can be achieved by a gradient-based optimization algorithm with one starting point, since Figure 4.7 only shows the response surface surrounding the global optimum and the actual response surface is multi-dimensional and unknown. The response variation with respect to the twist angles at the tip region (τ_7, τ_8) is much less compared to other control point locations. This indicates that the drag induced by the tip vortex is smaller than that induced by the slipstream, which will be confirmed and explained in the next section.

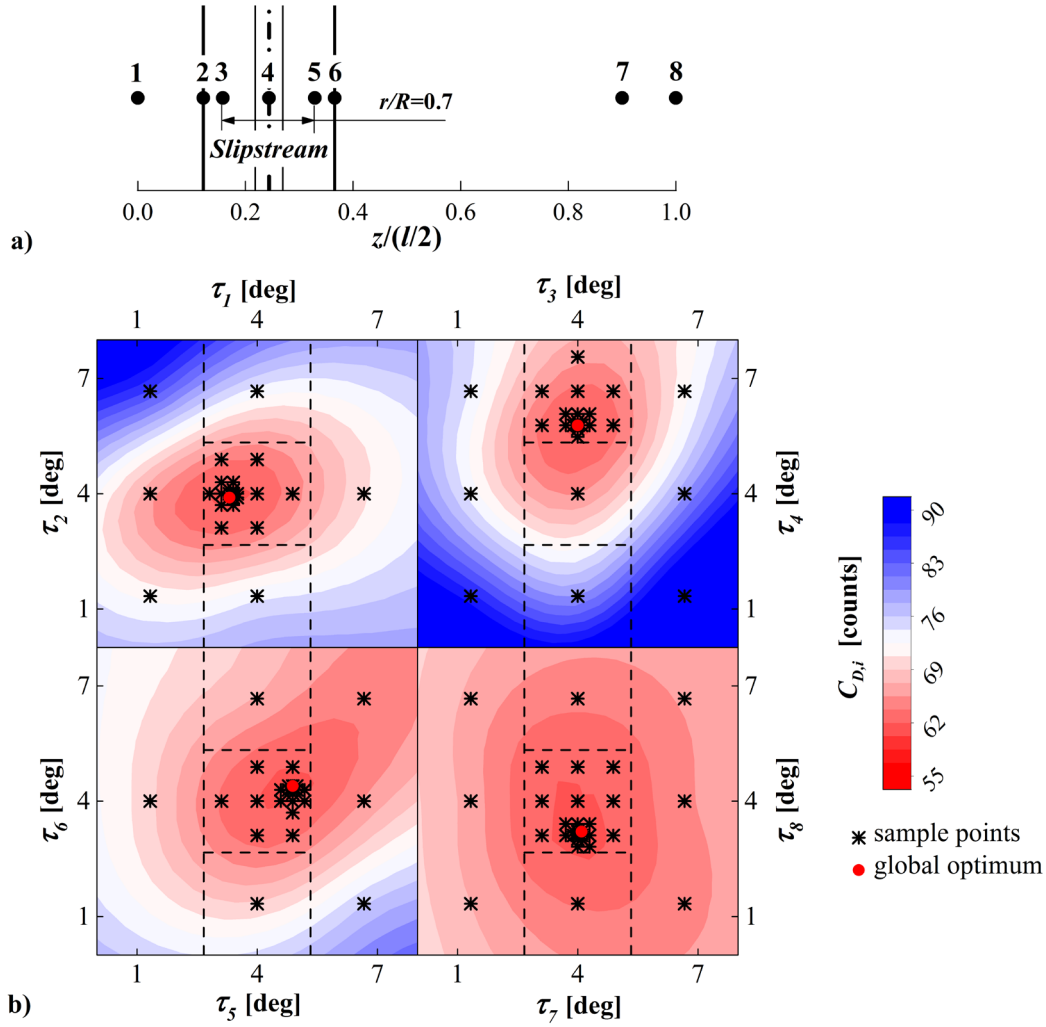

Figure 4.7 Design space exploration of wing twist optimization. The spanwise locations of control points for B-spline curve are depicted at the top.

4.3.3 Optimum spanwise loading distributions

In Figure 4.8, the spanwise lift, circulation and induced drag distributions of the wing with optimum twist distribution are presented. In Figure 4.8a and Figure 4.8b, comparisons are made of the lift and circulation distributions obtained from potential flow-based analysis (denoted as potential), potential flow-based analysis applied with SPRP model (denoted as potential-SPRP), and the Euler simulation result (denoted as Euler). The local lift coefficient of the wing C_l is defined based on the freestream dynamic pressure and the local wing area ΔS as:

$$C_l = \frac{l}{0.5\rho V_\infty^2 \Delta S} \tag{4.18}$$

The match of both lift and circulation distributions between the latter two cases again confirms the convergence of the multi-fidelity optimization procedure.

The total induced drag, which includes the wing self-induced drag and the propeller-induced drag, is shown in Figure 4.8c. The wing self-induced drag is a consequence of the downwash velocity produced by the trailing wake vorticity on the collocation points. Since

the magnitude of local induced drag is proportional to the local strength of bound circulation, the distribution of wing self-induced drag follows the same pattern of the circulation distribution in the way that the local maximum/minimum in circulation distribution results in local maximum/minimum of wing self-induced drag. Analogous to the downwash velocity induced by the trailing wake vorticity, the swirl velocity inside the propeller slipstream also induces (positive or negative) drag on the wing by tilting the lift force at wing collocation points. On the blade-upgoing side, the swirl velocity points upward and induces negative drag (or equivalently thrust) on the wing. Similarly, on the blade-downgoing side, the swirl velocity points downward and induces positive drag on the wing. Due to the fact that the wing circulation is augmented on the blade-upgoing side and diminished on the blade-downgoing side, the propeller-induced negative drag is larger in magnitude than the positive drag. However, the propeller-induced drag cancels out each other on upgoing and downgoing sides, and the total reduction in drag, in the end, is small compared to the wing self-induced drag, accounting for only 4% of the total induced drag.

It can be seen from Figure 4.8b that in the Euler simulation result, there is a local minimum in wing circulation distribution at the location of the slipstream edge on the blade-upgoing side, and a local maximum on the blade-downgoing side. These two extremes result from the interaction between the vorticity embedded in the slipstream and the wing surface as discussed in Sec. 2.5.2, and they are not captured by the low-fidelity potential flow-based analysis. This phenomenon was also observed, e.g., in Figure 5 of Ref. [80]. However, as discussed above, these extremes have a strong effect on the induced drag distribution. In this sense, it can be concluded that when performing the induced drag prediction of the wing with a tractor propeller, one should refer to a solution where the interaction between the propeller slipstream and the downstream wing is simulated.

4.4 SRV design for tractor propeller in installed configuration

By optimizing the twist distribution of the wing, the reduction of induced drag can be achieved. However, the complexity of wing geometry and subsequently the difficulty in manufacturing has increased by introducing twist distribution. This problem can be tackled by having the wing without any twist distribution but introducing a set of SRVs which also has the capability of recovering swirl. In this way, extra thrust can be generated from the vanes. However, the velocity distributions inside the slipstream will be changed by the presence of SRVs. The lift and induced drag distributions of the wing will be altered accordingly. A full coupling between SRV design and wing analysis is established. A set of SRVs is designed at the same condition with that of the wing shape optimization.

The azimuthal positions of the vanes are optimized using DIRECT algorithm. The radius of the SRVs is kept the same as that of the propeller. The wing is again represented by singularities distributed on 200 spanwise panels and 23 chordwise panels, and SRVs are discretized into 20 lifting segments. The coupling between SRV design and wing analysis is defined to be converged when the change in SRV thrust is less than 1%, which corresponds to 0.02–0.05% of propeller thrust. This is considered as a sufficient resolution.

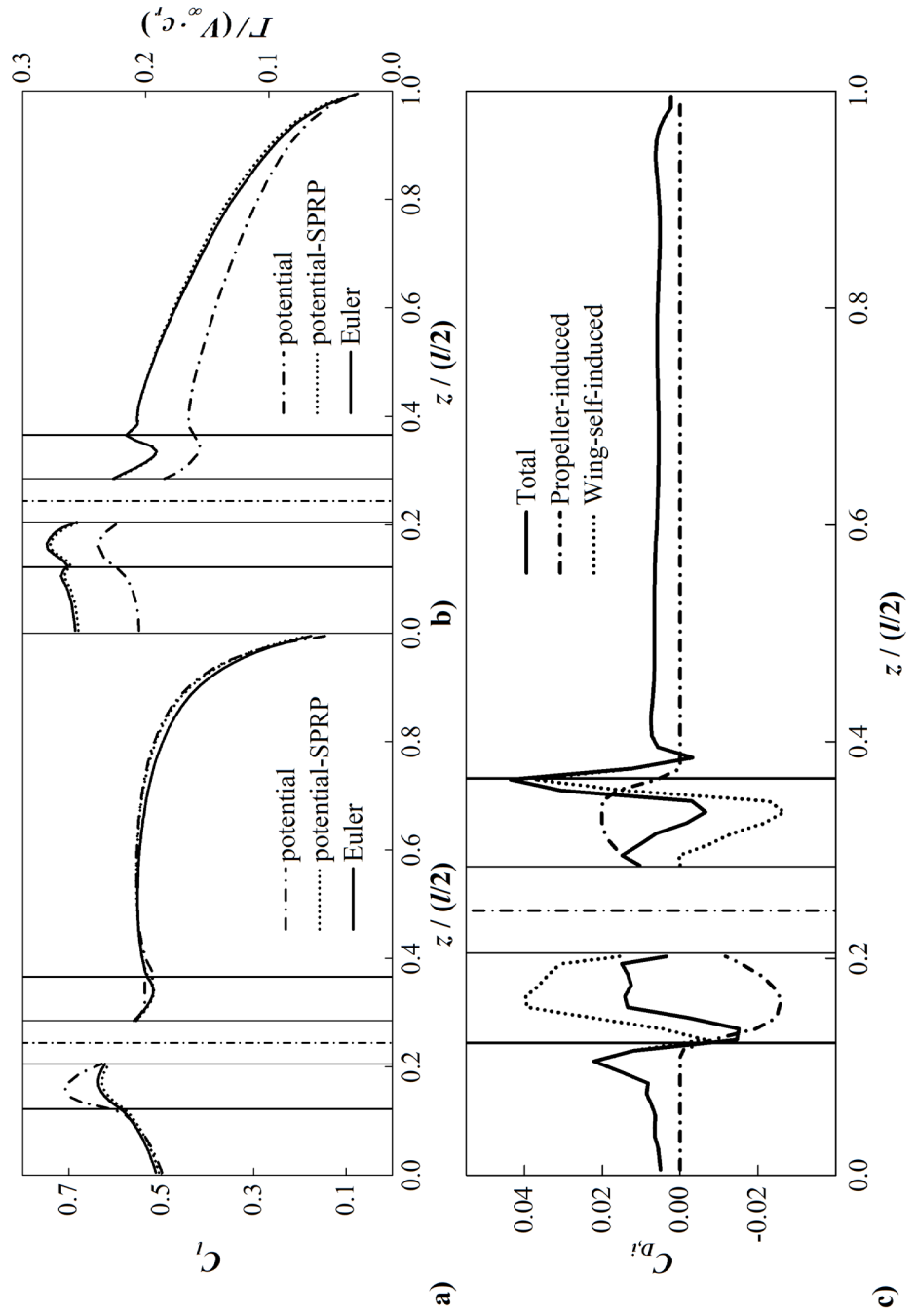

Figure 4.8 Depiction of a) lift distribution, b) circulation distribution, and c) induced drag distribution of the wing with optimum twist distribution

In terms of SRV arrangement, three aspects are considered to be paramount to the overall system performance: the axial and azimuthal positions of SRVs relative to the wing, and the blade count. The effect of the axial and azimuthal positions of SRVs is discussed in Sec. 4.4.1, and the effect of SRV blade count is investigated in Sec. 4.4.2.

4.4.1 Effect of axial and azimuthal positions of SRVs

4.4.1.1 Velocity and force diagrams of SRVs and wing

The wing with a positive lift induces upwash at the front and downwash at the back. The angular velocity generated by the propeller, when expressed in wing coordinate system, points upward on the blade-upgoing side and downward on the blade-downgoing side. Considering the installation position of SRVs, it can be either upstream or downstream of the wing in terms of axial position, and either on the blade-upgoing side or the downgoing side in terms of azimuthal position. Consequently, there are four different combinations of the induced velocities from the propeller and wing on the SRVs. For ease of study, the effect of axial and azimuthal positions of SRVs is investigated in this section by designing SRV with only one blade. Figure 4.9 illustrates the SRV-wing mutual induced velocity and force diagrams for these four different cases.

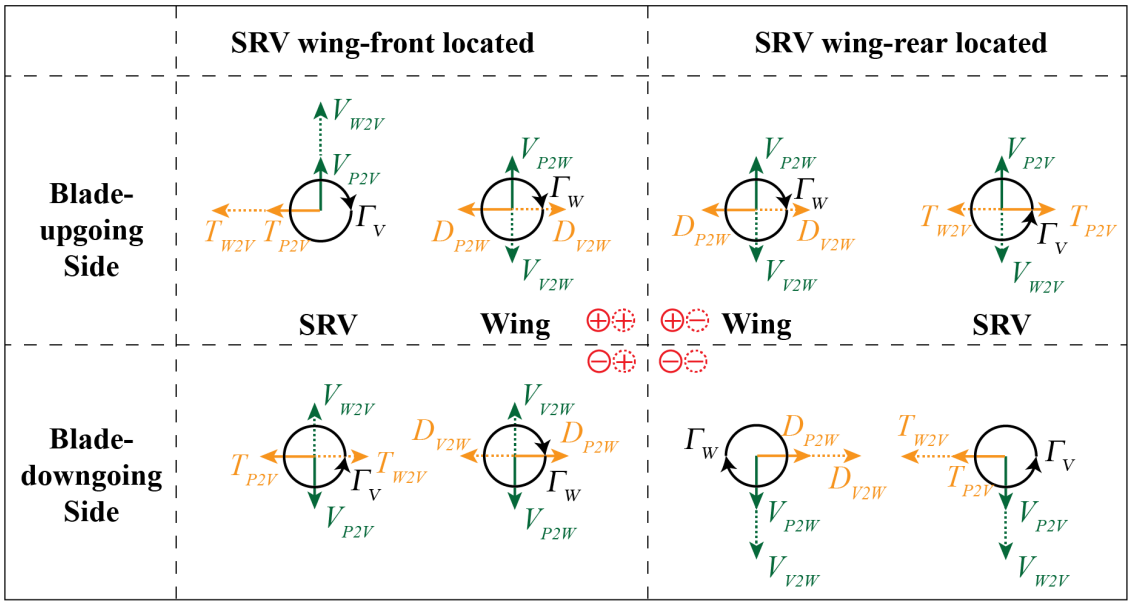

Figure 4.9 SRV-wing mutual induced velocity and force diagrams. In this scheme, the SRV-wing system is viewed from the side with the undisturbed flow coming in from the left. The index "A2B" refers to the force or velocity induced by A element on B element.

On the blade-upgoing side, the upward angular velocity induced by the propeller is augmented by the wing-induced upwash when SRVs are located upstream of the wing, and diminished by the downwash when SRVs are located downstream of the wing. From SRV thrust production point of view, it is more beneficial to locate SRVs upstream of wing where the resultant swirl velocity is larger compared to the downstream location. Besides positive thrust which is the axial component of the acting force, a positive lift is also generated which is the vertical component of the acting force. Conversely, on the blade-downgoing side, the downward angular velocity is decreased by the upwash upstream of wing, and enhanced by

the downwash downstream of the wing. More thrust will be generated if SRVs are positioned downstream of the wing compared to the upstream location. However, the lift force generated by the vanes is negative.

From the wing point of view, in all the four cases, the induced force on the wing by the SRVs always has the opposite direction to the induced force on the SRVs by the wing. This has a simple physical explanation when one notes that the swirl velocity in the propeller slipstream can either be recovered by the SRVs or the wing.

4.4.1.2 Performance of SRV and wing

The SRV design is performed at N = 1 for the four configurations discussed in Sec. 4.4.1.1 where the airfoil shape employs NACA 2412 as introduced in Sec. 4.2.2.1. The axial distance between the SRV stacking line and the wing quarter-chord line is one time propeller diameter when SRV is located upstream of the wing, and three quarters of the wing root chord length when SRV is located downstream of the wing.

The azimuthal position of the vane is optimized for the propulsive performance by the DIRECT algorithm as discussed in Sec. 4.2.4 (Eq. (4.17)). The overall layout of the propeller actuator disk, the wing and the optimum SRV design of the four cases is sketched in Figure 4.10.

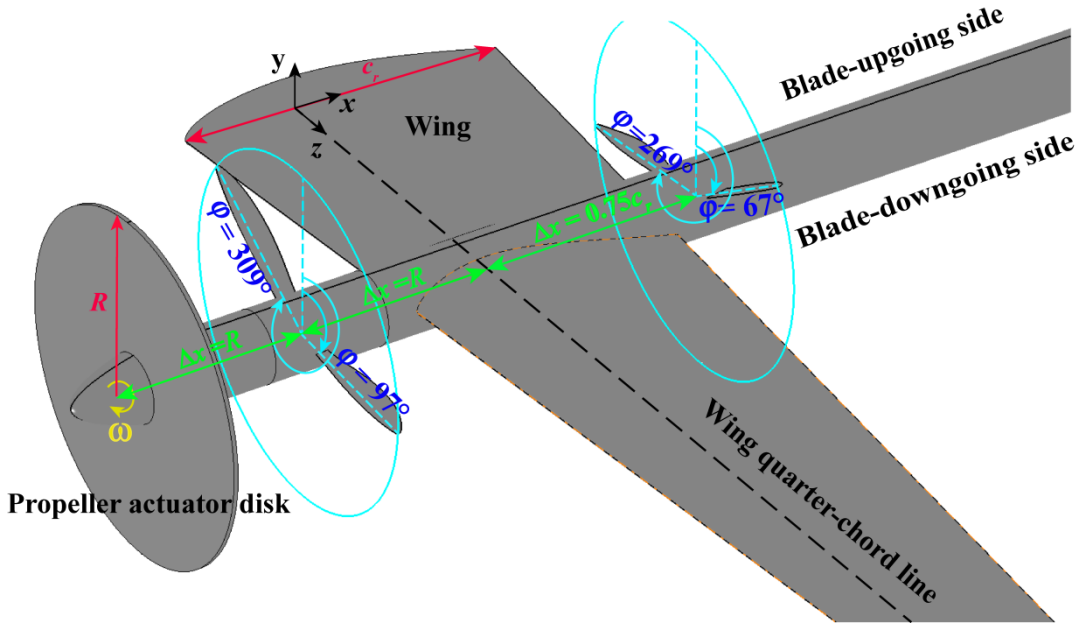

Figure 4.10 Sketch of the propeller actuator disk, the wing, and the optimum SRV design at N = 1 and four different installation positions.

The thrust coefficient of SRV $-T_{C,V}$ (negative value due to its opposite direction with the wing drag), the induced-drag coefficient of the wing $C_{D,i}$, and their summation are shown in Figure 4.11. As discussed previously, when the SRV is located upstream of the wing, it generates more thrust on the blade-upgoing side than the downgoing side. The calculation shows that the maximum thrust equals 10.8 counts at the vane position of φ = 309°. However, the induced drag of the wing has increased dramatically mainly due to two reasons. Firstly, as

can be seen from Figure 4.9, the SRV induces downwash and thus positive drag on the wing. The wake and tip vortices shed from the SRV is at a closer distance to the wing surface compared to the bound vorticity of SRV, hence they become dominant in generating downwash velocities on the wing. Secondly, even though the rolling up of the vane tip vortex is not simulated in the lifting line model, this phenomenon is captured well by the Euler simulation due to its inherent inviscid mechanism. Because of the rolling up of the vane tip vortex, the wing circulation exhibits an increase at the region close to the vane tip vortex. A local maximum is present in wing circulation distribution and consequently a local maximum in wing induced drag. Through the application of the multi-fidelity process, this effect is included in the induced-drag evaluation of the wing. These two effects get their maximum influence at a vane position of φ = 270° as can be observed in Figure 4.11(b). For the reason discussed above, the increased amount of wing induced drag is even higher than the thrust produced by the SRV. Thus in terms of drag reduction, it is detrimental to locate the SRV upstream of the wing.

When the SRV is located downstream of the wing, the angular velocity in propeller slipstream is enhanced by the wing-induced downwash on the blade-downgoing side. The SRV gets its maximum thrust coefficient of 9.1 counts at φ = 74° on this side. On the blade-upgoing side, a local maximum of $T_{C,V}$ is found when the SRV is located horizontally at φ = 270° where the wing-induced velocity gets its maximum. Since the wing is located upstream of SRV, both the wake and the tip vortices of the vane have limited effect on the wing loading distribution. There is a maximum change of 5.8 counts of wing-induced drag with different vane azimuthal positions. Besides thrust, the vane is also generating negative lift. In order to keep the total lift constant, the wing needs to provide more lift (by having a larger incidence angle) compared to the case without SRV, which leads to an increase of induced drag. The summation of $-T_{C,V}$ and $C_{D,i}$ gets its minimum value of 62.0 counts at vane position of φ = 67°. At this position, the vane is capable of providing thrust of 8.8 counts.

The system performance with SRV at four different installation locations is summarized in Table 4.2. One may conclude that it is preferable to locate SRV downstream of wing on the blade-downgoing side in terms of thrust production.

Table 4.2 Summary of the system performance with SRV at four different installation locations

SRV location	optimum φ	$-T_{C,V}$ [counts]	$C_{D,i}$ [counts]	$-T_{C,V}+C_{D,i}$ [counts]
Wing-front located on blade-upgoing side	309°	-10.8	86.1	75.3
Wing-front located on blade-downgoing side	97°	-0.5	81.1	80.6
Wing-rear located on blade-upgoing side	269°	-5.4	68.7	63.3
Wing-rear located on blade-downgoing side	67°	-8.8	70.8	62.0

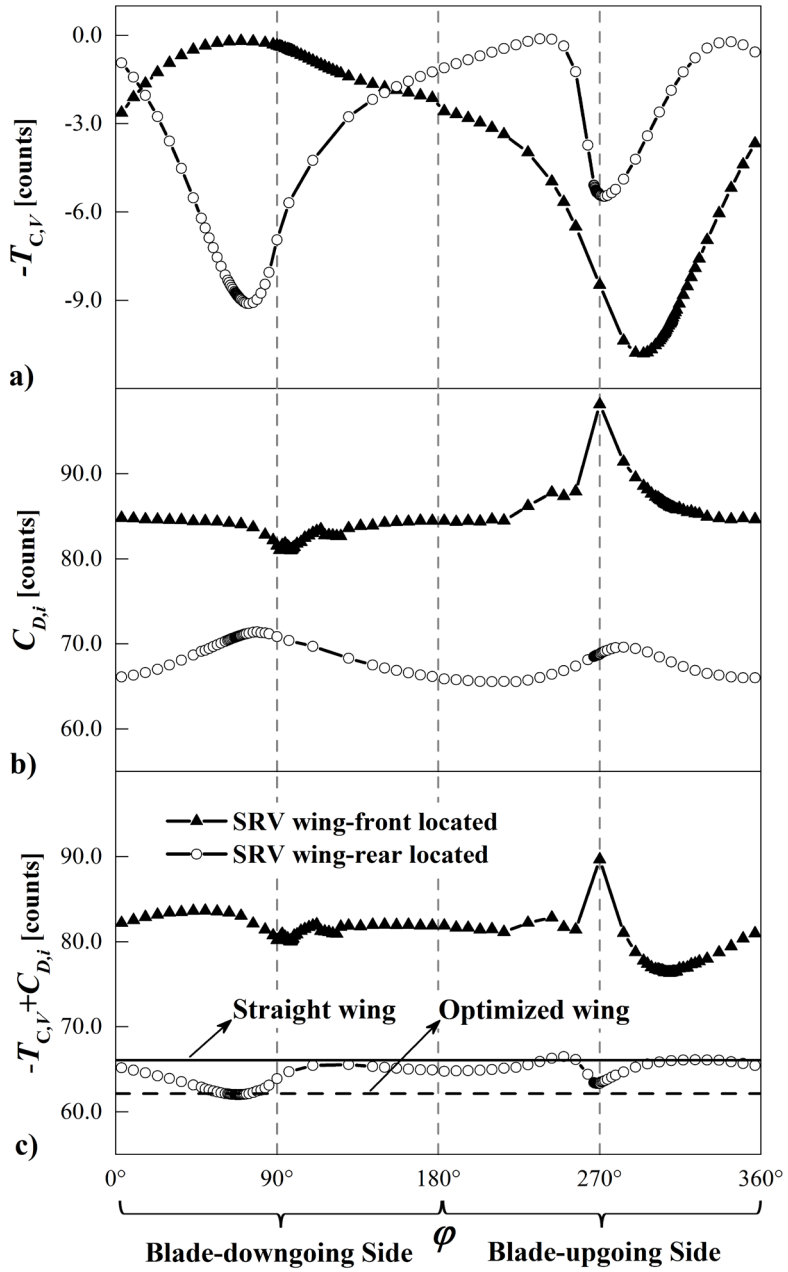

Figure 4.11 SRV and wing performance with respect to different axial and azimuthal positions of SRV relative to the wing at $N = 1$; a) SRV thrust coefficient $-T_{C,V}$; b) induced-drag coefficient of wing $C_{D,i}$; c) summation of $-T_{C,V}$ and $C_{D,i}$.

4.4.1.3 Effect of vane axial position at downstream of the wing

In the previous discussion, an optimum SRV location is identified where the vane is located on the blade-downgoing side downstream of the wing. The effect of the vane axial position relative to the wing is further investigated of this configuration at $N = 1$. The axial position of the wing is fixed (Figure 4.10). While, the axial distance between the SRV and the wing is increased based on the case discussed in the previous section (the axial separation between the SRV and the trailing edge of the local wing section at spanwise location of $z = 2R$ was $\Delta x = 0.35R$). The performance of the SRV and the wing is shown in Figure 4.12. When increasing their axial distance, the induced velocity from the wing on the vane decreases. With less enhancement of angular velocity by the wing, less thrust is generated by

the vane. Even though $C_{D,i}$ decreases with the increment of x, the system drag of the combination $-T_{C,V}+C_{D,i}$ increases. The overall performance gets its optimum when SRV is located closest to the wing.

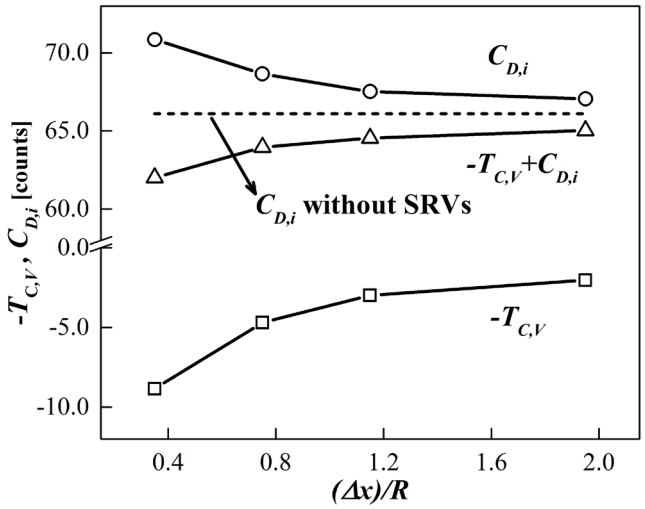

Figure 4.12 Performance of the SRV and the wing with respect to the axial position of the vane downstream of the wing. Δx denotes the axial separation between the SRV and the trailing edge of the local wing section at spanwise location of $z = 2R$.

4.4.2 Effect of blade count

In Chapter 3, it was found that the optimal number of SRVs with maximum thrust production for isolated propeller case is $N = 9$. In the previous section, it is demonstrated that it is preferable to locate SRVs on the blade-downgoing side downstream of the wing in the installed case. Even though there is a local optimum of system performance on the blade-upgoing side, the vane is located horizontally in the wake of the wing in this situation. This makes the local optimum questionable when taking viscous effects into account. Thus, the effect of blade count is investigated only on the blade-downgoing side with blade count up to 4.

The system performance is depicted in Figure 4.13. The induced drag of the wing again is correlated to the thrust of the SRVs due to the fact that the wing needs to compensate for the negative lift produced by the vanes. Thus, the induced drag coefficient of the wing increases with the increment of the blade count of the SRVs.

The thrust coefficient of SRVs designed for both isolated propeller (uninstalled case, denoted as Unins.) and installed propeller (denoted as Ins.) is characterized in Figure 4.13. In both cases, SRV thrust increases with the increment of blade count. However, the thrust provided by SRVs in the installed case is much larger than that of the uninstalled case (e.g. 8.8 counts compared to 2.7 counts at $N = 1$). This is due to the swirl velocity enhancement by the wing of the installed case. At the maximum blade count examined ($N = 4$), SRVs are capable of producing thrust of 12.2 counts in installed case, equivalent to 4.3% of propeller thrust. However, due to the increase of the wing induced drag, the summation of $-T_{C,V}$ and $C_{D,i}$ at $N = 4$, in the end, has decreased by 6.1 counts compared to the case without SRVs

(or equivalently, 2.1% of propeller thrust).

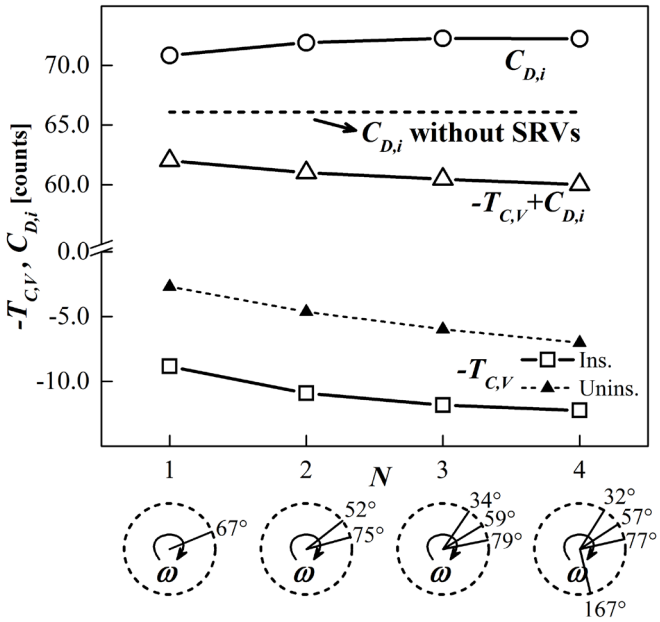

Figure 4.13 Performance of SRV and wing with respect to blade count.

4.5 Discussion of swirl recovery by the wing and the SRV

As illustrated in this chapter, the swirl recovery of the propeller slipstream can be achieved either by optimization of the wing loading distribution or by addition of SRV.

In the first way of optimization of the wing loading distribution, the swirl recovery leads to the induced-drag reduction of the wing with the constraint of constant wing lift. The wing loading is allocated more to the region where the lift-drag ratio is higher, which is the wing part immersed in the slipstream (Sec. 4.3.1). In the second way of addition of the SRV, the swirl recovery leads to the thrust enhancement from the vane with the constraint of constant total (wing + SRV) lift. Even after the wing loading is optimized, the addition of SRV can still provide thrust enhancement due to the fact that on the blade down-going side behind the wing, the angular momentum in the propeller slipstream is always enhanced by the wing-induced velocity. By recovering the (enhanced) angular momentum, the SRV has the ability of providing extra thrust without consuming any extra power. In conclusion, due to the different aerodynamic consequences (drag reduction of the wing compared with thrust enhancement from the SRV), the two ways of swirl recovery can be algebraically added up.

4.6 Conclusion

Design of swirl recovery system for propeller propulsion in a tractor configuration at cruise conditions is performed numerically. The swirl recovery can be achieved either by the trailing wing which leads to induced-drag reduction, or by introducing a set of SRVs in the slipstream which leads to extra thrust production. A design framework has been developed which consists of three modules corresponding to three components in this system, i.e. the analysis module of the isolated propeller, the SRV design module and the wing analysis

module. The framework features a multi-fidelity optimization procedure, where a potential flow-based solver is adopted as the low-fidelity method for fast convergence and Euler equations-based simulation is used as the high-fidelity method for verification purpose. The DIRECT optimization algorithm is utilized for global optimization, and the shape-preserving response prediction methodology is adopted as the model alignment technique between the low- and high-fidelity models.

A case study is carried out at the cruise condition of a typical turboprop aircraft, and two configurations are considered. In the first configuration, swirl recovery is achieved by the trailing wing, and the twist distribution of the wing is optimized. The Euler simulation of a tractor propeller-wing combination indicates that the slipstream impinging on the wing surface introduces local maxima and minima in wing circulation and subsequently induced-drag distribution not only inside but also at the edge of the slipstream. The low-fidelity potential flow-based method is not able to capture the multiple extrema in the wing circulation distribution, making the multi-fidelity optimization technique necessary for all the analyses performed in this chapter.

In the optimized wing configuration, the induced drag reduction is achieved by increasing the wing loading of the region where the lift-drag ratio is relatively higher, which is the region immersed in the slipstream. The twist angle is lowest at the tip to reduce the strength of wing tip vortex and thus tip losses. Compared to the baseline wing (untwisted), the induced drag has decreased by 3.9 counts out of 66.1 counts after optimization, corresponding to 1.4% of propeller thrust.

In the second configuration, a set of SRVs is introduced in the propeller slipstream. SRVs are designed with the constraint of constant total lift from SRVs and wing. Four different cases of SRV installation locations are identified based on different axial positions (upstream and downstream the wing) and azimuthal positions (blade-upgoing and downgoing side) relative to the wing. On the blade-downgoing side upstream of the wing and the blade-upgoing side downstream of the wing, the angular velocity in the slipstream is decreased by the wing induced velocity, while on the blade-upgoing side upstream of the wing and the blade-downgoing side downstream of the wing, the angular velocity is enhanced by the wing. From a thrust production point of view, it is beneficial to locate SRVs in regions where the angular velocity is enhanced. However, when SRVs are located upstream of the wing, the wake and tip vortices of the vane deteriorate the wing performance by increasing its induced drag. In such case, the thrust produced by the SRVs is counteracted by a larger drag increment on the wing. However, when the SRVs are located downstream of the wing, the circulation distribution of the wing is not disturbed much by SRVs, so as the induced drag. The best performance is found when the SRV is positioned on the blade-downgoing side downstream of the wing.

For the optimum configuration, a parameter study is performed in terms of the axial distance between SRV and wing. The system performance is found to be optimal when the SRV is located closest to the wing. At this position (where the SRV is three quarters of wing root chord length behind the wing quarter-chord line), a second parameter study is carried out in terms of blade count effect. In this particular case, the results have shown that SRVs are

capable of producing thrust of 12.2 counts at $N = 4$. However, besides thrust, negative lift is also generated by the vanes. In order to have constant total lift, the wing lift needs to be increased and consequently the induced drag. Taking this into account it is concluded that on constant lift and constant propeller thrust, compared to the case without SRVs, the equivalent drag of the system (the induced drag of the wing minus the thrust produce by the SRVs) has decreased by 6.1 counts, which is equivalent to 2.1% of propeller thrust.

It should be noted that, of all the analyses performed in this chapter, the effect of viscosity is neglected. It can be expected that part of the inviscid thrust of SRVs will be compensated by the viscous forces on the vanes when including viscosity effect. In order to figure out whether it is still beneficial for the propulsive performance when including SRVs, in the next chapter, the optimum configuration identified in this chapter is investigated in viscous flow condition.

Chapter 5 RANS Validation of the Swirl Recovery Vane for Installed Propeller Propulsion Systems

5.1 Introduction

In the previous chapter, an optimum configuration in terms of the overall system propulsive performance was identified where the SRVs are located behind the wing on the blade-downgoing side. The numerical investigations of the previous chapter, however, were performed with neglect of viscosity. This is considered to be acceptable since the main objective of the previous chapter was to explore the design space of the SRV while maintaining the computational efficiency. Moreover, due to the fact that the interference between the wing and the SRV is mainly inviscid, the conclusion is believed to be consistent with and without the inclusion of viscosity.

On the other hand, it can be expected that part (or even all) of the inviscid thrust of the SRVs will be compensated by the viscous drag exerted on the vanes. Thus, when introducing the viscous effect, it is unknown whether it is still beneficial in terms of propulsive performance to include SRVs. Therefore, an investigation is conducted in this chapter taking the effect of viscosity into account. This is done by designing and analyzing a new set of SRV on condition of viscous flow for the optimum configuration identified in the previous chapter (SRV on the blade down-going side downstream of the wing).

Due to the rotation motion of the propeller in the wing reference frame, the flowfield inside the slipstream features unsteadiness resulting from the periodic sweeping of the blade wake and tip vortices. With a tractor propeller, the performance of the downstream wing is dependent on the inflow conditions coming from the slipstream. Thus, the time-variation of the flow parameters in the slipstream results in the time-variation of the wing performance. The feature of such a time-dependent flowfield can be simulated, for example, by solving unsteady Reynolds-Averaged Navier Stokes (URANS) equations, which is capable of capturing both steady effects and large scale unsteadiness [107].

However, in spite of the time-variation of the wing performance, the steady simulation of the propeller-wing configuration by solving RANS equations was found to be representative of the time-averaged performance obtained from URANS simulation. For example, in Ref. [108], a tractor propeller together with a trailing wing was simulated by

solving RANS equations. The simulation result in terms of the wing performance as well as the pressure distribution on the wing surface was compared with those obtained from experiments. Good agreement was found between them. In another example, Williams [109] applied a frequency domain analysis to the unsteady aerodynamic coupling between a tractor propeller and a wing. The results of the unsteady analysis were compared with those obtained from the quasi-steady analysis and the experimental tests in terms of the time-averaged wing lift and drag. Good agreement was also found between all of them. Therefore, in this chapter, steady simulations are performed while neglecting the time-transient variation of the flowfield.

5.2 SRV design

The SRV design is performed in the same way with that introduced in Sec. 3.3.1. Firstly, the flowfield surrounding the tractor propeller and the trailing wing is established by solving the RANS equations with ANSYS® CFX solver, after which the velocity field on the SRV plane is subtracted. Secondly, the SRV planform is determined in two steps, where the optimal circulation distribution is calculated first, followed by an airfoil design routine.

The blade count of the SRV is set at N = 1 due to the reason presented below. As discussed previously in Sec. 3.3.2.1 (Figure 3.11), around 20% of the inviscid thrust provided by the SRVs is compensated by the viscous drag. It is assumed (and validated later in Sec. 5.3.4) that for the installed case, the percentage of the viscous drag with respect to the inviscid thrust of the SRV is no less than that of the uninstalled case. However, it can be observed from Figure 4.13 that the increase of the inviscid thrust of the SRVs when increasing the blade count (from 1 to 2, or even more) is always less than 20%. Thus, when introducing the viscous effect, the propulsive performance gets its optimum at blade count of N = 1. Therefore, the SRV design is performed at N = 1 as presented below.

5.2.1 RANS simulation of the propeller-wing configuration

The propeller and the wing geometries are kept the same with that used in the previous chapters (Figure 3.5 and Figure 4.5). The airframe is neglected such that the configuration is symmetry relative to the reflection plane (Figure 5.1). Thus, only half of the configuration is simulated by the RANS solver. The computational domain consists of a half cylinder with diameter of 10 times the wing span, extending 5 times the wing span upstream of the wing and 10 times the wing span downstream. The cylindrical block surrounding the propeller used in Sec. 3.3 is again used here. The boundary layers on the nacelle and the wing surface are resolved using 25 layers of hexahedron elements. In order to ensure an adequate resolution of the interaction between the propeller slipstream and the wing, smaller tetrahedral elements are arranged in a cylindrical region extending $3D_P$ downstream of the propeller. The rest of the computational domain (besides the propeller block and the hexahedron elements) is filled with unstructured mesh generated in ANSYS® ICEM.

The reflection plane is set as a free-slip wall boundary. A velocity inlet is specified, and the average static pressure of the outlet is prescribed to be equal to the undisturbed static

pressure. The SST turbulence model is adopted. The propeller block is specified as a rotational domain (with rotational frequency of n_s) which is solved in a rotating reference frame. On the interface between the rotational propeller block and the stationary wing block, the mixing plane method is used which performs a circumferential averaging of the fluxes through bands on the interface. Thus, it accounts for the time-averaged interaction effects while neglecting the transient interaction effects. The simulation is carried out at the same condition with that introduced in Sec. 4.2.1, which corresponds to an altitude of 5000 m, flight Mach number of 0.44, the propeller advance ratio of $J = 2.4$ and blade pitch angle of $\beta_{0.7R} = 50°$, and the wing lift coefficient of $C_{L,W} = 0.5$.

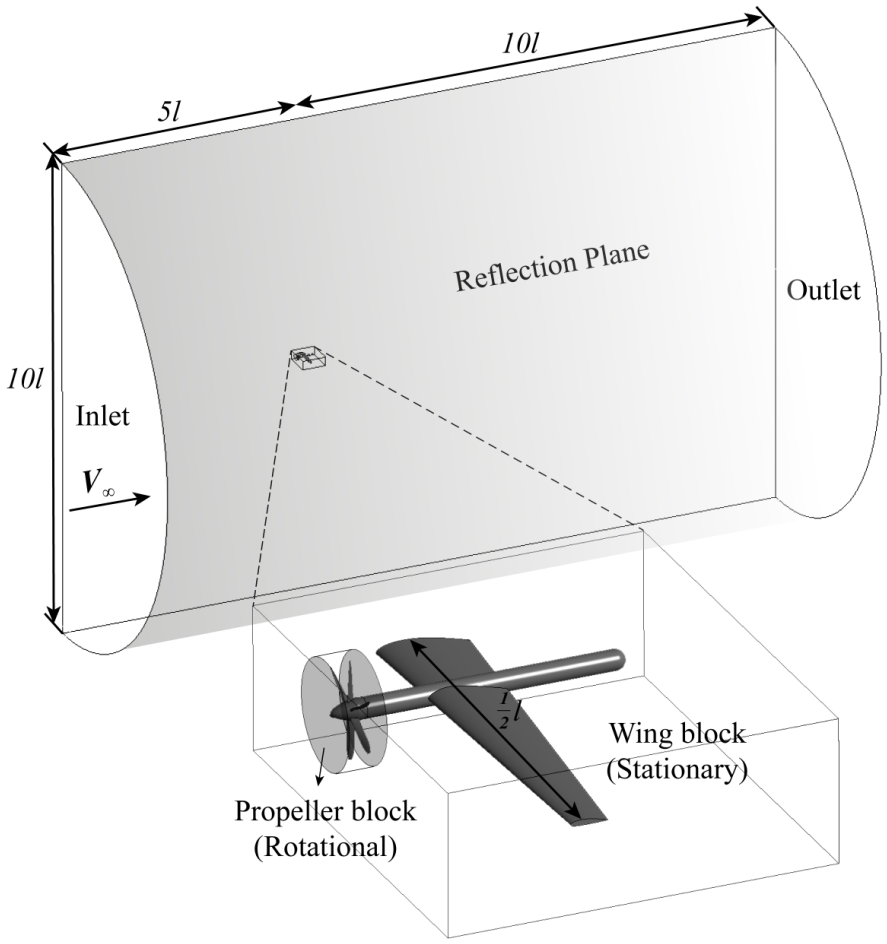

Figure 5.1 The computational domain of the propeller-wing configuration in the RANS simulation.

A grid refinement study was carried out on three meshes: coarse mesh (y^+ = 50, Z = 3.4 million), medium mesh (y^+ = 25, Z = 5.7 million) and fine mesh (y^+ = 12, Z = 14.0 million). The wing lift coefficient $C_{L,W}$ is plotted in Figure 5.2 with respect to the mesh size factor ($Z^{-2/3}$). As the mesh size reduces, the wing lift coefficient approaches an asymptotic value of $C_{L,W} = 0.5$. This value was obtained by applying Richardson's rule using the predictions of the medium and fine meshes, with a refinement ratio q = 2 and order of convergence b = 3.0.

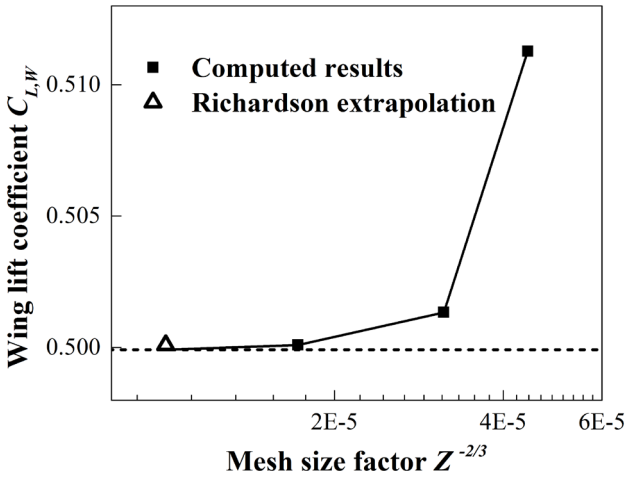

Figure 5.2 Mesh refinement study for the RANS simulation of the propeller-wing configuration at $J = 2.4$ and $\beta_{0.7R} = 50°$ showing the wing lift coefficient $C_{L,W}$ as function of the mesh size factor $Z^{-2/3}$.

It should be noted that despite of the same advance ratio of the propeller ($J = 2.4$) and the lift coefficient of the wing ($C_{L,W} = 0.5$), the thrust coefficient of the propeller predicted by the RANS simulation ($T_{C,P,RANS} = 0.0316$) is slightly different from that was predicted by the Euler equations ($T_{C,P,Euler} = 0.0294$). This is due to the fact that the propeller model used in the RANS simulation has full blade geometry, where the (time-averaged) interference from the downstream wing on the propeller performance is included. As a comparison, in the Euler simulation, the propeller model is represented by an actuator disk where the upstream effect of the wing on the propeller performance is excluded. However, since the goal is not to represent the cruise flight condition of the ATR 72 aircraft as close as possible but just to validate the performance of the SRV in viscous flow condition, the change in the propeller thrust is allowed.

As demonstrated in Sec. 4.4.1.3, in terms of the axial separation between the wing and the SRV, the system propulsive performance gets its optimum when the SRV is located closest to the wing, which was set at $\Delta x = 0.35R$. The new set of SRV is positioned at the same axial location as was done in the previous chapter. Since the SRV is located behind the propeller and the wing, when designing the SRV, the variations of both the propeller-induced and wing-induced velocities with and without addition of the SRV are neglected.

For determination of the azimuthal position of the SRV, the global optimization algorithm DIRECT is used as discussed in Sec. 4.2.4. When defining the swirl angle as:

$$\xi = \text{atan}(V_t / V_a) \tag{5.1}$$

the swirl angle is indicative of the angular momentum that can be recovered by the SRV, and thus the potential of thrust production from the SRV. The swirl angle on the SRV plane ($\Delta x = 0.35R$) obtained from the RANS simulation is plotted in Figure 5.3a. The optimum azimuthal position of the SRV obtained from optimization result is shown to be at $\varphi = 67.8°$ where the magnitude of ξ gets its maximum.

The radial distributions of the axial and circumferential velocities, as well as the swirl angle at $\varphi = 67.8°$, are presented in Figure 5.3b. The resultant velocities are combinations of the propeller-induced and wing-induced velocities. In the SRV plane, the wing-induced velocity contributes to both the axial and circumferential velocities. Thus, compared with the velocities behind the uninstalled propeller as shown in Figure 3.8, the radial positions of the maximum value of V_a and V_t are shifted towards larger radius due to the addition of wing-induced velocities. At the radial position of $r/R = 1$, V_t does not diminish to zero as in the case of isolated propeller, which is also a consequence of the disturbance by the wing-induced velocities. However, the radius of SRV is again set at the same value with that of the propeller.

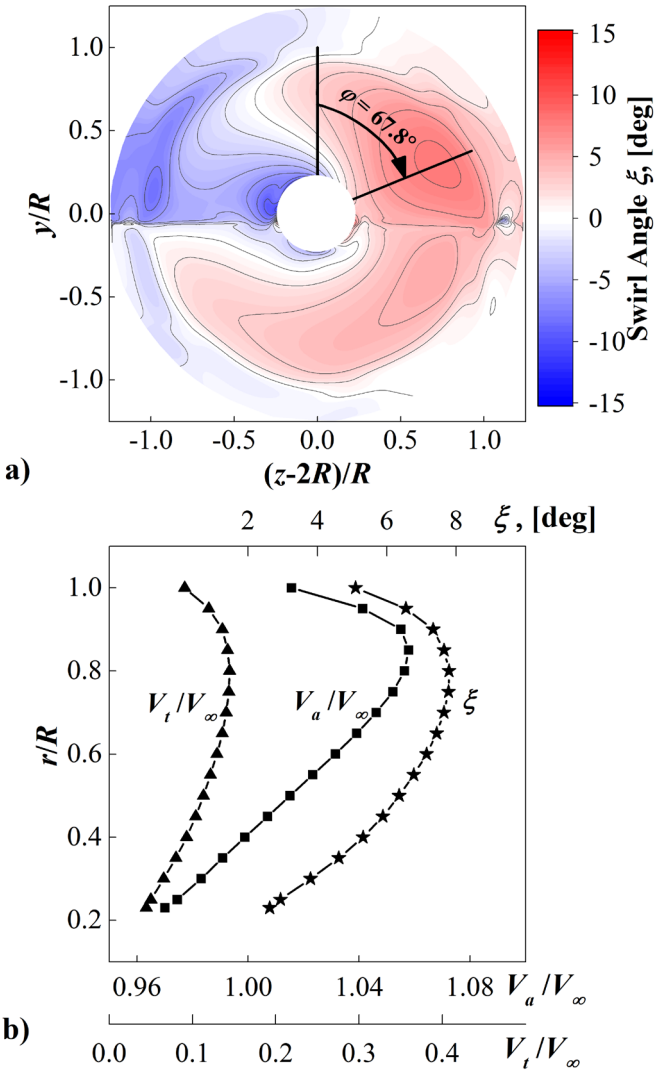

Figure 5.3 SRV design input obtained from the RANS simulation of the propeller-wing configuration at $J = 2.4$, $\beta_{0.7R} = 50°$ and $C_{L,W} = 0.5$: a) contour of the swirl angle in SRV plane (front view, the black line illustrates the maximum swirl-angle location $\varphi = 67.8°$); b) the radial distributions of the axial and tangential velocities and the swirl angle at $\varphi = 67.8°$.

5.2.2 SRV design with the velocity input

With the velocity input obtained from the RANS simulation (Figure 5.3), the SRV is designed at blade count of $N = 1$. Since no fairing is required for housing the instrumentation

as was done previously in Sec. 3.4, the hub radius of SRV is set at the same with that of the propeller (0.084 m). In the first step, the SRV circulation distribution is optimized based on the lifting line theory as discussed in Sec. 3.3.1.2. The blade is again discretized into 20 lifting segments, and the resulting optimum circulation distribution is shown on the left of Figure 5.4.

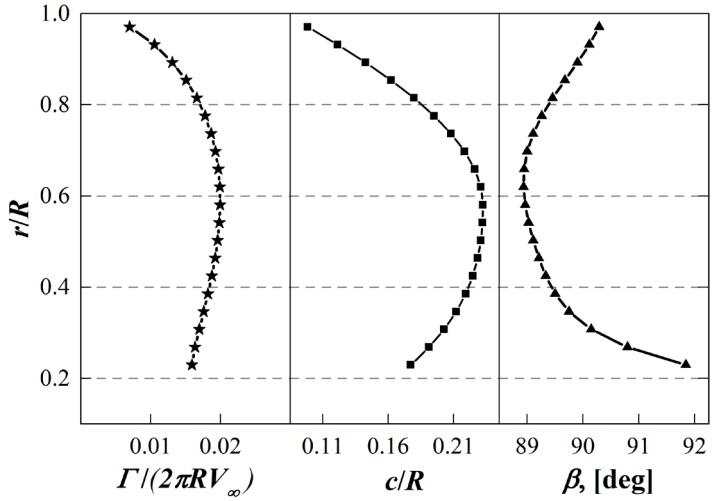

Figure 5.4 Radial distributions of the circulation, the chord length and the pitch angle of the SRV designed at $\Delta x = 0.35R$, $\varphi = 67.8°$ and $N = 1$.

In the second step, the airfoil design is performed at three representative sections: the root section ($r/R = 0.23$), the section with the maximum circulation ($r/R = 0.58$), and the tip section ($r/R = 0.97$). During the airfoil design process, it is found that the optimum value of the maximum camber, the chordwise position of the maximum camber, and the maximum thickness at all three sections exhibit similar values (less than 10% of difference) with those of the NACA-8405 airfoil. This is due to the relatively uniform distributions of both the circulation and the Reynolds number along the radius (compared with those of the SRVs designed for the isolated propeller, see Figure 3.13). Thus, the NACA-8405 airfoil is adopted at all radial sections, and only the chord length distribution is optimized with the method described in Sec. 3.3.1. The resulting optimum distributions of the chord length and the pitch angle are shown in the middle and on the right of Figure 5.4 respectively.

The overall performance of the SRV predicted by the lifting line theory is presented in Table 5.1. It should be noted that the performance coefficients shown here are all defined based on the freestream dynamic pressure and the wing area as in Eq. (4.3) and Eq. (4.16). Compared to the thrust generated by the propeller ($T_{C,P} = 0.0316$), the SRV provides 3.0% of the propeller thrust when the viscous drag is excluded ($T_{C,V,invis} = 9.4\times10^{-4}$ based on lifting line theory). The viscous drag of the SRV ($C_{D,V,vis} = 2.6\times10^{-4}$ based on 2D airfoil analysis), however, has compensated 28.6% of the inviscid thrust, leaving 2.1% of propeller thrust generated by the SRV. The percentage of the viscous drag with respect to the inviscid thrust is consistent with the assumption made in Sec. 5.2 that more than 20% of the inviscid thrust provided by the SRVs is compensated by the viscous drag. Thus, it is confirmed that the system gets its optimum performance when the blade count of the SRV is set at $N = 1$.

Since the SRV is located on the blade down-going side, the lift force of the SRV is negative ($C_{L,V} = -0.015$) which corresponds to 3% of the wing lift ($C_{L,W} = 0.5$). Thus, when the SRV is installed, the incidence angle of the wing needs to be increased to have the same overall lift of the wing-SRV combination.

Table 5.1 SRV performance predicted by the lifting line theory. All the non-dimensional parameters in this table are defined based on the freestream dynamic pressure and the wing area as in Eq. (4.3) and Eq. (4.16).

Variable	Value
$T_{C,V,invis}$ ($T_{C,P}$)	9.4×10^{-4} (0.0316)
$C_{D,V,vis}$	2.6×10^{-4}
$T_{C,V,invis} - C_{D,V,vis}$	6.7×10^{-4}
$C_{L,V}$ ($C_{L,W}$)	-0.015 (0.50)

5.3 RANS simulation of the propeller-wing-SRV configuration

5.3.1 Mesh topology

The geometries and the mesh topology of the propeller and the wing are kept the same as that used in Sec. 5.2.1. Another block surrounding the SRV is generated consisting of unstructured mesh (Figure 5.5). The resolution of the vane solid surface, the refinement of the wake and tip region of the vane are similar to that of the wing by scaling down the mesh size based on the chord length ratio of the SRV and the wing. The boundary layer is resolved using 25 layers of hexahedron elements generated from the vane surface.

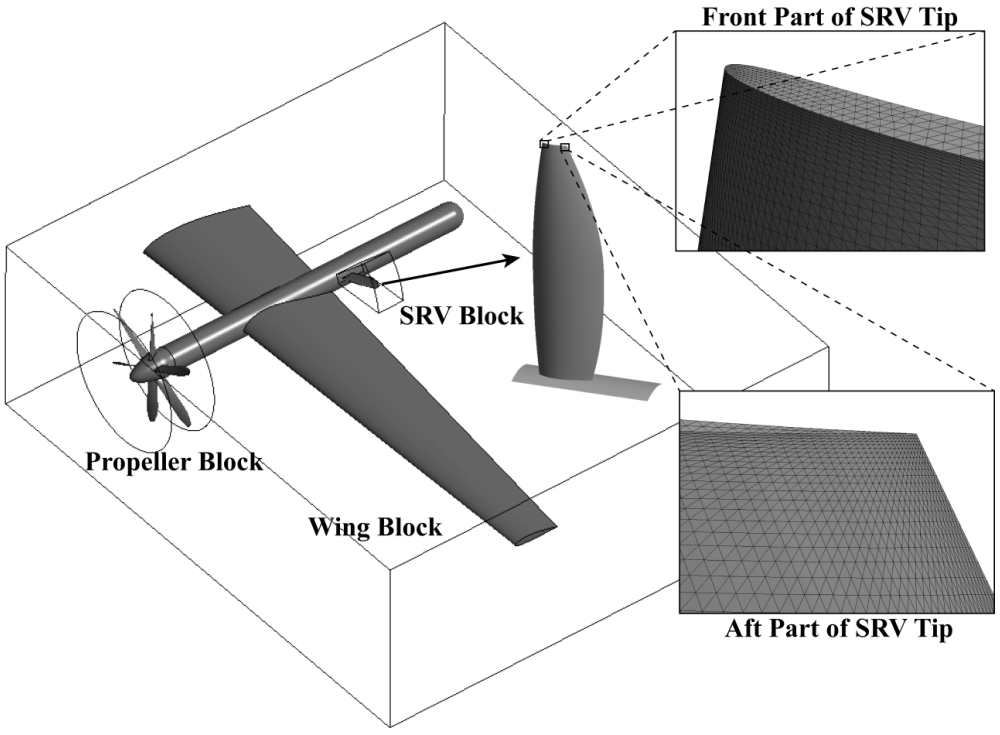

Figure 5.5 Mesh topology of the propeller-wing-SRV configuration and the resolution of the vane solid surface.

The boundary conditions, the turbulence model, and the interface between the rotational propeller block and the stationary wing block are set the same as those discussed in Sec. 5.2.1. As mentioned in the previous section, besides the positive thrust, a negative lift is also generated by the SRV. Thus, the wing incidence angle is adjusted from 3.2° (without SRV) to 3.4° (with SRV installed) in order to compensate for the negative lift generated by the SRV. The simulation is carried out at the same condition with that introduced in Sec. 4.2.1, which corresponds to an altitude of 5000 m, flight Mach number of 0.44, the propeller advance ratio of $J = 2.4$ and blade pitch angle of $\beta_{0.7R} = 50°$. The simulation is again performed with the finite volume-based solver ANSYS® CFX.

5.3.2 Overall propulsive and lifting performance of the system

The overall propulsive and lifting performance of the system with and without the installation of SRV is compared in Table 5.2. The total lift is kept the same after the installation of SRV. This is achieved by increasing the wing lift coefficient from 0.501 without SRV to 0.516 with SRV installed, in order to compensate for the negative lift generated by the SRV ($C_{L,V} = -0.015$). In terms of the propeller performance, due to the disturbance from the downstream wing and SRV, small variations are observed in the thrust coefficient and the efficiency of the propeller, whereas all the variations are less than 0.5%. This has confirmed the assumption made in Sec. 5.2.1 that the variation of the propeller-induced velocities after addition of the SRV is negligible.

Table 5.2 Comparison of the overall propulsive and lifting performance of the system with and without the installation of SRV based on RANS simulation and prediction by the lifting line theory (denoted as LLT). All the non-dimensional parameters in this table are defined based on the freestream dynamic pressure and the wing area as in Eq. (4.3) and Eq. (4.16).

Part	Variables	SRV off	SRV on	
			RANS	LLT
Propeller	$T_{C,P}$	0.0316	0.0317	–
	η_P	0.761	0.762	–
Wing	$C_{L,W}$	0.501	0.516	–
	$C_{D,W}$	0.0219	0.0220	–
SRV	$T_{C,V}$	–	6.4×10^{-4}	6.7×10^{-4}
	$C_{L,V}$	–	-0.015	-0.015
Total	$T_{C,P}+T_{C,V}$	0.0316	0.0323	–
	$C_{L,W}+C_{L,V}$	0.501	0.501	–

With regard to the performance of the SRV, a thrust coefficient of $T_{C,V,RANS} = 6.4\times10^{-4}$ is predicted by the RANS simulation (corresponds to 2.0% of propeller thrust), with only a small difference from that predicted by the lifting line theory ($T_{C,V,LLT} = 6.7\times10^{-4}$). However, out of the 2.0% extra thrust generated by the SRV, 0.4% is compensated by the increased drag of the wing ($C_{D,W}$), leaving the increase of the overall propulsive efficiency of 1.6% of

propeller thrust due to the installation of SRV.

5.3.3 Wing lift distribution

As discussed in Sec. 5.2.1, when designing the SRV, an assumption has been made that the variation of the wing-induced velocities after addition of the SRV is negligible. This is confirmed by the comparison of the wing lift distribution with and without the installation of the SRV as presented in Figure 5.6. The local lift coefficient of the wing C_l is defined based on the freestream dynamic pressure and the local wing area ΔS as in Eq. (4.18).

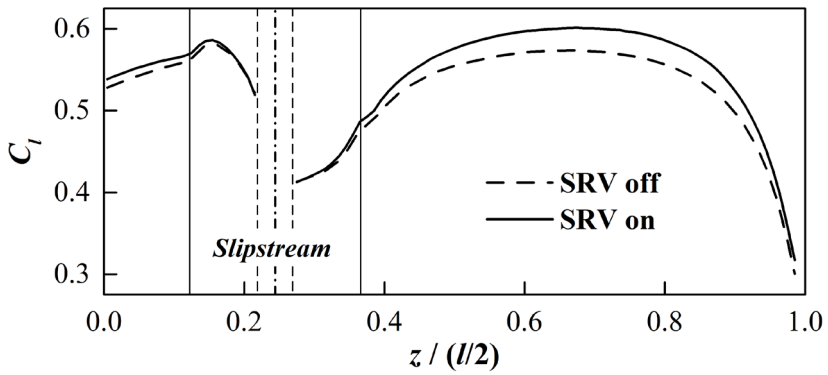

Figure 5.6 Comparison of the wing lift distribution with and without the installation of the SRV (based on RANS simulations).

Due to the increase of the wing incidence angle (from 3.2° without SRV to 3.4° with SRV installed), the wing lift with SRV installed is larger than that without SRV at all spanwise locations. However, the variation of C_l is smaller for the wing part immersed in the propeller slipstream compared to that outside of the slipstream. This is due to the fact that the performance of the wing inside the slipstream is dominated by the flowfield of the slipstream. Thus, the wing-induced velocities inside the slipstream would also exhibit smaller changes compared to the outside region. Therefore, the velocity input used for the SRV design, which is obtained from the simulation of the SRV-off configuration, is considered to be still valid when SRV is installed.

5.3.4 SRV loading distribution

The lift and circulation distributions of the SRV predicted by the lifting line theory are compared with those obtained from the RANS simulation as shown in Figure 5.7a. The local lift coefficient of the SRV ($C_{l,V}$) is defined based on the freestream dynamic pressure and the wing area as in Eq. (4.16). The circulation of a SRV section in the RANS simulation is obtained by integrating the velocity vectors along a rectangular which contains the SRV airfoil on the corresponding radial section. The circulation is then normalized by the freestream velocity multiplied by the vane radius. As can be observed from the figure, good agreement is observed in both the lift and the circulation distributions between the RANS simulation and the lifting line prediction.

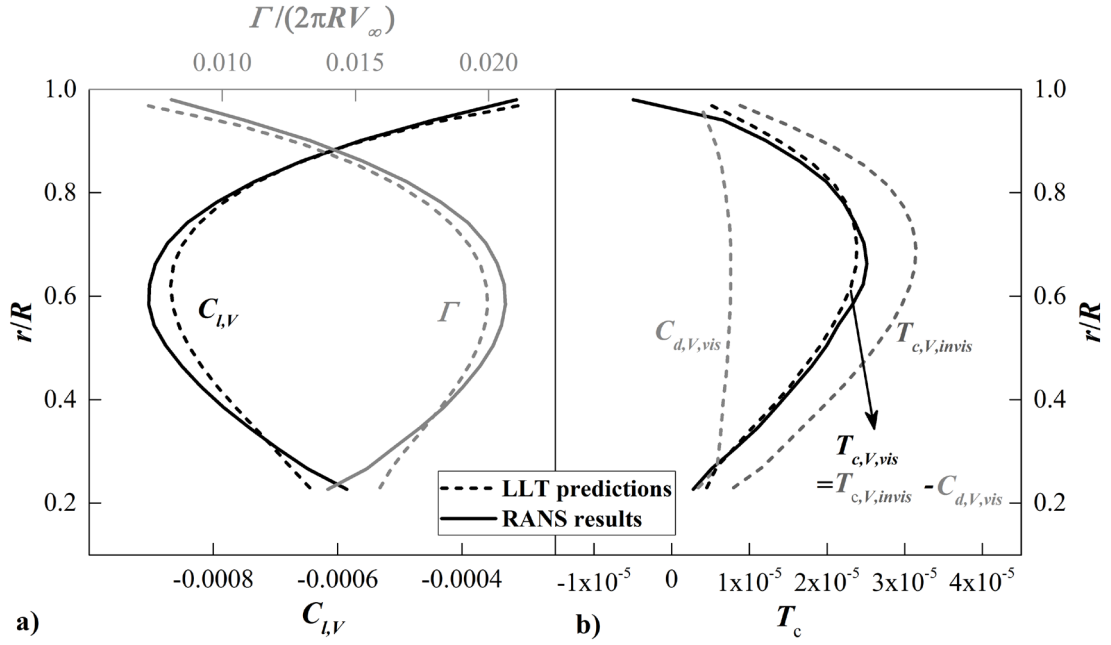

Figure 5.7 Comparison of the loading distribution of the SRV between the RANS simulation and the lifting line prediction in terms of: a) the circulation and the lift; b) the thrust.

The comparison of the thrust distribution of the SRV is illustrated in Figure 5.7b. The local thrust and drag coefficients of the SRV ($T_{c,V}$ and $C_{d,V}$) are defined based on the freestream dynamic pressure and the wing area as in Eq. (4.16). When designing the SRV with the lifting line theory, the optimum circulation distribution was first obtained (Figure 5.4), which gives the radial distribution of the inviscid thrust $T_{c,V,invis}(r)$ by virtue of the Kutta-Joukowski's theorem. Secondly, with the use of the airfoil of NACA-8405, the chord length distribution was optimized for the minimum penalty from viscous drag (Figure 5.4). Thus, the distribution of the viscous drag $C_{d,V,vis}(r)$ is calculated. Lastly, by subtracting the viscous drag form the inviscid thrust, the final thrust distribution of the SRV predicted by the lifting line theory is obtained by $T_{c,V,vis} = T_{c,V,invis} - C_{d,V,vis}$. As can be seen from Figure 5.7b, good agreement of the thrust distribution between the lifting line prediction and the RANS result is observed except at the blade tip region. The misalignment at the tip is probably due to the de-camber effect of the lifting line model which was discussed by Montgomery [110]. According to Montgomery [110], the velocity induced by the free vortex system of the wake will be higher at the trailing edge due to a closer distance than the leading edge. The aerodynamic consequence is that the induction from the free vortices is felt as a negative cambering of the airfoil, which tends to decrease the loading. The effect is felt everywhere on the blade but most significant at the tip. Thus, in the lifting line theory, the loading at the tip is overestimated when representing the blade by a lifting line instead of a surface, which is consistent with the observation from Figure 5.7b. It can be expected that by applying corrections for the de-camber effect, the lifting line theory would give better estimation of the blade loading at the tip region.

In this chapter, when evaluating the performance of the SRV, the effect of viscosity is taken into account. However, the numerical investigations are based on a scale-down model of a turboprop-powered airliner (Sec. 4.3) working at the flight condition of the full-scale

aircraft. This is done due to the reasons given below. Firstly, the wind-tunnel data of the scale-down propeller model is available, with which the validation of the numerical simulation of the propeller model can be made. Secondly, compared with the full-scale aircraft, the scale-down model exhibits a lower Reynolds number due to the reduced characteristic length. For an airfoil working at a lower Reynolds number, the lift-drag ratio is lower as a result of the larger boundary-layer thickness [111]. Thus, the propulsive performance of the scale-down SRV model discussed in this chapter indicates the lower boundary of SRV performance. For SRV implemented on full-scale aircraft, one would expect a smaller penalty of the viscous drag from the inviscid thrust provided by the SRV, or equivalently, a higher propulsive efficiency of the propulsion system.

5.4 Conclusion

In this chapter, the performance of the optimum SRV configuration (the SRV is located behind the wing on the blade down-going side) identified (with the help of inviscid analysis) in the previous chapter is validated in the case of viscous flow by means of RANS simulations.

A new set of SRV is designed at the same cruise condition of a typical turboprop aircraft ($J = 2.4$, $\beta_{0.7R} = 50°$ and $C_{L,W} = 0.5$). The design process established in Chapter 3 is used, which is based on the lifting line theory and an airfoil design routine. During the design process, the propeller-wing configuration is first simulated by solving RANS equations, after which the velocity distributions in the SRV plane is extracted and taken as design input. The optimum blade count is found at $N = 1$. The SRV is located at the azimuthal position where the angular momentum reaches the maximum ($\varphi = 67.78°$). At this position, an extra thrust of 2.1% of the propeller thrust is predicted by the lifting line theory, together with a negative lift equivalent to 3% of the wing lift.

This SRV design is subsequently validated by a RANS simulation. During the RANS simulation, the wing incidence angle is adjusted to compensate for the negative lift produced by the SRV. A thrust of 2.0% of the propeller thrust from the SRV is validated by the RANS simulation. Good agreement is observed in the lift, circulation, and thrust distributions of the SRV when comparing the lifting line prediction and the RANS result. However, due to the increase of the wing lift after addition of the SRV, out of the 2.0% extra thrust produced by the SRV, 0.4% is compensated by the increased drag of the wing, leaving overall propulsive benefit of 1.6% of propeller thrust.

Chapter 6 Conclusions and Recommendations

In this dissertation, the swirl recovery of the propeller propulsion system for both uninstalled and installed configurations is investigated numerically and experimentally. Focus is put on the research question of:

What is the principal mechanism of swirl recovery by means of SRVs and a trailing wing? What is the optimum layout for the best swirl-recovery (and subsequent thrust-enhancement) performance for tractor-propeller propulsion systems?

Evaluating isolated swirl recovery and that in combination with the wing, three sub-questions are formulated, of which the main conclusions are presented below.

6.1 Conclusions

6.1.1 Swirl recovery by SRV for the uninstalled propeller propulsion system

The first sub-question to be addressed regards the design and aerodynamic investigation of SRVs for the uninstalled propeller propulsion system:

For an uninstalled propeller propulsion system, what is the optimum SRV shape? What are the changes to the generalized propeller efficiency with addition of SRV?

In Chapter 3, the first research question is investigated. A universal explanation of swirl recovery mechanism is provided utilizing the lifting line theory. In principle, the swirl can be recovered by introducing aerodynamic elements which generate horseshoe vortices that have the opposite direction with those of the propeller.

In order to determine the optimum shape of the SRV, a hybrid framework is developed which is based on a lifting line model. The analysis method features a fast turnaround time, and is suitable for system level design and parameter studies. In the design framework, a variational approach is used where the partial derivatives of the objective function to the design variables is set to zero. With this design framework, the optimum SRV shape can be obtained without applying a dedicated optimization routine, thus reducing computational time.

As a test example, a set of SRVs was designed for a six-bladed propeller at a high

propeller loading condition ($C_{T,P} = 0.322$) with a Reynolds number of 5.90×10^4 relative to the blade chord length at 70% radial position and freestream velocity of 29 m/s. A parametric study was performed of the SRV performance as a function of the blade count and radius. It was found that the maximum SRV thrust could be obtained with a blade count of 9 and vane radius equal to that of the propeller. For this case, it was estimated that 4.1% of the propeller thrust could be produced by the SRVs.

To validate the design routine, an experiment was performed with a propeller and the SRVs in a low-speed open-jet wind tunnel. Due to the practical constraint, a blade count of 4 was chosen instead of the identified optimum of 9. At the design point, a thrust of 2.6% of the propeller thrust was measured from the SRVs, which is smaller compared to the prediction (3.4%) by the lifting-line method. The measured thrust of the SRVs diminished to 1.5% of the propeller thrust at a cruise condition of J = 1.0. However, since the SRVs provided thrust at all the measured propeller advance ratios ($J = 0.6-1.0$), and did not require any extra power input, the propulsive efficiency of the system (propeller + SRVs) improved accordingly for all flight phases considered.

6.1.2 Swirl recovery by the downstream wing for the installed propeller propulsion system

The second sub-question regards the swirl recovery of the installed propeller propulsion system by the downstream trailing wing:

For a wing-mounted tractor propeller configuration, what is the optimum wing shape for swirl-recovery purpose? What are the changes to the generalized propeller efficiency by wing shape optimization?

In Chapter 4, the second research question is investigated. In order to determine the optimum wing shape, a multi-fidelity optimization procedure is developed, where the low-fidelity method corresponds to the potential flow-based method, and the high-fidelity method is based on the analysis by solving Euler equations.

The Euler simulation of the propeller-wing configuration indicates that the slipstream impinging on the wing surface introduces local maxima and minima in the wing circulation not only inside but also at the edge of the slipstream. The low-fidelity potential flow-based method is not able to capture the multiple extrema in the wing circulation distribution, making the multi-fidelity optimization technique necessary for all the analyses performed for the installed configuration.

As a test case, the twist distribution of the wing is optimized at the cruise condition of a typical turboprop aircraft. Compared to the baseline wing (untwisted), the induced drag of the optimized wing has decreased by 3.9 counts out of 66.1 counts, corresponding to 1.4% of the propeller thrust. The induced-drag reduction is achieved by increasing the wing loading of the region where the lift-drag ratio is relatively higher, which is the region immersed in the slipstream. The twist angle is lowest at the tip to reduce the strength of wing tip vortex and

thus tip losses.

Since the swirl velocity generated by the propeller can be recovered only on the blade-upgoing side of the wing (and enhanced on the blade-downgoing side), the swirl recovery from the trailing wing is limited.

6.1.3 Swirl recovery by the SRVs for the installed propeller propulsion system

The third sub-question regards the swirl recovery of propeller propulsion system by introducing a set of SRVs in the slipstream:

For a wing-mounted tractor propeller configuration equipped with SRVs, what is the optimum layout of SRVs-wing combination for swirl-recovery purpose? What are the changes to the generalized propeller efficiency with addition of SRV?

The third research question is investigated in Chapter 4 and 5. In Chapter 4, the SRVs are designed with the multi-fidelity method (with assumption of inviscid flow) at the same cruise condition as that of the wing-shape optimization. Four different cases of SRVs installation positions are investigated with different axial and azimuthal positions relative to the wing. It was found that when the SRVs are located upstream of the wing, the wake and tip vortices of the vane deteriorate the wing performance by increasing its induced drag. In such cases, the thrust produced by the SRVs is counteracted by a larger drag increase from the wing. However, when the SRVs are located downstream of the wing, the circulation distribution of the wing is not disturbed much by the SRVs, so as the induced drag. In the end, an optimum configuration is identified where SRVs are positioned on the blade-downgoing side downstream of the wing.

For the identified optimum configuration, a parameter study is performed in terms of the axial distance between the SRV and the wing. The system performance is found to be optimal when the SRV is located closest to the wing. At blade count of 4, SRV is capable of producing 4.2% of propeller thrust. However, besides thrust, negative lift is also generated by the vanes. In order to have constant total lift, the lift of the wing increases and consequently the induced drag. In the end, compared to the case without SRVs, the drag of the system has decreased by 6.1 counts, which is equivalent to 2.1% of propeller thrust.

In Chapter 5, the SRV performance is validated taking the effect of viscosity into account. The propeller-wing configuration is first simulated by a RANS solver, after which the SRV is designed with the lifting line theory. Due to the addition of the viscous drag, the SRV gets its optimum performance at blade count of 1. An optimum azimuthal position of SRV in terms of thrust production is identified where the angular momentum in the SRV plane reaches the maximum.

The SRV design is subsequently validated by RANS simulation. During the RANS simulation, the wing incidence angle is adjusted to compensate for the negative lift produced by the SRV. A thrust of 2.0% of the propeller thrust from the SRV is validated by the RANS

simulation. Good agreement is observed in the lift, circulation, and thrust distributions of the SRV between the lifting line prediction and the RANS result. However, due to the increase of the wing lift after addition of the SRV, out of the 2.0% extra thrust produced by the SRV, 0.4% is compensated by the increased drag of the wing, leaving overall propulsive benefit of 1.6% of propeller thrust.

By addition of the SRV, the swirl recovery leads to the thrust enhancement from the vane with the constraint of constant total (wing + SRV) lift. It should be noted that even after the wing loading is optimized, the addition of SRV can still provide thrust enhancement due to the fact that on the blade down-going side behind the wing, the angular momentum in the propeller slipstream is always enhanced by the wing-induced velocity. By recovering the (enhanced) angular momentum, the SRV has the ability of providing extra thrust without consuming any extra power. Therefore, it can be concluded that due to the different aerodynamic consequences (drag reduction of the wing compared with thrust enhancement from the SRV), the two ways of swirl recovery can be algebraically added up.

6.2 Recommendations

6.2.1 Wing shape optimization

In Sec. 4.3, the wing shape is optimized in terms of the twist distribution. However, the optimization can also be performed on the chord distribution (as was done by Veldhuis [16]), the camber distribution, or any combination of them all. The unified mechanism of all the different optimizations is that the loading distribution of the wing is optimized, even though different wing shapes may have different other properties than the aerodynamic property (e.g. weight and ease of manufacturing).

6.2.2 SRV Design method

Even though a design framework of the SRV is developed and validated, additional improvement can be made of the design method as suggested below:

- Through this dissertation, the SRV design is performed with the utilization of the lifting line theory. As discussed in Sec. 5.3.4, in the lifting line theory, the loading at the tip is overestimated when representing the blade by a lifting line instead of a surface. This situation can be improved, for example, by applying corrections for the de-camber effect of the lifting line model, or applying a higher fidelity (potential-based) method such as the vortex lattice method or the panel method. In both cases, the chordwise loading of the vane is resolved either algebraically or physically.
- During the SRV design, a single point is chosen as the design condition. However, considering the multiple flight phases that a turboprop aircraft would experience, it is preferable to have a robust optimization of SRV taking into account different flight phases (or equivalently, different propeller blade loading conditions) in order to maximize the propulsive benefit from SRVs during the full flight cycle.

6.2.3 Multi-disciplinary design optimization of the SRV

In this dissertation, only the aerodynamic performance of the SRVs is considered while neglecting the weight penalty that comes along with the installation of the vanes. As can be expected, with the addition of SRVs and provision of extra thrust from them, either the maximum take-off weight (MTOW) can be increased with the same propeller propulsion system, or the propeller can be adjusted (to a different blade pitch angle without modification of propeller, or by designing a new propeller with a smaller radius, etc.) to maintain the constant MTOW. A quick estimation of the weight penalty is provided in Appendix B for the SRVs discussed in Chapter 3.

For SRVs located inside the propeller slipstream, the vane loading would exhibit strong unsteadiness due to the continuous and period sweeping of the blade wake and tip vortices. Extra noise would be generated from the vanes as a sequence of the time-transient interaction between propeller slipstream and SRVs. However, the tests performed by NASA indicated no extra noise by addition of SRV [37], while on the contrary, the experiments performed in DNW has shown an increased level of noise [41]. Further numerical and experimental studies should be performed in order to verify the noise production of SRVs both in uninstalled and installed configuration.

In conclusion, a multi-disciplinary design optimization is suggested in order to evaluate the overall performance benefit or impairment of the SRVs.

6.2.4 Application of SRV for "uninstalled" propeller propulsion system

The SRV design for uninstalled propeller propulsion system discussed in Chapter 3 is not restricted by the "uninstalled" condition. In fact, as long as the flow parameters on the SRV plane is approximately axisymmetry, such as the case where a pusher propeller is used at the rear of the wing or on the pylon (Figure 6.1), the design method developed and the conclusions drawn for the "uniform" SRV, where the vanes are uniformly distributed along the circumferential direction and exhibit identical loading, would still maintain.

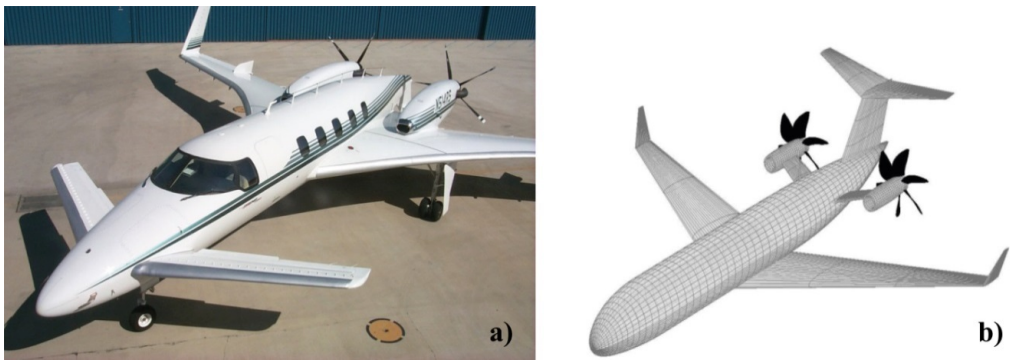

Figure 6.1 Examples of aircraft equipped with pusher propellers: a) the Beechcraft Starship NC-51, and b) layout of an aircraft equipped with pylon-mounted pusher propellers.
(Courtesy of Sinnige [112])

Appendix A Dimensional Analysis of Propeller Performance

In order to find out the key operational parameters that determine the aerodynamic performance for a given propeller, the dimensional analysis is performed. At the heart of dimensional analysis is the concept of similarity. Similarity refers to a transformation of variables that leads to a reduction in the number of non-dimensional governing parameters that specify the problem [113]. The non-dimensional governing parameters should form a complete set of basic building blocks for the system of derived quantities. The governing parameters used for the description of given propeller aerodynamics in the current context are listed in Table A.1 together with their units.

Table A.1 Governing parameters for description of propeller aerodynamics and their units

Governing parameters	**Unit**
propeller diameter, D_P	[m]
propeller rotation frequency, n_s	[1/s]
air density, ρ	[kg/m^3]
air kinematic viscosity, υ	[m^2/s]
air bulk elastic modulus, K	[N/m^2]
freestream velocity, V_∞	[m/s]
blade pitch angle at 70% radius, $\beta_{0.7R}$	[1]
propeller thrust, T_P	[N]
propeller torque, Q	[N·m]
propeller shaft power, P	[W]

The governing parameters listed in Table A.1 have three independent dimensions (i.e. mass [kg], length [m] and time [s]). Therefore, according to the Buckingham π theorem [114], there can be three independent parameters (e.g. D_P, n_s and ρ) out of the governing parameters, such that dimensions of the rest governing parameters can be expressed as products of powers of the dimensions of the three independent parameters as ($\beta_{0.7R}$ is already a non-dimensional parameter, thus neglected):

$$\begin{aligned}
[\upsilon] &= [D_P]^{a_1}\,[n_s]^{b_1}\,[\rho]^{c_1} \\
[K] &= [D_P]^{a_2}\,[n_s]^{b_2}\,[\rho]^{c_2} \\
[V_\infty] &= [D_P]^{a_3}\,[n_s]^{b_3}\,[\rho]^{c_3} \\
[T_P] &= [D_P]^{a_4}\,[n_s]^{b_4}\,[\rho]^{c_4} \\
[Q] &= [D_P]^{a_5}\,[n_s]^{b_5}\,[\rho]^{c_5} \\
[P] &= [D_P]^{a_6}\,[n_s]^{b_6}\,[\rho]^{c_6}
\end{aligned} \qquad \text{(A.1)}$$

Putting these equations in unit form results in:

$$\begin{aligned}
[\mathrm{m}^2\cdot\mathrm{s}^{-1}] &= [\mathrm{m}]^{a_1}\,[\mathrm{s}^{-1}]^{b_1}\,[\mathrm{kg}\cdot\mathrm{m}^{-3}]^{c_1}\\
\left[\mathrm{kg}\cdot\mathrm{m}^{-1}\cdot\mathrm{s}^{-2}\right] &= [\mathrm{m}]^{a_2}\,[\mathrm{s}^{-1}]^{b_2}\,[\mathrm{kg}\cdot\mathrm{m}^{-3}]^{c_2}\\
\left[\mathrm{m}\cdot\mathrm{s}^{-1}\right] &= [\mathrm{m}]^{a_3}\,[\mathrm{s}^{-1}]^{b_3}\,[\mathrm{kg}\cdot\mathrm{m}^{-3}]^{c_3}\\
[\mathrm{kg}\cdot\mathrm{m}\cdot\mathrm{s}^{-2}] &= [\mathrm{m}]^{a_4}\,[\mathrm{s}^{-1}]^{b_4}\,[\mathrm{kg}\cdot\mathrm{m}^{-3}]^{c_4}\\
[\mathrm{kg}\cdot\mathrm{m}^2\cdot\mathrm{s}^{-2}] &= [\mathrm{m}]^{a_5}\,[\mathrm{s}^{-1}]^{b_5}\,[\mathrm{kg}\cdot\mathrm{m}^{-3}]^{c_5}\\
[\mathrm{kg}\cdot\mathrm{m}^2\cdot\mathrm{s}^{-3}] &= [\mathrm{m}]^{a_6}\,[\mathrm{s}^{-1}]^{b_6}\,[\mathrm{kg}\cdot\mathrm{m}^{-3}]^{c_6}
\end{aligned} \tag{A.2}$$

Dimensional consistency requires that two sides of the equation have the same unit, i.e.:

$$\begin{array}{lll}
[\mathrm{m}]: & [\mathrm{s}]: & [\mathrm{kg}]:.\\
2 = a_1 - 3c_1 & -1 = -b_1 & 0 = c_1\\
-1 = a_2 - 3c_2 & -2 = -b_2 & 1 = c_2\\
1 = a_3 - 3c_3 & -1 = -b_3 & 0 = c_3\\
1 = a_4 - 3c_4 & -2 = -b_4 & 1 = c_4\\
2 = a_5 - 3c_5 & -2 = -b_5 & 1 = c_5\\
2 = a_6 - 3c_6 & -3 = -b_6 & 1 = c_6
\end{array} \tag{A.3}$$

Thus,

$$\begin{array}{lll}
a_1 = 2 & b_1 = 1 & c_1 = 0\\
a_2 = 2 & b_2 = 2 & c_2 = 1\\
a_3 = 1 & b_3 = 1 & c_3 = 0\\
a_4 = 4 & b_4 = 2 & c_4 = 1\\
a_5 = 5 & b_5 = 2 & c_5 = 1\\
a_6 = 5 & b_6 = 3 & c_6 = 1
\end{array} \tag{A.4}$$

Non-dimensional parameters are introduced as follows:

$$\begin{aligned}
\Pi_1 &= \frac{\upsilon}{{D_P}^{a_1} {n_s}^{b_1} \rho^{c_1}} = \frac{\upsilon}{{D_P}^2 {n_s}^1}\\
\Pi_2 &= \frac{K}{{D_P}^{a_2} {n_s}^{b_2} \rho^{c_2}} = \frac{K}{{D_P}^2 {n_s}^2 \rho^1}\\
\Pi_3 &= \frac{V_\infty}{{D_P}^{a_3} {n_s}^{b_3} \rho^{c_3}} = \frac{V_\infty}{D_P n_s}\\
\Pi_4 &= \frac{T_P}{{D_P}^{a_4} {n_s}^{b_4} \rho^{c_4}} = \frac{T_P}{{D_P}^4 {n_s}^2 \rho}\\
\Pi_5 &= \frac{Q}{{D_P}^{a_5} {n_s}^{b_5} \rho^{c_5}} = \frac{Q}{{D_P}^5 {n_s}^2 \rho}\\
\Pi_6 &= \frac{P}{{D_P}^{a_6} {n_s}^{b_6} \rho^{c_6}} = \frac{P}{{D_P}^5 {n_s}^3 \rho}
\end{aligned} \tag{A.5}$$

Since $(D_P \cdot n_s)$ is proportional to the tip speed of the propeller, Π_1 is inversely proportional to the Reynolds number based on the propeller tip speed and diameter ($\Pi_1 = \frac{1}{Re_{tip}} = \frac{\upsilon}{(D_P n_s) \cdot D_P}$). With the speed of sound determined by $a_{SoS}^2 = K/\rho$, Π_2 is inversely proportional to the square of the tip Mach number ($\Pi_2 = \frac{1}{Ma_{tip}^2} = \left(\frac{a_{SoS}}{D_P n_s} \right)^2$). Π_3 is the propeller tip speed non-dimensionalized by the freestream velocity, which is called the propeller advance ratio ($\Pi_3 = J = \frac{V_\infty}{n_s D_P}$). Π_4 , Π_5 and Π_6 are called propeller thrust coefficient $\Pi_4 = C_{T,P} = \frac{T_P}{\rho n_s^{\,2} D_P^{\,4}}$, torque coefficient $\Pi_5 = C_Q = \frac{Q}{\rho n_s^{\,2} D_P^{\,5}}$ and power coefficient $\Pi_6 = C_P = \frac{P}{\rho n_s^{\,3} D_P^{\,5}}$ respectively. The propeller efficiency is defined by the ratio of the propulsive power over the shaft power as:

$$\eta_P = \frac{T_P V_\infty}{P} = \frac{T_P V_\infty}{Q\omega} = \frac{J \cdot C_{T,P}}{2\pi C_Q} = \frac{J \cdot C_{T,P}}{C_P} \tag{A.6}$$

Therefore, the propeller performance is typically represented by the thrust coefficient $C_{T,P}$, the torque coefficient C_Q , the power coefficient C_P , and the efficiency η_P as a function of the advance ratio J and the blade pitch angle $\beta_{0.7R}$ at the operating Reynolds number Re_{tip} and Mach number Ma_{tip} .

Appendix B SRV Weight Penalty Estimation

With addition of SRVs, the weight of the aircraft increases, so does the total drag of the aircraft at a given flight speed. Consequently, part of the thrust produced by the SRVs needs to counteract the increased drag imposed by their own weight. This part of thrust is estimated as follows.

The drag coefficient of the aircraft can be expressed in terms of the lift coefficient as:

$$C_D = C_{D,0} + \frac{C_L^2}{\pi A e} \tag{B.1}$$

where $C_{D,0}$ is the zero-lift drag coefficient, A is the wing aspect ratio and e is the Oswald efficiency factor. Using representative values of $C_{D,0} = 0.02$, $e = 0.82$ from Torenbeek [115] for large turboprop aircraft, the aspect ratio of ATR 72 aircraft $A = 12$ [116], and $C_L = 0.5$ at cruise, the total drag coefficient is estimated to be $C_D = 0.0281$. With the addition of SRVs, the total weight increases so that the lift coefficient should increase accordingly (assuming constant wing area). Since there is no information about the weight estimation of SRVs, as a first guess, the weight of SRVs is assumed to be the same with that of the propeller blades, which is $m_{SRV} = m_{prop} = 165\ \text{kg}$ for ATR 72 [116]. Thus, the estimated increase of the lift coefficient is:

$$\Delta C_L = \frac{N_{engine} m_{SRV}}{m_{MTO}} C_L = \frac{2 * 165\ \text{kg}}{22800\ \text{kg}} * 0.5 = 0.0072 \tag{B.2}$$

The corresponding relative increase of the drag coefficient due to the weight penalty is:

$$\frac{\Delta C_D}{C_D} = \frac{\frac{1}{\pi A e}[(C_L + \Delta C_L)^2 - C_L^2]}{C_D} = 0.083\% \tag{B.3}$$

As can be seen from the above analysis, the drag increase due to the weight penalty of SRVs is one order of magnitude smaller than the thrust produced by the SRVs. However, in the above analysis, it is assumed that the maximum take-off weight is kept the same with addition of SRVs. This should not be the case since less fuel is required with extra thrust provided by SRVs, and consequently the maximum take-off weight could potentially be smaller with addition of SRVs. Ideally, the maximum take-off weight should be estimated based on the new propulsion system thrust of propeller-SRVs combination. Besides, the zero-lift drag $C_{D,0}$ consists of the majority of the total drag (around 70%), thus it has a great

influence on the estimation of the weight penalty. However, this data is not available in the open literature. In conclusion, in the estimation presented above, the uncertainty is unknown, and it only gives an idea of the order of the magnitude of weight penalty.

Bibliography

1. Froude, W., "On the Elementary Relation between Pitch, Slip and Propulsive Efficiency," NASA-TM-X-61726, 1920.

2. Drzewiecki, S., "Méthode Pour la Détermination des éléments Mécaniques des Propulseurs Hélicoïdaux," *Bulletin de L'Association Technique Maritime*, Vol. 3, No. 3, 1892.

3. Miley, S. J., Ash, R. L., Hyde, K. W., Landman, D., and Sparks, A. K., "Propeller Performance Tests of Wright Brothers "Bent-End" Propellers," *Journal of Aircraft*, Vol. 39, No. 2, 2002, pp. 234-241.

4. Padfield, G. D., and Lawrence, B., "The Birth of Flight Control: An Engineering Analysis of the Wright Brothers' 1902 Glider," *The Aeronautical Journal*, Vol. 107, No. 1078, 2003, pp. 697-718.

5. Betz, A., and Prandtl, L., "Schraubenpropeller mit Geringstem Energieverlust," *Göttinger Nachrichten*, Vol. 1919, 1919, pp. 193–217.

6. Goldstein, S., "On the Vortex Theory of Screw Propellers," *Proceedings of the Royal Society of London, Series A: Mathematical, Physical and Engineering Sciences*, Vol. 123, No. 792, 1929, pp. 440–465.

7. Hartman, E. P., and Biermann, D., "The Aerodynamic Characteristics of Full-scale Propellers Having 2, 3, and 4 Blades of Clark Y and R.A.F. 6 Airfoil Sections," NACA TR-640, 1938.

8. Lindsey, W. F., Stevenson, D. B., and Daley, B. N., "Aerodynamic Characteristics of 24 NACA 16-series Airfoils at Mach Numbers Between 0.3 and 0.8," NACA TN-1546, 1947.

9. Mikkelson, D. C., Mitchell, G. A., and Bober, L. J., "Summary of Recent NASA Propeller Research," *AGARD Fluid Dynamics Meeting on Aerodynamics and Acoustic of Propellers*, Toronto, Canada, 1984.

10. Mcmahon, T., "Oil Prices in Inflation Adjusted Terms," URL: https://inflationdata.com/Inflation/Inflation_Rate/Historical_Oil_Prices_Chart.asp.

11. Spencer, F. A., "Aircraft Selection," *AIAA Conference on Air Transportation: Technical Perspectives and Forecasts*, AIAA Paper 1978-1531, August, 1978.

12. Swihart, J. M., and Minnick, J. I., "Operations and Economics of U.S. Air Transportation," *AIAA Conference on Air Transportation: Technical Perspectives and Forecasts*, AIAA Paper 1978-1545, August, 1978.

13. Whitlow, J. B. Jr., and Sievers, G. K., "Fuel Savings Potential of the NASA Advanced Turboprop Program," NASA TM-83736, 1984.

14. Dugan, J. F., Gatzen, B. S., and Adamson, W. M., "Prop-Fan Propulsion-Its Status and Potential," SAE Technical Paper, No. 780995, 1978.

15. Jeracki, R. J., Mikkelson, D. C., and Blaha, B. J., "Wind Tunnel Performance of Four Energy Efficient Propellers Designed for Mach 0.8 Cruise," SAE Technical Paper, No. 790573, 1979.

16. Veldhuis, L. L. M., "Propeller Wing Aerodynamic Interference," Ph.D. Dissertation, Department of Aerospace Engineering, Delft University of Technology, Delft, the Netherlands, 2005.

17. L. Lombardi, "ATR, Program Review and Market Outlook," *10th EWADE Conference*, Naples, May, 2011.

18. ATR, "Connecting the Future, Turboprop Market Forecast 2018-2037," URL: http://www.atraircraft.com/datas/download_center/151/1011_makretforecast_digital_151.pdf

19. Bombardier Aerospace, "Market Forecast 2017-2036," URL: https://ir.bombardier.com/var/data/gallery/document/01/87/55/05/15/BCA-2017-2036-Market-Forecast-EN.pdf.

20. ATR Marketing Department, "Regional Market Outlook, Turboprop Perspective 2010-2029," URL: http://www.atraircraft.com/media/downloads/Regional%20Market%20Outlook%202010-2029.pdf.

21. RUAG, "World Air Forces 2015," URL: www.flightglobal.com/insight.

22. Veldhuis, L., Stokkermans, T., Sinnige, T., and Eitelberg, G., "Analysis of Swirl Recovery Vanes for Increased Propulsive Efficiency in Tractor Propeller Aircraft," *30th Congress of the International Council of the Aeronautical Sciences*, 2016.

23. Kroo, I., "Propeller-Wing Integration for Minimum Induced Loss," *Journal of Aircraft*, Vol. 23, No. 7, 1986, pp. 561-565.

24. Hager, R. D., and Vrabel, D., "Advanced Turboprop Project," NASA-SP-495, 1988.

25. Dominy, J., and Midgley, R. A., "A Transmission for the Contra-rotating Prop-fan Powerplant," *AIAA/SAE/ASME 20th Joint Propulsion Conference*, AIAA Paper 1984-1196, June, 1984.

26. Godston, J., and Mike, F. J., "Evaluation of Single and Counter Rotation Gearboxes for Propulsion Systems", *AIAA/SAE/ASME 20th Joint Propulsion Conference*, AIAA Paper 1984-1195, June, 1984.

27. Stürmer, A., Marquez Gutierrez, C. O., Roosenboom, E. W. M., Schröder, A., Geisler, R., Pallek, D., Agocs, J., and Neitzke K.-P., "Experimental and Numerical Investigation of a Contra Rotating Open-Rotor Flowfield," *Journal of Aircraft*, Vol. 49, No. 6, 2012, pp. 1868-1877.

28. Blandeau, V. P., and Joseph, P. F., "Broadband Noise due to Rotor-Wake/Rotor Interaction in Contra-rotating Open Rotors," *AIAA Journal*, Vol. 48, No. 11, 2010, pp. 2674-2686.

29. Akkermans, R. A. D., Stürmer, A., and Delfs, J. W., "Active Flow Control for Interaction Noise Reduction of Contra-rotating Open Rotors," *AIAA Journal*, Vol. 54, No. 4, 2016, pp. 1413-1423.

30. English Russia, "Antonov An 70," URL: http://englishrussia.com/2013/07/07/antonov-an-70/.

31. Kawakita, C., Takashima, R., and Sato, K., "CFD on Cavitation around Marine Propellers with Energy-saving Devices," *Mitsubishi Heavy Industries Technical Review*, Vol. 49, No. 1, 2012, pp. 63-67.

32. Saettone, S., Regener, P. B., and Andersen, P., "Pre-swirl Stator and Propeller Design for Varying Operating Conditions." *Proceedings of the 13th International Symposium on PRActical Design of Ships and Other Floating Structures*, September, 2016.

33. Zondervan, G. J., Holtrop, J., Windt, J., and Terwisga, T., "On the Design and Analysis of Pre-swirl Stators for Single and Twin Screw Ships," *Second International Symposium on Marine Propellers,* June, 2011.

34. Sedat, R. D., Purcell, E. S., and Hervey, C. L., "Full-Scale Trials of Pre-Swirl Vanes and Modified Propellers on a 41 Ft. Utility Boat," No. USCG-D-03-89, U.S. Coast Guard Research and Development Center, August, 1988.

35. Miller, C. J., "Euler Analysis of a Swirl Recovery Vane Design for Use with an Advanced Single-Rotation Propfan," *AIAA/SAE/ASME/ASEE 24th Joint Propulsion Conference*, AIAA Paper 1988-3152, July, 1988.

36. Gazzaniga, J. A., and Rose, G. E., "Wind Tunnel Performance Results of Swirl Recovery Vanes as Tested with an Advanced High Speed Propeller," *AIAA/SAE/ASME/ASEE 28th joint propulsion conference and exhibit*, AIAA Paper 1992-3770, July, 1992.

37. Dittmar, J. H., and Hall, D. G., "The Effect of Swirl Recovery Vanes on the Cruise Noise of an Advanced Propeller." *13th Aeroacoustics Conference*, AIAA Paper 1990-3932, October, 1990.

38. Wang, Y., Li, Q., Eitelberg G., Veldhuis, L. L. M., and Kotsonis, M., "Design and Numerical Investigation of Swirl Recovery Vanes for the Fokker 29 Propeller,". *Chinese Journal of Aeronautics*, Vol. 27, No. 5, 2014, pp. 1128–1136.

39. Stokkermans, T. C. A., van Arnhem N., Veldhuis, and L. L. M., "Mitigation of Propeller Kinetic Energy Losses with Boundary Layer Ingestion and Swirl Recovery Vanes," *Proceedings of the 2016 Applied Aerodynamics Conference*, Royal Aeronautical Society, London, U. K., 2016.

40. Li, Q., Wang, Y., and Eitelberg, G., "An Investigation of Tip Vortices Unsteady Interaction for Fokker 29 Propeller with Swirl Recovery Vane,". *Chinese Journal of Aeronautics*, Vol. 29, No. 1, 2016, pp. 117-128.

41. Sinnige, T., Stokkermans, T. C. A., Ragni, D., Eitelberg, G., and Veldhuis, L. L. M., "Aerodynamic and Aeroacoustic Performance of a Propeller Propulsion System with Swirl-Recovery Vanes," *Journal of Propulsion and Power*, Vol. 34, No. 6, 2018, pp. 1376-1390.

42. Witkowski, D. P., Lee, A. K., and Sullivan, J. P., "Aerodynamic Interaction between Propellers and Wings," *Journal of Aircraft*, Vol. 26, No. 9, 1989, pp. 829-836.

43. Snyder Jr., M. H., and Zumwalt, G. W., "Effects of Wingtip-mounted Propellers on Wing Lift and Induced Drag," *Journal of Aircraft*, Vol. 6, No. 5, 1969, pp. 392-397.

44. Patterson Jr., J., and Bartlett, G., "Effect of a Wing-tip Mounted Pusher Turboprop on the Aerodynamic Characteristics of a Semi-span Wing," *21st Joint Propulsion Conference*, AIAA paper 85-1286, July, 1985.

45. Sinnige, T., "Aerodynamic and Aeroacoustic Interaction Effects for Tip-Mounted Propellers: An Experimental Study," Ph.D. Dissertation, Department of Aerospace Engineering, Delft University of Technology, Delft, the Netherlands, 2018.

46. Stokkermans, T. C. A., "Design and Analysis of Swirl Recovery Vanes for an Isolated and a Wing Mounted Tractor Propeller," M.Sc. Thesis, Department of Aerospace Engineering, Delft University of Technology, Delft, the Netherlands, 2015.

47. Rankine, W. J. M., "On the Mechanical Principles of the Action of Propellers," *Transactions of the Institution of Naval Architects*, Vol. 6, 1865, pp. 13-39.

48. Froude, R. E., "On the Part Played in Propulsion by Differences of Fluid Pressure," *Transactions of the Institute of Naval Architects*, Vol. 30, 1889, pp. 390-405.

49. Van Kuik, G. A. M., Sørensen, J. N., and Okulov, V. L., "Rotor Theories by Professor Joukowsky: Momentum Theories," *Progress in Aerospace Sciences*, Vol. 73, 2015, pp.1-18.

50. van Kuik, G., *The Fluid Dynamic Basis for Actuator disk and Rotor Theories*, Amsterdam: IOS Press, 2018.

51. Prandtl, L. "Application of Modern Hydrodynamics to Aeronautics," NACA Technical Report, No. 116, 1923.

52. Betz, A., "Screw Propeller with Minimum Energy Loss," ("Schraubenpropeller mit Geringstem Energieverlust"), 1919, Translation from German by Sinclair, D. A., Translation Section, NRC Library.

53. Saffman, P. G., *Vortex Dynamics*, Cambridge University Press, 1992.

54. Bagai, A., and Leishman, J. G., "Rotor Free-wake Modeling Using a Pseudo-Implicit Technique—Including Comparisons with Experimental Data," *Journal of the American Helicopter Society*, Vol. 40, No. 3, 1995, pp. 29-41.

55. Benini, E., "Significance of Blade Element Theory in Performance Prediction of Marine Propellers," *Ocean Engineering*, Vol. 31, 2004, pp. 957-974.

56. Gur, O., and Rosen, A., "Comparison between Blade-element Models of Propellers," *The Aeronautical Journal*, Vol. 112, No. 1138, 2008, pp.689-704.

57. Bass, R., "Small Scale Wind Tunnel Testing of Model Propellers," *24th Aerospace Sciences Meeting*, AIAA-86-0392, January, 1986.

58. Witkowski, D. P., Lee, A. K., and Sullivan, J. P., "Aerodynamic Interaction between Propellers and Wings," *Journal of Aircraft*, Vol. 26, No. 9, 1989, pp. 829-836.

59. Favier, D., Maresca, C., and Agnes, A., "Unsteady Interactional Effects between a Propeller and a Fixed Wing," *AIAA 9th Applied Aerodynamics Conference*, AIAA Paper 91-3231, September, 1991.

60. Chiaramonte, J. Y., Favier, D., Maresca, C., and Benneceur, S., "Aerodynamic Interaction Study of the Propeller/Wing under Different Flow Configurations," *Journal of Aircraft*, Vol. 33, No. 1, 1996, pp. 46-53.

61. Anderson, J., *Fundamentals of Aerodynamics, Fifth Edition*, New York: McGraw-Hill, 2011.

62. Johnston, R. T., and Sullivan, J. P., "Unsteady Wing Surface Pressures in the Wake of a Propeller," *Journal of Aircraft*, Vol. 30, No. 5, 1993, pp. 644-651.

63. Roosenboom, E. W. M., "Image Based Measurement Techniques for Aircraft Propeller Flow Diagnostics: Propeller Slipstream Investigations at High-lift Conditions and Thrust Reverse," Ph.D. Dissertation, Department of Aerospace Engineering, Delft University of Technology, Delft, the Netherlands, 2011.

64. Katz, J., and Plotkin, A., *Low-speed Aerodynamics, Second Edition*, Cambridge University Press, 2001.

65. Obayashi, S., and Tsukahara, T., "Comparison of Optimization Algorithms for Aerodynamic Shape Design," *AIAA Journal*, Vol. 35, No. 8, 1997, pp. 1413-1415.

66. Coney, W. B., "A Method for the Design of a Class of Optimum Marine Propulsors," Ph.D. Dissertation., Dept. of Ocean Engineering, Massachusetts Institute of Technology, 1989.

67. Hildebrand, F. B., "Topics in Higher-Dimensional Calculus," *Advanced Calculus for Applications*, Englewood Cliffs, NJ: Prentice-Hall, 1962, pp. 357-359.

68. Conway, J. T., "Analytical Solutions for the Actuator Disc with Variable Radial Distribution of Load," *Journal of Fluid Mechanics*, Vol. *297*, 1995, pp. 327-355.

69. Ortun B., Boisard R., and Gonzalez-Martino I., "In-plane Airloads of a Propeller with Inflow Angle: Prediction vs. Experiment", *30th AIAA Applied Aerodynamics Conference*, AIAA Paper 2012-2778, June, 2012.

70. Lignarolo, L. E. M., Ragni, D., Krishnaswami, C., Chen, Q., Ferreira, C. J., and Van Bussel, G. J. W., "Experimental Analysis of the Wake of a Horizontal-Axis Wind-Turbine Model," *Renewable Energy*, Vol. 70, 2014, pp. 31-46.

71. ANSYS, C., "*ANSYS CFX-Solver Theory Guide, Release 14.5*" ANSYS, Inc., 2012.

72. Menter, F. R., "Two-equation Eddy-viscosity Turbulence Models for Engineering Applications," *AIAA Journal*, Vol. 32, No. 8, 1994, pp.1598-1605.

73. Balasubramanian, R., Barrows, S., and Chen, J., "Investigation of Shear-Stress Transport Turbulence Model for Turbomachinery Applications," *46th AIAA Aerospace Sciences Meeting and Exhibit*, AIAA Paper 2008-0566, January, 2008.

74. Roache, P. J., "Perspective: A Method for Uniform Reporting of Grid Refinement Studies," *Journal of Fluids Engineering*, Vol. 116, No. 3, 1994, pp. 405-413.

75. Wrench Jr., J. W., "The Calculation of Propeller Induction Factors," Applied Mathematics Laboratory Technical Report, No. 1116, Feb. 1957.

76. Epps, B., and Kimball, R. W., "Unified Rotor Lifting Line Theory," *Journal of Ship Research*, Vol. 57, No. 4, 2013.

77. Jacobs, E. N., Ward, K. E., and Pinkerton, R. M., "The Characteristics of 78 Related Airfoil Sections from Tests in the Variable-Density Tunnel," NACA TR-460, January 1933.

78. Hooke, R., and Jeeves, T. A., "Direct Search Solution of Numerical and Statistical Problems," *Journal of the ACM* , Vol. 8, No. 2, 1961, pp.212-229.

79. Drela, M., "XFOIL: An Analysis and Design System for Low Reynolds Number Airfoils," *Low Reynolds Number Aerodynamics*, Springer Berlin Heidelberg, 1989, pp. 1-12.

80. Stuermer, A., "Unsteady CFD simulations of Contra-rotating Propeller Propulsion Systems," *44th AIAA/ASME/SAE/ASEE Joint Propulsion Conference & Exhibit*, AIAA Paper 2008-5218, July, 2008.

81. Horváth, C., "Beamforming Investigation of Dominant Counter-rotating Open Rotor Tonal and Broadband Noise Sources," *AIAA Journal*, Vol. 53, No. 6, 2015, pp.1602-1611.

82. Prederi, D., Parrinello, A., Gadda, A., and Mantegazza, P., "Flutter Analysis of Propfan-open Rotors,", *Journal of Aircraft*, Vol. 55, No. 3, 2018, pp. 1024-1040.

83. Gopalarathnam, A., Broughton, B. A., McGranahan, B. D., and Selig, M. S., "Design of Low Reynolds Number Airfoils with Trips", *Journal of Aircraft*, Vol. 40, No. 4, 2003, pp. 768-775.

84. Lyon, C. A., Selig, M. S., and Broeren, A. P., "Boundary Layer Trips on Airfoils at Low Reynolds Numbers," *35th Aerospace Sciences Meeting & Exhibit*, AIAA Paper 1997-0511, January, 1997.

85. Howard, R. M., and Miley, S. J., "Time-Dependent Boundary-Layer Response in a Propeller Slipstream," *Journal of Aircraft*, Vol. 26, No. 9, 1989, pp. 863-869.

86. Renoud, R. W., and Howard, R. M., "Airfoil Boundary-layer Response to an Unsteady Turbulent Flowfield," *AIAA Journal*, Vol. 28, No. 11, 1990, pp. 1894-1900.

87. Nahuis, R., and Sinnige, T., "Design, Manufacture and Commissioning of a New NLR Six-Component Rotating Shaft Balance for Delft University of Technology," *10th International Symposium on Strain-Gauge Balances*, Mianyang; China, 2016.

88. Gracey, W., "Wind-Tunnel Investigation of a Number of Total-Pressure Tubes at High Angles of Attack-Subsonic, Transonic, and Supersonic Speeds," NACA TR-1303, January, 1957.

89. Wieneke, B., "PIV Uncertainty Quantification from Correlation Statistics," *Measurement Science and Technology*, Vol. 26, No. 7, 2015, pp. 074002.

90. Beck, N., Radespiel, R., Lenfers, C., Friedrichs, J., and Rezaeian, A., "Aerodynamic Effects of Propeller Slipstream on a Wing with Circulation Control," *Journal of Aircraft*, Vol. 52, No. 5, 2015, pp.1422-1436.

91. Hanson, D. B., and Magliozzi, B., "Propagation of Propeller Tone Noise Through a Fuselage Boundary Layer," *Journal of Aircraft*, Vol. 22, No. 1, 1985, pp. 63-70.

92. Miranda, L., and Brennan, J., "Aerodynamic Effects of Wingtip-mounted Propellers and Turbines," *4th Applied Aerodynamics Conference*, AIAA Paper 1986-1802, June, 1986.

93. Jensen, L., Hansman, R. J., Venuti, J., and Reynolds, T., "Commercial Airline Altitude Optimization Strategies for Reduced Cruise Fuel Consumption," *14th AIAA Aviation Technology, Integration, and Operations Conference*, AIAA Paper 2014-3006, June, 2014.

94. ATR, "ATR Family," URL: http://www.atraircraft.com/products_app/media/pdf/FAMILY_septembre2014.pdf

95. ATR Marketing Department, "ATR Family,", URL: http://www.atraircraft.com/products_app/media/pdf/FAMILY_septembre2014.pdf.

96. Babikian, R., Lukachko, S. P., and Waitz, I. A., "The Historical Fuel Efficiency Characteristics of Regional Aircraft from Technological, Operational, and Cost Perspectives," *Journal of Air Transport Management*, Vol. 8, No. 6, 2002, pp. 389-400.

97. Van Dam, C. P., and Nikfetrat, K., "Accurate Prediction of Drag Using Euler Methods," *Journal of Aircraft*, Vol. 29, No. 3, 1992, pp. 516–519.

98. Yamazaki, W., Matsushima, K., and Nakahashi, K., "Drag Decomposition-Based Adaptive Mesh Refinement," *Journal of Aircraft*, Vol. 44, No. 6, 2007, pp. 1896–1905.

99. Blackwell, J., "Numerical Method To Calculate the Induced Drag or Optimal Span Loading for Arbitrary Non-Planar Aircraft," NASA SP-405, May, 1976.

100. Lotstedt, P., "Accuracy of a Propeller Model in Inviscid Flow," *Journal of Aircraft*, Vol. 32, No. 6, 1995, pp. 1312-1321.

101. Jones, D. R., Perttunen, C. D., and Stuckman, B. E., "Lipschitzian Optimization without the Lipschitz Constant," *Journal of Optimization Theory and Applications*, Vol. 79, No. 1, 1993, pp. 157-181.

102. Hansen, P., Jaumard, B., and Lu, S. H., "Global Optimization of Univariate Lipschitz Functions: I. Survey and Properties," *Mathematical Programming*, Vol. 55, 1992, pp. 251-272.

103. Bartholomew-Biggs, M. C., Parkhurst, S. C. and Wilson, S. P., "Using DIRECT to Solve an Aircraft Routing Problem," *Computational Optimization and Applications*, Vol. 21, No. 3, 2002, pp. 311-323.

104. Watson, L. T., and Baker, C. A., "A Fully-Distributed Parallel Global Search Algorithm," *Engineering Computations*, Vol. 18, No. 1/2, 2001, pp. 155-169.

105. Cox, S. E., Haftka, R. T., Baker, C. A., Grossman, B., Mason, W. H., and Watson, L. T., "A Comparison of Global Optimization Methods for the Design of a High-Speed Civil Transport," *Journal of Global Optimization*, Vol. 21, No. 4, 2001, pp. 415-432.

106. Yang, X. S., and Koziel, S. eds., "Computational Optimization and Applications in Engineering and Industry," *Studies in Computational Intelligence*, Vol. 359, Springer Science & Business Media, 2011.

107. Tominaga, Y., "Flow around a High-rise Building Using Steady and Unsteady RANS CFD: Effect of Large-scale Fluctuations on the Velocity Statistics," *Journal of Wind Engineering and Industrial Aerodynamics*, Vol. 142, 2015, pp. 93-103.

108. Lenfers, C., Beck, N., and Bauer, M., "Propeller and Active High Lift Wing Interaction in Experiment and Simulation," *New Results in Numerical and Experimental Fluid Mechanics X*, pp. 51-61, Springer, Cham. 2016.

109. Williams, M. H., and Cho, J., "Propeller-wing Interaction Using a Frequency Domain Panel Method," *Journal of Aircraft*, Vol. 27, No. 3, 1990, pp. 196-203.

110. Montgomerie, B., "De-camber: Explanation of an Effect of Lift Reduction Near the Tip Caused by the Local Flow around Airplane Wings or Wind Turbine Tips," *Plenary Meeting of the Group for Dynamic Stall and 3D Effects a European Union, Joule 2 Project*, Cranfield Institute of Technology, April 3-4, 1995.

111. Schlichting, H., and Gersten, K., *Boundary Layer Theory*, Springer, 8th Edition, 2000.

112. Sinnige, T., Ragni, D., Eitelberg, G., and Veldhuis, L. L., "Mitigation of Pusher-propeller Installation Effects by Pylon Trailing-edge Blowing," *Journal of Aircraft*, Vol. 54, No. 1, 2016, pp. 292-300.

113. Bridgman, P. W., *Dimensional Analysis*, Yale University Press, 1922.

114. Barenblatt, G. I., *Scaling*, Cambridge University Press, 2003.

115. Torenbeek, E., "Synthesis of Subsonic Airplane Design: an Introduction to the Preliminary Design of Subsonic General Aviation and Transport Aircraft, with Emphasis on Layout, Aerodynamic Design, Propulsion and Performance," Springer Science & Business Media, 2013.

116. Filippone, A., *Advanced Aircraft Flight Performance*, Cambridge University Press, 2012.

Acknowledgements

The time I spent in the Netherlands during my PhD research is the most challenging period of time I have so far in terms of getting exposed to a new language, a new living environment, and a totally different culture. Luckily, with the tremendous help and strong support from my colleagues, my friends, and my families, I made it through. Hereby, I would like to acknowledge all of them.

First and foremost, I would like to express my great gratitude to my promotors Professor Leo Veldhuis and Professor Georg Eitelberg for both giving me the opportunity of doing research in TU Delft and guiding me through it all along the four years. Your deep understandings of aerodynamics and wide horizon of aeronautical knowledge are setting up good examples to me all the time and motivates me to be as excellent and knowledgeable as both of you.

I am grateful to my master supervisor Professor Yangang Wang, who not only provided valuable supervision for my master thesis, but also gave me strong support during my PhD. Special thanks to Tomas Sinnige. You are always the first person I turn to for questions and discussions. I have learned a lot from you, especially your prudent scientific attitude and good working habits. Many thanks to Daniele Ragni for the help and instruction of PIV measurements. Thanks to Francesco Avallone for co-supervising master student and help with LBM-related work. Thanks to all the PhD colleagues of the propeller group, Yannian Yang, Tom Stokkermans, Nando van Arnhem, Peijian Lv, Reynard de Vries and Sumit Tambe. I can always expect nice discussions from the group meeting every Friday. I am also grateful to the administrative assistance from Nana Saaneh and Kimberley Graauw. Thanks to Kenan Öztürk, Xinyuan Liu, and Luc van den Ende for doing master projects with me. All your work contributes to my research to a great extent.

The experimental work in OJF would not succeed without the help from Henk-Jan Siemer, Nico of Beek, Frits Donker Duyvis, Peter Duyndam, Stefan Bernardy, Leo Molenwijk and Dennis Bruikman. Thanks for all your valuable work and support.

Thanks also go to my Chinese friends, Shuanghou, Xiaojia, Qingqing, Zi, Ye, Juan, Kaikai, Yili, Feijia, Zaoxu, Xiaojun, Xiaodong, Pengling, Haohua, Xiangrong and many more. It always makes me feel like home when spending time together with you. My gratitude to all the members of the badminton clubs Sweti Day and USSR. Thanks to Jiawei, Yingyi, Xiaoman, Jun, Kailun, Zhi, Chichi, Bjorn, Xia, Nicky, Queenie, Indra, Yanbo, Anita, CK, JP, Yan, Jie and many others for all the happy moments of playing badminton and having parties together.

Great thanks to my parents, for your endless love and support whenever I need them. I always hope that I can make you proud of me someday. I have tried every effort to achieve that during the last four years by making myself a better man every day in every aspect. Love you with all my heart.

Publications

Journal articles

- Li, Q., Öztürk, K., Sinnige, T., Ragni, D., Wang, Y., Eitelberg, G., and Veldhuis, L. L. M., "Design and Experimental Validation of Swirl-recovery Vanes for Propeller Propulsion Systems," *AIAA Journal*, Vol. 56, No. 12, 2018, pp. 4719-4729.

- Li, Q., Liu, X., Eitelberg, G., and Veldhuis, L. L. M., "Numerical Investigation of Configuration with Optimum Swirl Recovery for Propeller Propulsion Systems," *AIAA Journal*, Vol. 57, No. 4, 2019, pp. 1502-1513.

Conference papers

- Van den Ende, L., Li, Q., Avallone, F., Casalino, D., Eitelberg, G., and Veldhuis, L. L. M., "Aerodynamic and Aeroacoustic investigation of Swirl Recovery Vanes for Propeller Propulsion Systems," *31st Congress of the International Council of the Aeronautical Sciences*, Belo Horizonte, Brazil, September, 2018.

- Li, Q., Liu, X., Eitelberg, G., and Veldhuis, L. L. M., "Numerical Investigation of Swirl Recovery Design for Propeller Propulsion Systems," *2018 Applied Aerodynamics Conference*, AIAA Paper 2018-3648, June, 2018.

- Li, Q., Öztürk, K., Sinnige, T., Ragni, D., Wang, Y., Eitelberg, G., and Veldhuis, L. L. M., Towards Optimum Swirl Recovery Vanes for Propeller Propulsion Systems," *35th AIAA Applied Aerodynamics Conference*, AIAA Paper 2017-3571, June, 2017.

Curriculum Vitae

1990.02.07 Born in Taiyuan, Shanxi, China

Education

2014.11–present Ph.D. researcher in Flight Performance and Propulsion, Faculty of Aerospace Engineering, Delft University of Technology under supervision of Professor Leo Veldhuis and Professor Georg Eitelberg.

2012.09–2015.03 Master of Science in Propulsion Theory and Engineering of Aeronautics and Astronautics, School of Power and Engine, Northwestern Polytechnical University under supervision of Professor Yangang Wang.

Thesis: Preliminary Design and Optimization of Swirl Recovery Vane for Fokker F29 Propeller.

2008.09–2012.06 Bachelor of Science in Flight Vehicle Propulsion Engineering, School of Power and Engine, Northwestern Polytechnical University.